M.Sc. Thesis, The Initial State of Heavy Ion Collisions in the IP-Glasma Framework

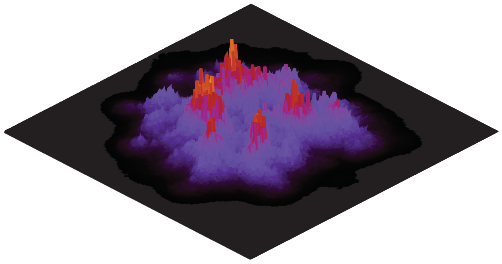

Scott McDonald
Supervisor: Sangyong Jeon
Department of Physics
McGill University
Montréal, Québec
Canada

A Thesis submitted to the
Faculty of Graduate Studies and Research
in partial fulfillment of the requirements for the degree of
Masters of Science

Dedicated to Catherine

Contents

List of Figures

List of Tables

Abstract

First implemented by Schenke et al [1, 2], IP-Glasma is a QCD based initial state model for Heavy Ion Collisions that is able to reproduce a wide range of observables, both on average and in event-by-event distributions, when used to initialize hydrodynamic simulations. The model incorporates small-x gluon saturation via the Impact Parameter Dependent Saturation Model (IPSAT) [3] and introduces sub-nucleonic color charge fluctuations by stochastically sampling the color charge density for each nucleon, before ultimately evolving the gluon field configuration via a classical Yang-Mills evolution. This thesis is the debut of a second formulation of IP-Glasma, the results of which will be presented throughout this work. The objective is to reproduce the results of the highly successful IP-Glasma model and to extend them to study new experimental data in order to further constrain the transport properties of the Quark Gluon Plasma. Predictions and postdictions for Run 2 at the LHC, which is currently underway, will be presented and discussed.

Résumé

Implémenté pour la première fois par Schenke et al [1, 2], IP-Glasma est un modèle de conditions initiales pour collisions d'ions lourds, basé sur la chromodynamique quantique, capable de décrire un large éventail d'observations lorsqu'utilisé en combinaison avec une simulation hydrodynamique. Le modèle inclus la saturation des gluons de très basses énergies à l'aide du Modèle de Saturation avec Dépendance au Paramètre d'Impact ("Impact Parameter Dependent Saturation Model" IPSAT) [3], et introduit des fluctuations de charges sub-nucléoniques en échantillonnant stochastiquement la densité de charges de couleur de chaque nucléon, pour ensuite évoluer les configurations du champ de gluon à l'aide d'une évolution Yang-Mills classique. Cette thèse est la première étape d'une nouvelle formulation du modèle IP-Glasma. L'objectif est de reproduire les résultats existants du modèle et de l'appliquer à de nouvelles données expérimentales, dans le but de mieux déterminer les propriétés de transport du plasma quark-gluon. Des prédictions et postdictions pour le LHC sont présentées et discutées.

Acknowledgments

There are countless people who taught me things that contributed to this thesis. First and foremost, I would like to thank my supervisor, Sangyong Jeon, for his tireless commitment to the success of his students. His guidance and approach to problem solving have taught me a great deal about how to think like a physicist. Most importantly, he put me in a position to succeed and provided the necessary guidance to ensure that I did, for which I am deeply grateful.

I would also like to thank Charles Gale, who was like a second adviser, for his insights and guidance. In addition, I would like to thank the post-docs that have helped me during my time at McGill: Thomas Epelbaum, Gabriel Denicol, and Chun Shen. Each was invaluable to my education and maturation as a physicist. Chun, in particular, helped me diagnose and overcome numerical problems both with MUSIC and IP-Glasma throughout my tenure at McGill, and his physical intuition was often a guiding force.

This work would not be possible without Francois Fillion-Gourdeau's efforts in writing the IP-Glasma code on which this thesis is based. I thank him for this contribution and for his friendly and helpful correspondences. Björn Schenke was gracious enough to share his expertise and his personal notes on IP-Glasma. His suggestions were indispensable, and I am very grateful for his help. I would also like to express my gratitude to all of my fellow graduate students in the nuclear theory group at McGill University. They have taught me a great deal and pushed me to be a better student and physicist.

Finally, I would like to thank my family for their support and encouragement, and for inspiring and nurturing my intellectual curiosity.

The Initial State of Heavy Ion Collisions in the IP-Glasma Framework

1

Introduction

1.1 History

In 1911, Ernest Rutherford discovered the nucleus with his famous gold foil experiment. By scattering alpha particles off of a thin sheet of gold foil, Rutherford was able to determine that atoms were composed of a dense positive core and mostly empty space. Thus nuclear physics was born.

Since Rutherford's time, extraordinary progress has been made in understanding the mysteries and complexities of the nuclear world, yet the idea underlying his experimental approach remains relevant to this day; nuclear physicists are still studying scattering experiments at higher and higher energy resolution to determine the composition and nature of what are believed to be fundamental particles. The question of atomic structure has long been resolved, but the nature of the subnucleonic structure of protons and neutrons, collectively known as nucleons, is still the subject of intense study. Today, nuclear physicists collide heavy ions such as gold and lead nuclei at relativistic speeds to learn about the prevailing nuclear theory of the day, Quantum Chromodynamics (QCD).

1.2 Quantum Chromodynamics

QCD is the theory that describes the strong nuclear force that binds quarks into nucleons. Just as the electromagnetic force binds positively charged nuclei with negatively charged electrons to form atoms, the strong nuclear force binds particles that carry "color" charge together to form hadrons. Hadrons are made up of either three

quarks (baryons), as in the case of protons and neutrons, or a quark and an anti-quark (mesons), such as pions and kaons. There are three generations of quarks, each of which has two members, for a total of six (up, down, charm, strange, top, bottom). Given the six quarks and the rules for combining them into hadrons stated above, one can create a zoo of hadronic matter.

In the Standard Model of particle physics forces are "mediated" or "carried" by particles known as gauge bosons. In the case of Quantum Electrodynamics(QED), the relativistic quantization of Maxwell's equations of electromagnetism (EM), the mediating particle is the photon. For QCD on the other hand, there are eight such particles, known as gluons, each carrying different color content, that mediate the QCD interaction. In both cases, the gauge bosons mediate forces between particles that carry electromagnetic force or color force for QED and QCD, respectively. Some particles, such as quarks, carry both types of charge, EM and color, and thus can interact via either force. However, the range of the two forces are sufficiently different that they are relevant on different length scales.

Despite the similarities, QCD poses clear challenges that make it more difficult to study than QED, given the same set of tools. Firstly QCD is an *asymptotically free* theory, meaning that the interaction is weak at short distances (high energy), but becomes strong at large distances (low energy). This can be contrasted with the more familiar forces of gravity and electromagnetism that behave in the opposite manner, growing weaker at longer distances. Rather, it is more suitable to think of the strong force as an elastic band that applies a constant restoring force as it is stretched, until eventually it snaps, creating a particle and an anti-particle pair.

In fact, this analogy describes a consequence of asymptotic freedom known as *color confinement*. In order to separate two particles that carry color charge, say a quark and an anti-quark for example, one would need greater and greater energy input until, eventually, it would become energetically favorable to produce a quark and an anti-quark out of the vacuum. At this point, the tube of energy connecting the quark and anti-quark, known as a "flux tube," will snap, leaving two colorless

bound states. Thus, color charge is said to be *confined* within colorless bound states made up of either three quarks (baryons) or a quark and an anti-quark (mesons). Consequently, we cannot study free color charged particles under normal conditions which leads to the importance of heavy ion collisions in understanding QCD, to be addressed in more detail in the following discussion.

On the theoretical side, a second, more technical difficulty owing to the coupling constant occurs in the strongly coupled (low energy) regime. At low energies, perturbative techniques, such as those employed with extraordinary success to study QED, are not feasible. One saving grace is that the QCD coupling is energy dependent and becomes weaker at high energies. This means that if we are able to build experiments that can probe energies where QCD is weakly coupled, we may be able to compare experimental results with theory derived using well-established perturbative techniques. Yet another reason to have hope is the fact that it is believed that at sufficiently high temperatures and pressures, strong matter reaches deconfinement, where the bound states melt into a soup of color charge made up of deconfined quarks and gluons and known as Quark Gluon Plasma (QGP).

1.3 Heavy Ion Collisions and QGP

In the face of the challenges mentioned, and with these opportunities in mind, physicists have devised various ways of studying QCD matter including lattice QCD, AdS/CFT, non-perturbative techniques, and, most relevant to this thesis, Heavy Ion Collisions (HIC's). Current HIC experiments are sufficiently energetic to both reach the weakly coupled regime, where QCD is better understood, and to form QGP, thus opening a window into the behavior of unbound quarks and gluons at extreme temperatures and pressures. This novel form of matter is believed to have existed in the early universe, shortly after the Big Bang.

While the study of QGP may provide insight into other areas of physics, it is a rich and fascinating form of matter worthy of study in its own right. Its formation at the Relativistic Heavy Ion Collider (RHIC) at Brookhaven National Lab (BNL) in

Long Island, New York and the Large Hadron Collider (LHC) at CERN in Geneva, Switzerland has been the source of great excitement and the subject of intense investigation. By studying QGP, physicists hope to gain insight into the phase diagram, transport coefficients, equation of state, and perhaps many more interesting features of hot QCD matter. The obvious question is, how do we know that we have created QGP? What is the evidence?

1.3.1 Signatures of the Formation of QGP

Collective Flow

One of the key signatures of QGP is the presence of elliptic flow, as quantified by the second Fourier coefficient of the expansion of the azimuthal distribution of particles,

$$\frac{dN}{d\phi} = \frac{N}{2\pi}\left(1 + \sum_n 2v_n \cos\left[n(\phi - \psi_n)\right]\right) \tag{1.1}$$

where ψ_n is the phase of v_n and is known as the event-plane angle. This is the angle from which the v_n expansion is measured and orients the event along the impact parameter axis.

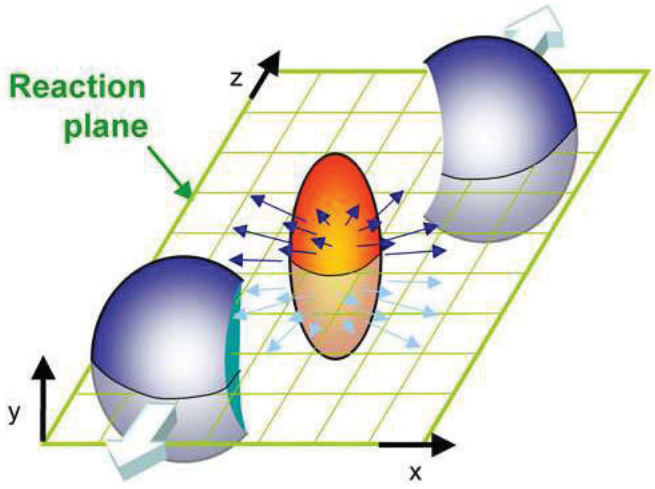

Figure 1.1: Colliding nuclei with almond shape overlap leading to a difference in pressure gradients in the long and short axis. This in turn leads to the elliptic flow phenomenon. Figure taken from [4].

For collisions with a finite impact parameter, there will be an almond-like overlap region between the colliding nuclei, as can be seen from figure (1.1). This almond

like shape causes an anisotropy in pressure gradients in which the fluid expands more rapidly parallel to the x-axis in figure (1.1), compared to the y-direction where the pressure gradient is smaller. The shape of this momentum anisotropy causes the Fourier expansion to be dominated by the $\cos(2\phi)$ term, v_2, known as elliptic flow.

The initial state energy anisotropies are quantified by ϵ_n,

$$\epsilon_n = \frac{\sqrt{\langle r^n \cos(n\phi)\rangle^2 + \langle r^n \sin(n\phi)\rangle^2}}{\langle r^n \rangle} \tag{1.2}$$

where average quantities are the energy density weighted averages over the transverse plane.

$$\langle * \rangle = \frac{\int d^2x * \epsilon(x)}{\int d^2x \epsilon(x)} \tag{1.3}$$

and ϵ is the local energy density. The fact that the initial distribution of energy gets converted to a momentum anisotropy is strong evidence for collective behavior and a signature of the formation of QGP. This thesis will focus heavily on flow observables that are directly related to the v_n and ϵ_n, as well as the interplay between these quantities.

1.3.2 HIC Theory Overview

From a theoretical standpoint, heavy ion collisions can be broken into three distinct stages, each governed by their own effective theories: 1) Pre-equilibrium dynamics and thermalization, 2) Hydrodynamic evolution, and 3) Hadronization. In fact, one can subdivide HIC's much more finely, as can be seen in table (1.3.2), but the main divisions are those mentioned above. This thesis will be primarily concerned with the pre-equilibrium dynamics of heavy ion collisions but will also rely on the other phases of the evolution to be able to compare observables with experimental data, since the initial state is not directly observed in experiment. Hydrodynamics and hadronization will allow for a phenomenological study in which the results of the IP-Glasma model, to be outlined in this thesis, are compared with experimental data. That being said, this thesis will give only the most cursory overview of the hydrodynamics and hadronization models employed, as they are not the focus of the

current work. The specific numerical implementations used for these two theories are MUSIC for hydrodynamics, and UrQMD for hadronization. MUSIC, or MUScl for Ion Collisions, is a second-order relativistic viscous hydrodynamics simulation, including shear and bulk viscosities, developed at McGill University [5]. UrQMD stands for Ultrarelativistic Quantum Molecular Dynamics, and was first developed in at Göethe Universität in Frankfurt, Germany [6].

To illustrate the complexity of HIC's, table (1.3.2) gives a brief description of HIC's and the prevailing theories that govern each stage of the collision. The far right column gives the specific numerical simulations used for this thesis.

Table 1.1: Table showing the complexity of heavy ion collisions along with the variety of models and numerical simulations used to study them in this thesis.

Description	Time	Prevailing Theory	Simulation Used
Before the collision	$t < t_0$	Color Glass Condensate	IP-Glasma
Immediately after the collision	$t_0 < t < \frac{1}{Q_s}$	Strong Classical Fields - Glasma	IP-Glasma
Thermalization/Isotropization	$\frac{1}{Q_s} < t < t_{equilibrium}$	Glasma/Kinetic Theory/Hydro	IP-Glasma
QGP (Hydrodynamics)	$t_{equilibrium} < t < t_{freezeout}$	Relativistic Viscous Hydrodynamics	MUSIC
Hadron Gas	$t_{freezeout} < t < t_{freestream}$	Cooper-Frye/UrQMD/Kinetic Theory	UrQMD
Free Streaming	$t_{freestream} < t$	Particles free stream to detectors	UrQMD

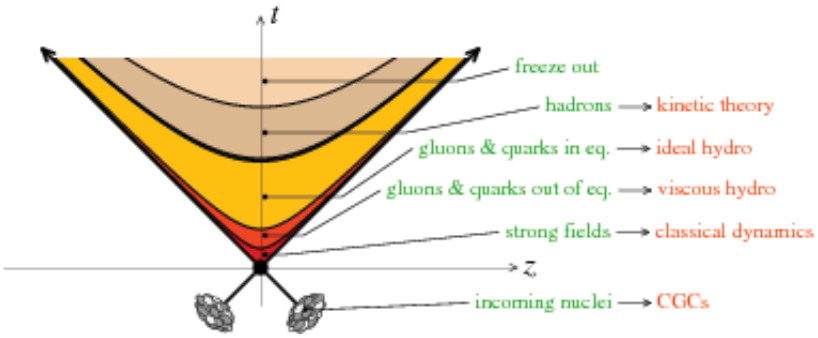

Figure 1.2: Schematic diagram showing the various stages of a heavy ion collision and the effective field theories by which they are governed. This thesis is focused very specifically on the the pre-collision and classical Yang Mills dynamics represented as the two incoming nuclei, and the red strip in the light cone, respectively. This figure was taken from [7]

.

In many ways the pre-equilibrium physics is the least well constrained component out of the three, but is currently under intense study. It is important to note that

knowledge of the initial nuclear wave functions will likely set the ultimate constraint on our understanding of HIC's, and thus the initial state will be critical in the study of HIC's for years to come. Relativistic viscous hydrodynamics has been enormously successful in describing the behavior of the QGP formed at RHIC and the LHC, but it is not yet fully understood how the system gets to an equilibrated state for which hydrodynamics is justified, or whether such a stringent condition can be relaxed for hydrodynamics. While this thesis will not address this crucial question directly, it does aim to demonstrate the effectiveness of IP-Glasma, a QCD based model that is able to reproduce experimental data for many observables of interest when used as an initial condition for hydrodynamic simulations.

Historically, hydrodynamics has been initialized with a number of geometric initial conditions such as Monte-Carlo Glauber, or wounded nucleon models. IP-Glasma, however, is a QCD based model that includes saturation physics as well as both geometric fluctuations and sub-nucleonic fluctuations relating to the distribution of color charge density within each nucleon. Its ability to reproduce a wide range of observables including quantities that are entirely fluctuation based such as v_3, as well as event-by-event v_n and multiplicity distributions have made IP-Glasma the standard in the field.

In terms of procedure, IP-Glasma is a Monte-Carlo event generator that determines the saturation scale within the IPSat framework [3] and relates it to the color charge density. The saturation scale is the energy scale at which the gluon density ceases to grow, or saturates, within a high energy nucleus or hadron and will be discussed in far greater detail in the next chapter. Once the color charge density is obtained, IP-Glasma determines the gauge fields in the McLerran-Venugopalan (MV) [15] model and evolves them in time via the classical Yang Mills equations. Finally, IP-Glasma computes the stress-energy tensor, and diagonalizes it to find the energy density and local velocity that are relevant to initializing hydrodynamical simulations. The details of this process will be outlined in this thesis.

1.3.3 Goals of this Thesis

As experimentalists smash heavy ions together near the speed of light, theorists try to create a framework in which to understand their results. Progress in the field of heavy ion collisions is a constant back and forth in which theorists and experimentalists trade turns making advances that in turn pave the way for their counterparts to advance the field. This thesis is an effort to summarize one of the most successful theoretical models for the initial state of HIC's, namely IP-Glasma, and perhaps make a small contribution to its advancement.

This thesis was first and foremost aimed at reproducing the hugely successful results of the IP-Glasma model [1, 2] as a foundation for future novel and exciting applications. Run 2 at the LHC, however, has provided an immediate opportunity to expand this work to make predictions and postdictions relating to hadronic observables at 5.02 TeV. Novel results are presented for hadron integrated v_n coefficients, charged hadron multiplicity, and hadron differential v_n. In addition, predictions are made for $\langle p_T \rangle$, v_n distributions, and identified particle as well as multi-strange particle spectra and multiplicities. Also, for the first time, two and three-plane event correlations are computed using IP-Glasma initial conditions. Novel results are also presented for identified particle differential v_3 and v_4 at both 2.76 TeV and 5.02 TeV.

1.3.4 Organization

This thesis is organized as follows. In chapter 2, we will delve into the background theory, beginning with the most general theory, QCD, and we will progressively narrow the focus past the Color Glass Condensate(CGC)[8] and Mclerran-Venugopalan (MV) [15] models, eventually arriving at IPSat and IP-Glasma. We will derive the classical Yang Mills equations in $\tau - \eta$ coordinates and relate the pre-collision gauge fields to the post-collision gauge fields by matching solutions on the boundary of the light-cone. Then, we will back track slightly to determine the form of the pre-collision gauge fields in terms of the color charge density. At this point, we will discuss the saturation scale and relate it to the color charge density. Finally, we will discuss the

boost invariant Hamiltonian formulation of the CGC, the equations of motion, and their implementation of the lattice.

In chapter 3, we derive the stress energy tensor from the CGC action using Noether's theorem and explicitly show the form of its diagonal elements. We discuss the anisotropy of the IP-Glasma stress-energy tensor and the procedure by which we match it to hydrodynamics, We give a brief overview of hydrodynamics and the parameters used for the phenomenological study carried out in this thesis. Finally, we discuss UrQMD, the hadronic cascade model used for the results presented.

In chapter four, numerical details will be discussed. First we will discuss the units and spacing used on the lattice for this work. From there we will discuss lattice gauge theory, the numerical procedure for solving for the initial gauge fields after the collision, the Leap Frog algorithm used to evolve the EOM's, and Brent's Method as used to solve for the saturation scale. Finally, we will show the explicitly form of the stress energy tensor on the lattice.

In the last chapter, we will discuss observables as well as show and analyze the results of this thesis.

2

Theory

2.1 Introduction

In this section, we aim to discuss the theoretical foundation that undergirds the initial state of Heavy Ion Collisions and motivates the rest of this thesis. In particular, this section will discuss the Color Glass Condensate, the Classical Yang Mills equations, IP-Sat, and ultimately IP-Glasma. We will discuss the procedure for determining the color charge configuration of the incoming nuclei, derive the pre-collision gauge fields, relate them to the gauge fields after the collision, and determine the evolution equations.

2.2 Color Glass Condensate (CGC)

The theoretical framework that governs the pre-collision dynamics of heavy ion collisions is an effective field theory known as the Color Glass Condensate (CGC). This evocative name is a good place to start our discussion, at least at the qualitative level. Color, of course, refers to the colors charges of QCD, since each nucleon in the colliding nucleus is made of quarks and gluons, which carry color charge. More specifically, nucleons are made of three valence quarks, but in addition carry many more sea quarks and gluons, all of which carry color charge.

In physics, the term "glass" is often used to describe systems that evolve on time scales much longer than their characteristic microscopic time scale, the reason being that ordinary glass, the material that makes up household items such as window panes and drinking cups, behaves as a solid on short time scales and as a fluid on

long time scales. Here this term is applicable because the boosted partons that act as sources for the gluon fields, experience time dilation and hence are essentially "frozen" over the time scale of the interaction between the two colliding nuclei. Finally, the system is like a condensate because the phase space density of gluons is very high and they behave coherently over length scales $<1/Q_s$, where Q_s is the saturation scale, a quantity that will be discussed in detail in a section later on.

In order to consider the CGC on a more quantitative level, we will first look at the full QCD action

$$S_{QCD} = \int d^4x \left(-\frac{1}{4} F^a_{\mu\nu} F^{\mu\nu a} + \sum_f \bar{\psi}_f \left(i \not{D} - m_f \right) \psi_f \right) \tag{2.1}$$

where f is an index that runs over the number of quark flavors, and a is a color index that runs from 1 to 8, and we have used Feynman's slash notation $\not{D} = \gamma^\mu \partial_\mu$ where γ^μ are Dirac matrices (see appendix (7.3)). This action describes the interaction of dirac fermions, namely quarks that carry color charge along with eight color charged gauge fields, i.e. gluons, and is the fundamental field theory governing quarks and gluons. Here the field strength tensor $F_{\mu\nu}$ and the covariant derivative are defined, respectively as,

$$F^a_{\mu\nu} = \partial_\mu A^a_\nu - \partial_\nu A^a_\mu + g f^{abc} A^b_\mu A^c_\nu \tag{2.2}$$

and,

$$D_\mu = \partial_\mu - i g A^a_\mu t^a \tag{2.3}$$

Comparing the full QCD action to the action of the CGC,

$$S_{CGC} = \int d^4x \left(-\frac{1}{4} F^a_{\mu\nu} F^{\mu\nu a} + J^{\mu a} A^a_\mu \right) \tag{2.4}$$

we can notice some clear differences. First, it is important to remember that the CGC is an *effective field theory* meaning that it describes the system in terms of the effective degrees of freedom, in this case gluon gauge fields. Most strikingly, we see

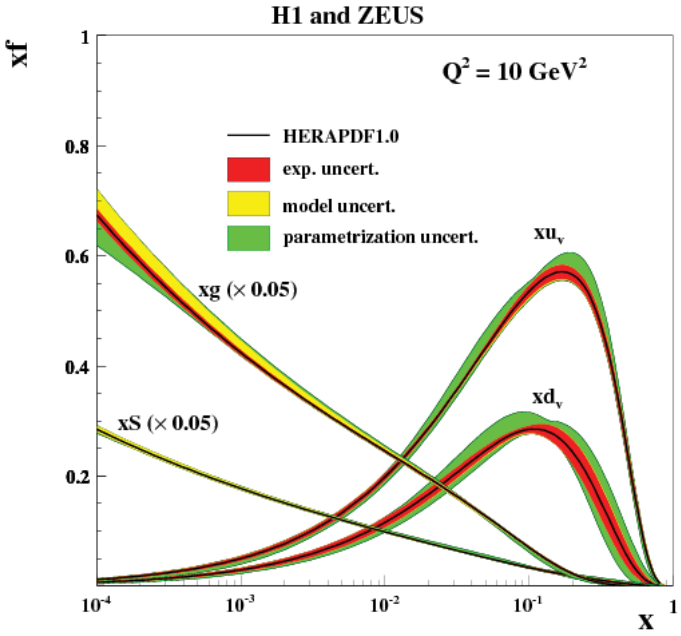

Figure 2.1: HERA data for parton distribution functions taken from [10]. The different curves correspond to different parton distribution functions where xu_v is for the up quark, xd_v is for the down quark, xS is for the strange quark, and xg is for gluons.

that S_{CGC} does not have any fermions. This is because the CGC separates large x (fast) and small x (slow) degrees of freedom, treating the fast partons, including the valence quarks, as "external" sources $J^{\mu a}$ for the slow partons, i.e. classical gauge fields. Here x denotes the fraction of the total nuclear momentum that each parton is carrying, $x = \frac{k}{P}$, where k is the momentum of the parton and P is the momentum of the entire nucleus. Thus the quarks serve as static sources, frozen on the time scale of the interaction, that radiate gluons via bremstrahlung. At sufficiently high energies, the system will be dominated by gluons, which is reflected in the effective action in equation (2.4). This can be seen in the parton distribution functions fitted to HERA data in figure (2.1)

At high energy, or equivalently low values of x, the gluon distribution function clearly dominates the system (note that it has been divided by 20 to compare with the up and down quarks). For the constant x implementation of the saturation scale given in this thesis $x \approx 10^{-4}$ at LHC energies as given by the CMS fit [11], which is

well within the gluon dominated regime.

Furthermore, the sources are considered to be infinitely Lorentz contracted and are thus treated as surface charge densities moving along the light cone (see appendix (7.1) for details on light cone coordinates). In the CGC framework, the nuclei are considered to be in what is often called the "infinite momentum limit", meaning that they are moving with the speed of light. In this case the nuclei truly are two dimensional. This approximation is not a bad one, as the Lorentz factor at the LHC is, for center of mass energy 2.76 TeV,

$$\gamma = \frac{E}{m} = \frac{\sqrt{s}/2}{m} \approx \frac{1.38 \text{ TeV}}{1 \text{ GeV}} = 1380 \tag{2.5}$$

where the masses of the proton and neutron are both approximately 1 GeV. For a nucleus of radius $R_{nuc} \approx 6.0$ fm, this gives a longitudinal width of

$$width = \frac{2R_{nuc}}{\gamma} = \frac{12 \text{ fm}}{1380} \approx 0.0086 fm \tag{2.6}$$

Considering the fact that the radius of a nucleon is about 1 fm, the Lorentz contracted nuclei see one another with less than 1 percent of the longitudinal extent (diameter) of a nucleon at rest.

This applies to the large x valence partons that carry large fractions of the momentum of the incoming nuclei [12]. The small x partons, however, for which $x \ll A^{-1/3}$ are delocalized over distances larger than the diameter of the nucleus, due to the uncertainty principle. Thus the small x gluon fields "see" the large x source terms as infinitely thin in the longitudinal direction.

Additionally, one can use the uncertainty principle on the light cone,

$$\Delta x^+ \sim \frac{1}{k^-} \tag{2.7}$$

where $x^\pm = x_\mp = (x^0 \pm x^3)/\sqrt{2} = (t \pm z)/\sqrt{2}$ is the light-cone coordinate of a parton (appendix (7.1)) and $k^\mp$ is its conjugate momentum in the same coordinate system, to estimate the lifetime of a parton. The relativistic dispersion relation in these coordinates is

$$m^2 = E^2 - \boldsymbol{k}^2 = E^2 - \boldsymbol{k}_\perp{}^2 - k_z^2 = (E + k_z)(E - k_z) - \boldsymbol{k}_\perp{}^2 = 2k^+k^- - \boldsymbol{k}_\perp{}^2 \quad (2.8)$$

Thus the dispersion relation in light-cone coordinates is

$$k^- = \frac{m^2 + \boldsymbol{k}_\perp{}^2}{2k^+} = \frac{m_\perp^2}{2k^+} = \frac{m_\perp^2}{2xP^+} \quad (2.9)$$

where the transverse mass is defined as $m_\perp = m^2 + \boldsymbol{k}_\perp{}^2$. Here P is the total momentum of the nucleus and k is the fraction carried by the parton under consideration. Combining the dispersion relation and the uncertainty principle gives

$$\Delta x^+ \sim x\frac{P^+}{m_\perp^2} \quad (2.10)$$

where x^+ plays the role of the time coordinate, and Δx^+ represents the lifetime of the parton. Thus, the lifetime of each parton is proportional to its momentum fraction x, meaning that large x partons live far longer than small x partons. This means that the small x gluon fields "see" frozen sources. The fact that the large x partons are frozen and two dimensional justifies the color currents being delta functions moving along the light cone,

$$J^{\mu a}(x) = \rho^a_{(A)}(\mathbf{x}_\perp)\delta^{\mu+}\delta(x^-) + \rho^a_{(B)}(\mathbf{x}_\perp)\delta^{\mu-}\delta(x^+) \quad (2.11)$$

where the subscripts A and B refer to the two incoming nuclei. The exact form of the charge density distribution within the colliding nuclei cannot be determined on an event-by-event basis, leaving stochastic sampling as the best alternative. The form of the color charge distribution is model dependent, but, in general, observables can be calculated by [13]

$$\langle O \rangle = \int [D\rho] W[\rho] O[\rho] \quad (2.12)$$

averaging over all charge configurations for an observable O according to the distribution, or weight function, $W[\rho]$. In the McLerran-Venugopalan (MV) [15] model, in which we will be working, the weight function takes the form of a Gaussian as will be seen in the next section.

2.2.1 Eikonal Approximation and Scale Separation

The CGC makes the eikonal approximation in which the hard partons remain undeflected after the collision and proceed along the light cone. To justify this approximation, first made [14], we move to light cone coordinates.

In light coordinates rapidity [1] becomes,

$$y = \frac{1}{2}\ln\left(\frac{E+p_z}{E-p_z}\right) = \frac{1}{2}\ln\left(\frac{p^+}{p^-}\right) \tag{2.13}$$

where $p^\pm = p_\mp = (p^0 \pm p^z)/\sqrt{2}$. Noting that

$$p^+p^- = \frac{1}{2}\left(E^2 - p_z^2\right) = \frac{1}{2}\left(\boldsymbol{p}_\perp{}^2 + m^2\right) = \frac{1}{2}m_\perp^2 \tag{2.14}$$

where the last equality is simply through the definition of transverse mass, allows us to re-write eq. (2.13) as

$$y = \frac{1}{2}\ln\left(\frac{p^+p^+}{p^-p^+}\right) = \frac{1}{2}\ln\left(\frac{2(p^+)^2}{m_\perp^2}\right) \tag{2.15}$$

For a particle created in the collision, say a pion, we define the Feynman x as the longitudinal momentum fraction,

$$x = \frac{p_\pi^+}{p_{proj}^+} \tag{2.16}$$

where $0 \leq x \leq 1$ and p_{proj}^+ is the momentum of the projectile nucleus. For the pion, equation (2.15) becomes

$$y = \frac{1}{2}\ln\left(\frac{2(p_\pi^+)^2}{m_{\pi_\perp}^2}\right) = \ln\left(\frac{\sqrt{2}(xp_{proj}^+)}{m_{\pi_\perp}}\right) = y_{proj} - \ln\left(\frac{1}{x}\right) + \ln\left(\frac{M}{m_{\pi_\perp}}\right) \tag{2.17}$$

where the rapidity of the projectile nucleus is $y_{proj} = \ln(\frac{\sqrt{2}p_{proj}^+}{M})$. We will consider two regimes: central rapidity (near $y = 0$), and rapidities near the beam rapidity.

[1] Rapidity is related to the direction and momentum of a particle, ranging from $-\infty$ for a particle travelling down the negative beam axis to $+\infty$ for particles travelling down the positive beam axis. A particle travelling purely in the transverse plane will have a rapidity of zero. Rapidity is particularly useful because it is additive under Lorentz boosts.

The former corresponds to $p_z = 0$, or equivalently in the above formulation $p^+ = \frac{m_\perp}{\sqrt{2}}$, since

$$y = \frac{1}{2}\ln\left(\frac{2(p_\pi^+)^2}{m_{\pi\perp}^2}\right) = \frac{1}{2}\ln\left(\frac{2(\frac{m_\perp}{\sqrt{2}})^2}{m_{\pi\perp}^2}\right) = \frac{1}{2}\ln(1) = 0 \tag{2.18}$$

However, this corresponds to

$$x = \frac{m_\perp}{\sqrt{2}p_{proj}^+} = \frac{m_\perp}{\sqrt{s}} \tag{2.19}$$

which in the high-energy limit, where our concerns lie, gives $x \ll 1$. Thus, we are safe to approximate the particle production at central rapidity to be primarily due to the small-x particles, predominantly gluons as we saw in figure (2.1). Conversely, particles that have rapidity close to the beam rapidity after the collision, correspond to particles for which,

$$-\ln\left(\frac{1}{x}\right) + \ln\left(\frac{M}{m_\perp}\right) \approx 0 \tag{2.20}$$

$$x \approx \frac{m_\perp}{M} = \frac{\sqrt{m^2 + \boldsymbol{p}_\perp{}^2}}{M} \tag{2.21}$$

Consider the valence partons, which make up the a large portion of the mass of the nuclei, i.e. $m \approx M$. In this case, $p_\perp \approx 0$, meaning that very little transverse momentum was transferred and the particles continue virtually undisturbed along the light cone. This is the large x ($x \approx 1$) scenario, and provides some justification for the large x eikonal source approximation mentioned above. Alternatively, one can think of the dominant source of parton production as bremstrahlung for which, at weak coupling, the typical momentum transfer is soft, leaving the source, i.e. valence partons, as recoil-less sources moving along the light cone [15].

Either way, the system left behind is made up of strong classical gluon fields. At these high energies the gluon fields are extremely strong and thus can be treated classically since quantum corrections will be negligible. In particular, the high gluon density limit corresponds to classical fields because, in this case, the commutator of creation and annihilation operators is negligible compared to the large occupation number [12],

$$[a_k, a_k^\dagger] = 1 \ll a_k^\dagger a_k = N_k \tag{2.22}$$

QED provides an intuitive analogy. Consider a highly occupied system of photons. In this case, one need not consider the quantum corrections from QED, and Maxwell's equations describe the system quite well. The same is true of the gluon occupancy in the CGC and thus we only consider the classical Yang-Mills equations.

In order to determine the form of the initial fields, and their subsequent evolution, we will need the equations of motion, the classical Yang Mills equations, to be discussed in the next section.

2.3 Classical Yang Mills (CYM) Field

The Yang-Mills equations generalize Maxwell's equations of electromagnetism to the case of multiple charges, meaning that charge becomes a multi-dimensional complex vector space, rather than just the scalar electric charge of E&M. In the case of QCD, we have three charges, typically referred to as red, green, and blue, and thus we are concerned with the SU(3) YM equations. By varying the CGC action in equation (2.4) we arrive at the YM equations of motion,

$$[D_\mu, F^{\mu\nu}]_a = J_a^\nu \tag{2.23}$$

where the source term in the context of HIC's is given by (2.11). Again, the EOM are reminiscent of Maxwell's equations but with an additional SU(3) color index. This simple difference of gauge group has profound implications for the theory. For one, the theory is non-abelian, meaning fields are matrix valued and do not commute with one another. This in turns leads to the non-linearity of the equations, since, as is apparent in the covariant derivative, there will be commutator terms that are non-linear in the gauge fields. In terms of physics, this means that gluons, the QCD gauge bosons, interact with one another, leading to many additional vertices and diagrams that greatly complicate perturbative calculations. Furthermore, this non-linearity destroys the superposition principle that is so useful in regular electrodynamics.

Of course, the non-Abelian nature of the YM equations leads to other profound effects such as the negative beta function in the renormalization group flow that in

turn leads to asymptotic freedom. These topics account for the rich complexity of QCD, but are not the subject of this thesis. For now, we move on to deriving the form of the field strength tensor and CYM equations in $\tau - \eta$ coordinates.

2.3.1 Derivation of Field Strength in $\tau - \eta$ Coordinates

In order to use the CYM equations to evolve the system after the collision ($\tau > 0$), it is necessary to first clarify the form of the field strength tensor. We will begin in light-cone coordinates, which we will use for the gauge fields prior to the collision, and convert to $\tau - \eta$ coordinates, since these will be more convenient after the collision. The new variables τ and η are defined by

$$\tau = \sqrt{t^2 - z^2} \tag{2.24}$$

$$\eta = \frac{1}{2} \ln \left(\frac{t+z}{t-z} \right) \tag{2.25}$$

where t is the usual time coordinate ant z is the usual spatial coordinate, taken to be the beam direction. Beginning our derivation with

$$F^{i\pm} = \partial^i A^\pm - \partial^\pm A^i - ig[A^i, A^\pm] \tag{2.26}$$

In anticipation of a later discussion, we will take the following ansatz in the forward light cone ($\tau > 0$) consistent with the gauge choice $A^\tau = (x^- A^+ + x^+ A^-)/\tau = 0$

$$A^+ = x^+ \alpha(\tau, \mathbf{x}_\perp) \tag{2.27}$$

$$A^- = -x^- \alpha(\tau, \mathbf{x}_\perp) \tag{2.28}$$

$$A^i = \alpha_3^i(\tau, \mathbf{x}_\perp) \tag{2.29}$$

Substituting these expressions into (2.26) and lowering the index on the derivative in the middle term gives (refer to appendix (7.1) for a review of the metric in light cone coordinates),

$$F^{i\pm} = \partial^i(\pm x^\pm \alpha) - \partial^\pm \alpha_3^i - ig[\alpha_3^i, \pm x^\pm \alpha] = \partial^i(\pm x^\pm \alpha) - g_{\pm\mp}\partial^\pm \alpha_3^i - ig[\alpha_3^i, \pm x^\pm \alpha] \quad (2.30)$$

$$F^{i\pm} = \partial^i(\pm x^\pm \alpha) - \partial_\mp \alpha_3^i - ig[\alpha_3^i, \pm x^\pm \alpha] \quad (2.31)$$

Expanding the light cone derivatives in terms of $\tau - \eta$ coordinate derivatives by using the chain rule,

$$F^{i\pm} = \pm x^\pm \partial^i \alpha - \frac{\partial \tau}{\partial x^\mp}\partial_\tau \alpha_3^i - ig[\alpha_3^i, \pm x^\pm \alpha] \quad (2.32)$$

Pulling out a factor of $\pm x^\pm$ out of the first and third terms, which we can do since $x^\pm$ is simply a number,

$$F^{i\pm} = \pm x^\pm (\partial^i \alpha - ig[\alpha_3^i, \alpha]) - \frac{\partial \tau}{\partial x^\mp}\partial_\tau \alpha_3^i \quad (2.33)$$

But,

$$\frac{\partial \tau}{\partial x^\mp} = \frac{\partial}{\partial x^\mp}\sqrt{2x^+x^-} = \frac{1}{2}\frac{2x^\pm}{\sqrt{2x^+x^-}} = \frac{x^\pm}{\tau} \quad (2.34)$$

which leaves us with

$$F^{i\pm} = -x^\pm \left(\mp \partial^i \alpha \pm ig[\alpha_3^i, \alpha] + \frac{1}{\tau}\partial_\tau \alpha_3^i\right) = -x^\pm \left(\mp [D^i, \alpha] + \frac{1}{\tau}\partial_\tau \alpha_3^i\right) \quad (2.35)$$

Following the same procedure for the pure light-cone gauge components,

$$F^{+-} = -F^{-+} = \partial^+ A^- - \partial^- A^+ - ig[A^+, A^-] = \partial^+ A^- - \partial^- A^+ \quad (2.36)$$

where the commutator vanishes because

$$[A^+, A^-] = [x^+\alpha, -x^-\alpha] = -x^+x^-[\alpha, \alpha] = 0 \quad (2.37)$$

This leaves us with,

$$\begin{aligned} F^{+-} &= \partial^+(-x^-\alpha) - \partial^-(x^+\alpha) \\ &= \frac{\partial\tau}{\partial x^-}\partial_\tau(-x^-\alpha) - \frac{\partial\tau}{\partial x^+}\partial_\tau(x^+\alpha) \\ &= \frac{x^+}{\tau}\partial_\tau(-x^-\alpha) - \frac{x^-}{\tau}\partial_\tau(x^+\alpha) \\ &= \frac{-x^-x^+}{\tau}\partial_\tau\alpha - \frac{x^+}{\tau}\frac{\tau}{x^+}\alpha - \frac{x^-x^+}{\tau}\partial_\tau\alpha - \frac{x^-}{\tau}\frac{\tau}{x^-}\alpha \\ &= -2\frac{x^-x^+}{\tau}\partial_\tau\alpha - 2\alpha \\ &= -\frac{1}{\tau}\partial_\tau(\tau^2\alpha) \end{aligned} \tag{2.38}$$

where again we have used $\frac{\partial x^\pm}{\partial\tau} = \frac{\tau}{x^\mp}$. Finally, for the purely transverse coordinates,

$$F^{ij} = \partial^i\alpha_3^j - \partial^j\alpha_3^i - ig[\alpha_3^i, \alpha_3^j] \tag{2.39}$$

Now that we have the form of the field strength tensor, we can derive the EOM's from the CYM equations.

2.3.2 Derivation of CYM EOM's in $\tau - \eta$ Coordinates

In the forward light cone, where our interests lie, there are no source terms, so we need only worry about the homogeneous CYM equations. Again, we will begin in light cone coordinates and convert to $\tau - \eta$, since these will be more convenient after the collision. Beginning with the x^+ direction

$$[D_\mu, F^{\mu+}] = 0 \tag{2.40}$$

$$\partial_- F^{-+} - ig[A^+, F^{-+}] + [D_i, F^{i+}] = 0 \tag{2.41}$$

Converting derivatives to $\tau - \eta$ coordinates and using the expressions that we found for the field strength components, we have,

$$\frac{\partial\tau}{\partial x^-}\partial_\tau\left(\frac{1}{\tau}\partial_\tau(\tau^2\alpha)\right) - ig\left[x^+\alpha, \frac{1}{\tau}\partial_\tau(\tau^2\alpha)\right] + \left[D_i, -x^+\left(-[D^i, \alpha] + \frac{1}{\tau}\partial_\tau\alpha_3^i\right)\right] = 0 \tag{2.42}$$

$$\frac{x^+}{\tau}\left\{\partial_\tau\left(\frac{1}{\tau}\partial_\tau(\tau^2\alpha)\right) - ig\left[\alpha,\partial_\tau(\tau^2\alpha)\right] + \tau\left[D_i,[D^i,\alpha]\right] - [D_i,\partial_\tau\alpha_3^i]\right\} = 0 \quad (2.43)$$

Dividing out the $\frac{x^+}{\tau}$ factor, carrying out the τ derivative in the second term and raising the index on the first covariant derivative in the third term,

$$\partial_\tau\left(\frac{1}{\tau}\partial_\tau(\tau^2\alpha)\right) - ig\tau^2[\alpha,\partial_\tau\alpha] - \tau\left[D^i,[D^i,\alpha]\right] - [D_i,\partial_\tau\alpha_3^i] = 0 \quad (2.44)$$

For the analogous term, in the x^- direction,

$$[D_\mu, F^{\mu-}] = 0 \quad (2.45)$$

$$\partial_+ F^{+-} - ig[A^-, F^{+-}] + [D_i, F^{i-}] = 0 \quad (2.46)$$

Following a nearly identical procedure as above, we ultimately find,

$$-\partial_\tau\left(\frac{1}{\tau}\partial_\tau(\tau^2\alpha)\right) - ig\tau^2[\alpha,\partial_\tau\alpha] + \tau\left[D^i,[D^i,\alpha]\right] - [D_i,\partial_\tau\alpha_3^i] = 0 \quad (2.47)$$

These are the same four terms that showed up in the expression for $[D_\mu, F^{\mu+}] = 0$, except the signs are different. We can add and subtract these two results to get two simplified equations. Adding them gives

$$ig\tau^2[\alpha,\partial_\tau\alpha] + [D_i,\partial_\tau\alpha_3^i] = 0 \quad (2.48)$$

while subtracting yields,

$$\partial_\tau\left(\frac{1}{\tau}\partial_\tau(\tau^2\alpha)\right) - \tau\left[D^i,[D^i,\alpha]\right] = 0 \quad (2.49)$$

The last result is commonly expressed as

$$\frac{1}{\tau^3}\partial_\tau\tau^3\partial_\tau\alpha - \left[D^i,[D^i,\alpha]\right] = 0 \quad (2.50)$$

So far we have derived expressions for two of the three light cone CYM equations in terms on the initial gauge fields after the collision. For the last one,

$$[D_\mu, F^{\mu i}] = [D_+, F^{+i}] + [D_-, F^{-i}] + [D_j, F^{ji}] = 0 \tag{2.51}$$

Once again plugging in our expressions for the field strength components,

$$\partial_+ \left(x^+ \left(-[D^i, \alpha] + \frac{1}{\tau}\partial_\tau \alpha_3^i \right) \right) - ig \left[-x^- \alpha, x^+ \left(-[D^i, \alpha] + \frac{1}{\tau}\partial_\tau \alpha_3^i \right) \right]$$

$$+ \partial_- \left(x^- \left([D^i, \alpha] + \frac{1}{\tau}\partial_\tau \alpha_3^i \right) \right) - ig \left[x^+ \alpha, x^- \left([D^i, \alpha] + \frac{1}{\tau}\partial_\tau \alpha_3^i \right) \right] + [D_j, F^{ji}] = 0 \tag{2.52}$$

and applying the derivatives,

$$-[D^i, \alpha] + \frac{1}{\tau}\partial_\tau \alpha_3^i + x^+ \frac{\partial \tau}{\partial x^+} \partial_\tau \left(-[D^i, \alpha] + \frac{1}{\tau}\partial_\tau \alpha_3^i \right) - ig \left[-x^- \alpha, x^+ \left(-[D^i, \alpha] + \frac{1}{\tau}\partial_\tau \alpha_3^i \right) \right]$$

$$+ [D^i, \alpha] + \frac{1}{\tau}\partial_\tau \alpha_3^i + x^- \frac{\partial \tau}{\partial x^-} \partial_\tau \left([D^i, \alpha] + \frac{1}{\tau}\partial_\tau \alpha_3^i \right) - ig \left[x^+ \alpha, x^- \left([D^i, \alpha] + \frac{1}{\tau}\partial_\tau \alpha_3^i \right) \right] - [D^j, F^{ji}] = 0 \tag{2.53}$$

Combining like terms, making cancellations, and simplifying a bit,

$$\frac{2}{\tau}\partial_\tau \alpha_3^i + 2\frac{x^+ x^-}{\tau} \partial_\tau \left(\frac{1}{\tau}\partial_\tau \alpha_3^i \right) - 2igx^+ x^- \left[\alpha, [D^i, \alpha] \right] - [D^j, F^{ji}] = 0 \tag{2.54}$$

$$\frac{2}{\tau}\partial_\tau \alpha_3^i + \tau \partial_\tau \left(\frac{1}{\tau}\partial_\tau \alpha_3^i \right) - ig\tau^2 \left[\alpha, [D^i, \alpha] \right] - [D^j, F^{ji}] = 0 \tag{2.55}$$

Finally, we can combine the first two terms into one,

$$\frac{1}{\tau}\partial_\tau \tau \partial_\tau \alpha_3^i - ig\tau^2 \left[\alpha, [D^i, \alpha] \right] - [D^j, F^{ji}] = 0 \tag{2.56}$$

We have derived the boost invariant CYM equations of motion in the forward light cone. In order to utilize these equations to evolve the system in the forward light

cone, we need to find the boundary conditions on the light cone to initialize the gauge fields after the collision, which will be done in the next section.

2.3.3 Gauge Field due to a Single Nucleus

Sampling the charge distribution provides the source term to solve the classical Yang-Mills equations (eq. (2.23)). As mentioned earlier, these sources represent the hard partons that source the soft partons, i.e. the classical color fields, and travel along the light cone. In terms of the sampled charge density, the current can be written,

$$J_a^{+(-)} = g\rho_a(x^{-(+)}, \boldsymbol{x}_\perp) \tag{2.57}$$

Before the collision, each nucleus is a thin sheet of color charge travelling near the speed of light. In this picture, the sources are confined to the nuclei and thus the solution must solve the free equations of motion everywhere outside of these narrow sheets.

We aim to argue that the pre-collision fields satisfy 2-dimensional Poisson equations. The following discussion relies heavily on the reasoning of [16] but the original results were obtained in [15, 17, 18, 19]. Considering the source J^+ for the moment, and choosing covariant gauge initially , i.e.,

$$\partial_\mu A_C^\mu = 0 \tag{2.58}$$

we can find a solution in region 1 (see figure (2.3.3) for meaning of regions 1-4, as referred to throughout this section), for which $A_C^- = A_C^i = 0$. Here, the subscript C is a reminder that we are working in covariant gauge. The only non-vanishing component of the field strength tensor is

$$F^{i+} = \partial^i A_C^+ - \partial^+ A_C^i + g f^{abc} A_C^i A_C^+ = \partial^i A_C^+ \tag{2.59}$$

The gauge field in the x^+-direction can be determined via the CYM equations,

$$[D_i, F^{i+}] = J^+ \tag{2.60}$$

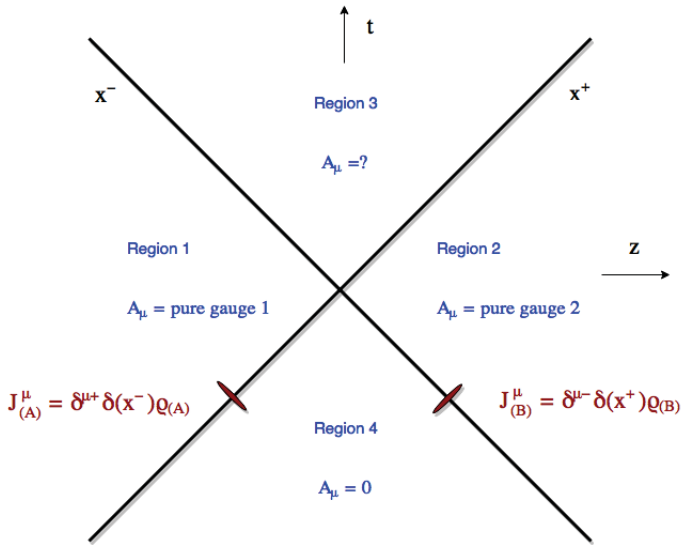

Figure 2.2: The fields are pure gauge in regions 1 and 2. The forward light cone is labeled as region 3 and represents the post-collision region of space time that are causally connected to the collision. The regions indicated in this figure are referred to throughout this section.

$$\left[(\partial_i - igA_{Ci}), \partial^i A_C^+\right] = \partial_i \partial^i A_C^+ - ig[A_{Ci}, \partial^i A_C^+] = \partial_i \partial^i A_C^+ = J^+ \tag{2.61}$$

where $i = 1, 2$ and the commutator term vanished because $A^i = 0$. Thus the gauge field satisfies a two-dimensional Poisson equation,

$$-\nabla_\perp^2 A_C^+ = J^+ = g\rho(x^-, \boldsymbol{x}_\perp) \tag{2.62}$$

Or equivalently, as is often written in the literature,

$$A_C^+ = \frac{-g\rho(x^-, \boldsymbol{x}_\perp)}{\nabla_\perp^2} \tag{2.63}$$

where we require the gauge fields to go to zero as $\boldsymbol{x}_\perp$ approaches infinity. Of course, for the current moving in the x^--direction, we have an analogous solution for region 2,

$$A_C^- = \frac{-g\rho(x^+, \boldsymbol{x}_\perp)}{\nabla_\perp^2} \tag{2.64}$$

Now that we have the gauge field in covariant gauge prior to the collision in regions 1 and 2, we can gauge transform to light-cone gauge, $A^+ = 0$. Doing so in region 1 gives

$$A^i_{(A)} = \frac{i}{g} V_{(A)} \partial^i V^\dagger_{(A)} \tag{2.65}$$

$$A^- = 0 \tag{2.66}$$

$$i\partial_- V^\dagger_{(A)} = g\Lambda V^\dagger_{(A)} \tag{2.67}$$

where $V_{(A)}$ is a gauge transformation matrix. Recalling that the gauge fields transform as

$$A^a_\mu(x)t^a \to V(x)(A^a_\mu(x)t^a + \frac{i}{g}\partial_\mu)V^\dagger(x) \tag{2.68}$$

we can see that equation (2.65) is pure gauge. Defining $\Lambda = A^+_C$ and solving equation (2.67), one can show

$$V = \mathrm{P}\ \exp\left[ig\int_{-\infty}^{x^-} \Lambda(z^-, \boldsymbol{x}_\perp)dz^-\right] \tag{2.69}$$

where P refers to the path ordering of the exponent. Plugging this result into equation (2.65) and replacing Λ with the right hand side of the Poisson equation (2.63), one finally finds,

$$A^i = i\left(\mathrm{P}\ \exp\left[ig\int_{-\infty}^{x^-} \frac{-1}{\nabla^2_\perp}\rho(z^-, \boldsymbol{x}_\perp)dz^-\right]\right)\nabla^i\left(\mathrm{P}\ \exp\left[ig\int_{-\infty}^{x^-} \frac{-1}{\nabla^2_\perp}\rho(z^-, \boldsymbol{x}_\perp)dz^-\right]\right)^\dagger \tag{2.70}$$

This amazing result allows us to relate the charge density, which will be sampled randomly for each nucleus, to the initial gauge fields by a pure gauge transform that relies on the solution to Poisson's equation. Now, we need to relate these pre-collision gauge fields to the post-collision fields, which will be done in the next section.

2.3.4 Initial Gauge Fields of Two 2-D Colliding Nuclei

For two nuclei, we simply sum two sources, moving in opposite directions on the $x^+$and x^- axes, respectively,

$$J = g\rho_A(x^-, \boldsymbol{x}_\perp) + g\rho_B(x^+, \boldsymbol{x}_\perp) \tag{2.71}$$

In this case,

$$A^{\pm} = 0 \tag{2.72}$$

$$A^i = \theta(x^-)\theta(-x^+)A^i_A(\boldsymbol{x}_\perp) + \theta(x^+)\theta(x^-)A^i_B(\boldsymbol{x}_\perp) \tag{2.73}$$

satisfy the equations of motion before the collision [19]. Here A_A and A_B are the pre-collision pure gauge fields associated with the two nuclei, A and B, respectively. The physical information is embedded in the discontinuity of the fields across the nuclei which gives the charge density and can be written, for $t < 0$,

$$\nabla_i A^i_{A(B)} = \rho_{A(B)}(\boldsymbol{x}_\perp) \tag{2.74}$$

Intuitively, the form of (2.73) makes sense as the gauge field due to two 2-dimensional nuclei travelling at the speed of light. Since the nuclei are moving at the speed of light, their fields cannot precede them and are pure gauge in their wake. Thus, there is only the transverse gauge fields that travel along with their respective nuclei at the speed of light. Due to their different charge configurations, the gauge fields from the two nuclei differ.

As a consequence of this solution (eq. (2.72) and (2.73)), the field strength components F^{ij} vanish. This solution is exact at all points in spacetime that are causally disconnected from the collision point, i.e. regions 1 and 2 in (2.3.3). It remains to determine the form of A_A and A_B from the initial charge density, which will be done in the next section.

After the collision, the solution is no longer pure gauge. When we are not on the light cone, but in any of the four regions in figure (2.3.3), there are no source terms since they are considered to remain on the light cone and thus the fields satisfy the homogeneous field equations. We will work in Schwinger gauge,

$$x^- A^+ + x^+ A^- = 0 \tag{2.75}$$

and take the ansatz already referred to in equations (2.27)-(2.28) in the forward light cone ($x^+ > 0$ and $x^- > 0$), where our interests lie, [19]

$$A^+ = x^+\alpha(\tau, \boldsymbol{x}_\perp) \tag{2.76}$$

$$A^- = -x^-\alpha(\tau, \boldsymbol{x}_\perp) \tag{2.77}$$

$$A^i = \alpha_3^i(\tau, \boldsymbol{x}_\perp) \tag{2.78}$$

At this point, determining the fields after the collision becomes a boundary value problem. The two nuclei collide at $\tau = 0$, which connects the regions of space-time before and after the collision. In order to derive the initial conditions at this point, we match the expressions for the gauge field before and after the collision. As a reminder, the equations of motions, as derived in a previous section, are [18][19]

$$\frac{1}{\tau^3}\partial_\tau\tau^3\partial_\tau\alpha - [D^i, [D^i, \alpha]] = 0 \tag{2.79}$$

$$\frac{1}{\tau}[D_i, \partial_\tau\alpha_3^i] + ig\tau[\alpha, \partial_\tau\alpha] = 0 \tag{2.80}$$

$$\frac{1}{\tau}\partial_\tau\tau\partial_\tau\alpha_3^i - ig\tau^2[\alpha, [D^i, \alpha]] - [D^j, F^{ji}] = 0 \tag{2.81}$$

Plugging in the boundary condition and matching terms on the boundaries and eliminating any discontinuities is a tedious but straightforward exercise in algebra and gives the simple result relating the pre-collision pure gauge fields to the fields in the forward light cone after the collision. The Yang Mills equation $[D_\mu, F^{\mu i}] = 0$ has a delta function singularity on the light cone which requires

$$\alpha_3^i(\tau, \boldsymbol{x}_\perp)|_{\tau=0} = \alpha_1^i(\boldsymbol{x}_\perp) + \alpha_2^i(\boldsymbol{x}_\perp) \tag{2.82}$$

The other two equations of motion yield,

$$\alpha(\tau, \boldsymbol{x}_\perp)_{\tau=0} = -\frac{ig}{2}[\alpha_1^i(\tau, \boldsymbol{x}_\perp), \alpha_2^i(\tau, \boldsymbol{x}_\perp)] \tag{2.83}$$

Eliminating the α_i's to get the actual fields before and after the collision,

$$A^i(\tau, \boldsymbol{x}_\perp)|_{\tau=0} = A^i_A(\boldsymbol{x}_\perp) + A^i_B(\boldsymbol{x}_\perp) \tag{2.84}$$

$$A^+|_{\tau=0} = x^+\alpha(\tau, \boldsymbol{x}_\perp)|_{\tau=0} = -x^+\frac{ig}{2}[A^i_A(\tau, \boldsymbol{x}_\perp), A^i_B(\tau, \boldsymbol{x}_\perp)] \tag{2.85}$$

$$A^-|_{\tau=0} = -x^-\alpha(\tau, \boldsymbol{x}_\perp)|_{\tau=0} = x^-\frac{ig}{2}[A^i_A(\tau, \boldsymbol{x}_\perp), A^i_B(\tau, \boldsymbol{x}_\perp)] \tag{2.86}$$

Thus the initial condition in the forward light cone is uniquely determined by the pure gauge fields before the collision which in turn depend on the charge distributions. Before determining the pre-collision gauge fields, a few comments are in store. First, the equations of motions and their solutions are boost invariant, meaning that they are independent of the rapidity coordinate η, which will justify a 2+1D numerical simulation. This is the initial condition analogue to Bjorken's boost invariant formulation of hydrodynamic equations, and will allow for a fully boost invariant, 2+1D treatment of HIC's. Second, the formulation given above for the infinite momentum limit of HIC's gives exact solutions for the notoriously difficult to solve CYM equations.

In reality, this limit is a good approximation, but it is just that, an approximation. The boost invariant case corresponds to mid-rapidity, and is unable to produce data as a function of rapidity. Now that 3+1D hydrodynamic simulations are becoming more common, the field will certainly move toward 3+1D initial conditions and, in fact, is already beginning to do so [21].

2.4 Initial Fields from the Charge Density

At this point, the story should be relatively clear. We sample the color charge according to the IP-Sat model, from which we can determine the initial pure gauge fields before the collision, and ultimately the initial glasma fields immediately afterwards. However, we have not yet specified how to solve the Poisson equation to determine the pre-collision fields nor talked about sampling the color charge distribution. We

will determine the pre-collision fields here and leave the charge sampling discussion for section (2.7.1) on the IPSat model. Starting from equation (2.64),

$$-\nabla_\perp^2 A_a^{+(-)}(\boldsymbol{x}_\perp) = g\rho_a(x^{-(+)}, \boldsymbol{x}_\perp) \tag{2.87}$$

Suppressing the $x^\pm$ notation as well as the color index for the moment, the Fourier transform of equation (2.87) can be written,

$$A(\boldsymbol{k}_\perp) = \frac{g\rho(\boldsymbol{k}_\perp)}{{\boldsymbol{k}_\perp}^2} \tag{2.88}$$

Thus, the differential equation becomes an algebraic one. Solving equation (2.88) and taking the inverse Fourier transform gives us the gauge field as a function of the position in the transverse plane. Taking the path ordered exponential of the gauge field gives the Wilson Line in the fundamental representation, [22]

$$V(\boldsymbol{x}_\perp) = Pe^{i\int dx^- A^+(x^-, \boldsymbol{x}_\perp)} \tag{2.89}$$

which can be discretized as

$$V(\boldsymbol{x}_\perp) = \prod_{k=1}^{N_y} \exp\left\{\frac{-ig\rho(\boldsymbol{x}_\perp)}{\nabla_\perp^2 - m^2}\right\} \tag{2.90}$$

where m is an infrared cutoff taken to be $m = \lambda_{QCD} = 0.2$ GeV. This leaves out momentum modes below this "mass" scale and protects against infrared divergences. Alternatively, the cutoff can be thought of as incorporating color confinement on the nucleon level since it removes modes below the QCD scale that would be subject to such confinement. Thus, it effectively "confines" these modes to within the nucleon and we do not see free modes below this scale. The assumption is that modes at the saturation scale dominate the system and thus the system should be insensitive to this cutoff. Details on the numerical and physical significance of the infrared cutoff can be found [22].

Using the expression for the discretized Wilson line (2.90), along with equation (2.65), one gets the gauge fields of the pre-collision nuclei, $A^i_{A(B)}(\boldsymbol{x}_\perp)$ which are pure gauges outside of the light cone as mentioned above. Equation (2.90) will be

instrumental in determining the form of the links in the lattice formulation, as will be seen in eq. (2.108), and ultimately solving for the initial links in the future light cone. For now, we have outlined the theoretical procedure for determining the gauge fields of the glasma immediately after the collision. At this juncture, we move on to Hamiltonian formulation and the EOMs of the fields.

Summary of Gauge Field Determination

1. Sample charge density
2. Solve the CYM equations in covariant gauge (Results in Poisson equation)
3. Solve Poisson equation to find gauge fields prior to the collision in regions 1 and 2 (Fourier Transform and Inverse Fourier Transform)
4. Gauge transform to light cone gauge
5. Relate pre-collision pure gauge fields from step 2 to find gauge fields immediately after the collision in region 3 by matching on the light cone

2.5 Hamiltonian and Equations of Motion

Starting from the CGC action given in eq. (2.4) the Hamiltonian density in the boost invariant case can be written in terms of the 2+1D Yang-Mills Hamiltonian coupled to an adjoint scalar [23] [24],

$$H = \int dx_\perp \eta \{ \frac{1}{2\tau} E_i^a E_i^a + \frac{\tau}{4} F_{ij}^a F_{ij}^a + \frac{1}{2\tau} (D_i \phi)^a (D_i \phi)^a + \frac{\tau}{2} E_\eta^a E_\eta^a \} \quad (i = x, y) \tag{2.91}$$

where the integration over space-time rapidity has already been carried out, and the rapidity component of the gauge field is the scalar field,

$$A_\eta(\tau, \eta, \boldsymbol{x}_\perp) = x^- A^+ - x^+ A^- \approx \phi(\tau, \boldsymbol{x}_\perp) \tag{2.92}$$

and

$$E_a^i = \tau \partial_\tau A_i^a \tag{2.93}$$

$$E_a^\eta = \frac{1}{\tau}\partial_\tau A_\eta^a \tag{2.94}$$

Renaming the rapidity component of the electric field as the conjugate momentum of the scalar field, i.e. $\pi = E^\eta$, and taking a trace over the color indices, the Hamiltonian density can be written,

$$\mathcal{H} = \mathrm{Tr}\left\{\frac{1}{\tau}E^i E^i + \frac{\tau}{2}F_{ij}F_{ij} + \tau\pi^2 + \frac{1}{\tau}[D_i,\phi][D_i,\phi]\right\} \quad (i = x, y) \tag{2.95}$$

This expression can be discretized to [23] [24]

$$H = \sum_{\boldsymbol{x}_\perp}\left\{\frac{g^2}{\tau}\mathrm{Tr}(E^i E^i) + \frac{2N_c\tau}{g^2a^2}\left(1 - \frac{1}{N_c}\mathrm{Re}(\mathrm{Tr}(U_{xy}))\right) + \frac{\tau}{a^2}\mathrm{Tr}(\pi^2) + \frac{1}{\tau}\sum_i \mathrm{Tr}(\phi - \tilde{\phi}_i)^2\right\} \tag{2.96}$$

The terms correspond, from left to right, to the contributions due to the transverse electric field, the longitudinal magnetic field, the longitudinal electric field, and the transverse magnetic field, respectively. In this case, $\tilde{\phi}_i$ is the parallel transported field in the direction i. At the lattice site j, this is given by

$$\tilde{\phi}_{i,j} = U_{i,j}\phi_{j+\hat{i}}U_{i,j}^\dagger \tag{2.97}$$

where $U_{i,j} = \exp(igaA_{i,j})$ is the gauge link at lattice site j in the direction i. The other quantities are the lattice spacing, a, the number of colors, N_c, the coupling constant, g, and the plaquette in the transverse plane, $U_{xy} = U_{x,i}U_{y,i+\hat{x}}U_{x,i+\hat{y}}^\dagger U_{y,i}^\dagger$ defined by a closed loop of gauge links. Notice the distinction in notation between the gauge link at site j, in the direction i $U_{i,j}$, with the comma, and the plaquette in the x-y plane U_{xy}, without the comma. The plaquette and its physical meaning are discussed in greater detail in section (4.7). At initial time, the energy is given by the longitudinal fields only, [25]

$$\epsilon(\tau = 0) = \lim_{\tau\to 0^+}\frac{1}{\tau}\frac{dE}{d^2\boldsymbol{x}_\perp d\eta} = \frac{2}{g^2a^4}\left(N_c - \mathrm{Re}(\mathrm{Tr}(U_{xy}))\right) + \frac{1}{a^4}\mathrm{Tr}(\pi^2) \tag{2.98}$$

where the first term is due to the longitudinal magnetic field and the second is due to the longitudinal electric field.

One can get the equations of motion for the fields by taking the Poisson brackets between the fields and the Hamiltonian. The result is,

$$\dot{U_i} = i\frac{g^2}{\tau}E^i U_i \tag{2.99}$$

$$\dot{\phi} = \tau\pi \tag{2.100}$$

$$\dot{E^x} = \frac{i\tau}{2g^2}\left[U_{xy} + U_{x(-y)} - U_{xy}^\dagger - U_{x(-y)}^\dagger\right] - \text{trace} + \frac{\dot{\text{i}}}{\tau}[\tilde{\phi}_{\text{x}}, \phi] \tag{2.101}$$

$$\dot{E^y} = \frac{i\tau}{2g^2}\left[U_{yx} + U_{y(-x)} - U_{yx}^\dagger - U_{y(-x)}^\dagger\right] - \text{trace} + \frac{\dot{\text{i}}}{\tau}[\tilde{\phi}_{\text{y}}, \phi] \tag{2.102}$$

$$\dot{\pi} = \frac{1}{\tau}\sum_i \left[\tilde{\phi}_i + \tilde{\phi}_{-i} - 2\phi\right] \tag{2.103}$$

where there is no sum over i implied in eq. (2.99) and the dot on the left hand side of the equations refers to the time derivative of the dotted quantity. Also, "-trace" means subtract the diagonal elements, leaving the matrix traceless. For equations (2.101) and (2.102), the four plaquettes terms are the four possible 1×1 plaquettes starting at the lattice site in question. These equations of motion are discretized and evolved in time using the leap frog algorithm (see chapter (4.4)) to get the fields at all times. As we will see, it is important to be careful at initial times in order to avoid division by zero.

2.5.1 Initial Conditions on the Lattice

The initial conditions ($\tau = 0$) discussed in section (2.3.4) can be formulated on the lattice to be [23],

$$\text{Tr}\left[t^a((U_i^{(A)} + U_i^{(B)})(1 + U_i^{(3)\dagger}) - \text{h.c.})\right] = 0 \tag{2.104}$$

which corresponds to (2.82), as well as

$$E^i = 0 \tag{2.105}$$

$$\phi = 0 \tag{2.106}$$

$$\begin{aligned}\pi(\boldsymbol{x}_\perp) = \frac{-i}{4g}\sum_i \Bigg[&\left(U_i^{(3)}(\boldsymbol{x}_\perp) - 1\right)\left(U_i^{\dagger(B)}(x_\perp) - U_i^{\dagger(A)}(x_\perp)\right) \\ &+ \left(U_i^{\dagger(3)}(\boldsymbol{x}_\perp - e_i) - 1\right)\left(U_i^{(B)}(\boldsymbol{x}_\perp - e_i) - U_i^{(A)}(\boldsymbol{x}_\perp - e_i)\right) - \text{h.c.}\Bigg]\end{aligned} \tag{2.107}$$

where the last expression is the lattice expression for equation (2.83). The links $U^{(A)}$ and $U^{(B)}$ correspond to the pure gauge fields of the pre-collision nuclei and e_i is the unit vector on the lattice connecting neighboring points in the i direction. $U^{(3)}$ on the other hand is the link matrix for the color field A^i after the collision ($\tau \geq 0$). The index i takes values $1, 2$ corresponding to the transverse coordinates x and y, respectively. The pure gauge links are defined on the lattice by assigning two SU(3) matrices (see appendix (7.2)), $V_{1,j}$ and $V_{2,j}$, one for each incoming nucleus, at each lattice site [24]. Then the link variable at site i, in the direction j, due to nucleus q becomes

$$U^{(q)}_{i,\hat{j}} = V_{q,i}V^\dagger_{q,i+\hat{j}} = e^{i\Lambda_i^{(q)}}e^{-i\Lambda^{(q)}_{i+\hat{j}}} \tag{2.108}$$

where $\Lambda_i^{(q)}$ is the solution to the Poisson equation for nucleus q at site i, $\nabla_\perp^2\Lambda_{(q)} = -g\rho_{(q)}$. Thus, our stochastic sampling of the color charge gives us the fields of each nucleus before the collision. One still needs to solve equation (2.104) to get $U^{(3)}$, however. Since $U^{(3)}$ is an element of SU(3), solving equation (2.104) actually means solving $N_c^2 - 1 = 8$ equations. The procedure for doing so will be discussed in chapter (4.3).

In the meantime, one can show that equation (2.104) solves the non-lattice initial conditions. Expanding the links in the normal way to first order in the lattice spacing

$U_i = 1 + igaA_i$, for small a, equation (2.104) becomes,

$$\begin{aligned}
&\mathrm{Tr}\{t^a[(1+igaA_i^{(A)}+1+igaA_i^{(B)})(1+1-igaA_i) \\
&\qquad\qquad -(1-igaA_i^{(A)}+1-igaA_i^{(B)})(1+1+igaA_i)]\} = 0 \\
&\mathrm{Tr}\,\{t^a[\,(2+iga(A_i^{(A)}+A_i^{(B)}))(2-igaA_i) \\
&\qquad\qquad -(2-ig(aA_i^{(A)}+A_i^{(B)}))(2+igaA_i)\,]\} = 0
\end{aligned} \tag{2.109}$$

Keeping only terms up to linear order in the lattice spacing,

$$\mathrm{Tr}\{t^a[(4+2iga(A_i^{(A)}+A_i^{(B)})-2igaA_i)-(4-2iga(A_i^{(A)}+A_i^{(B)})+2igaA_i)]\} = 0 \tag{2.110}$$

and cancelling terms,

$$\mathrm{Tr}\{t^a[4iga(A_i^{(A)}+A_i^{(B)})-4igaA_i)]\} = 0 \tag{2.111}$$

The solution comports with our previous result from section (2.3.4), that is

$$A_i = A_i^{(A)} + A_i^{(B)} \tag{2.112}$$

Similarly, with a bit more effort, one can use the same expansion for the gauge link to show that (2.107) coincides with (2.83), as is done in [24].

2.6 Saturation Scale and Color Charge Density

In HIC's, the highly boosted nuclei radiate gluons via brehmstrahlung, but cannot do so indefinitely. There is always a finite probability that two gluons can recombine. At some point, the gluons become so closely packed within the nucleus that gluon recombination begins to compete with gluon splitting. This phenomenon is known as *gluon saturation* and occurs when the product of the gluon recombination cross section with the gluon surface density of the nucleus exceeds unity [7], [26]

$$\rho_g \sigma_{gg\longrightarrow g} \sim \alpha_s Q^{-2} \times \frac{xG(x,Q^2)}{A^{2/3}} \tag{2.113}$$

The saturation momentum, then, is the minimum momentum for which this condition is satisfied. Solving, one finds

$$Q_s^2 = \frac{\alpha_s xG(x,Q^2)}{A^{2/3}} \tag{2.114}$$

Below this scale, saturation effects play an important role in taming the growth of gluon density, i.e. saturating the system. Above this scale, however, gluon cascades are still relatively unimpeded and can continue to increase the gluon density. In order for saturation effects to become evident, the saturation scale Q_s must be sufficiently large. In this thesis, the form of the saturation scale will be in accordance with the IP-Sat Model. At LHC energies, this scale is in the 1-2 GeV range at 2.76 TeV and reaches about 2.3 GeV for 5.02 TeV.

In terms of Feynman diagrams, the saturation process can be seen in fig. (2.3). The figure shows gluon cascades and a single gluon recombination, circled in red. When the recombination probability equals the probability for further radiation, saturation is reached.

Figure 2.3: Gluon cascade and recombination highlighted in red circle. This figure was taken from [7]

To foreshadow a later discussion, it is worth noting that it is perfectly intuitive for the saturation scale to relate to the color charge density. This scale sets the energy below which the gluon density can no longer grow and thus controls the charge density. As we will see, in the IP-Glasma model the saturation scale and the color charge density are related simply by a constant of proportionality.

For sufficiently high energy, or equivalently, small enough x [12],

$$Q_s^2(x) \gg \Lambda_{QCD}^2 \tag{2.115}$$

since the gluon density grows rapidly as a function of x, as we saw in figure (2.1. This suggests a weakly coupled system, i.e. $\alpha_s^2 \ll 1$, and thus the opportunity to use perturbative techniques. One must be careful, however, in this case because the high gluon density compensates for the small coupling to amplify the interaction probability to order one. In the absence of perturbative techniques, an effective field

theory that integrates out the "fast" degrees of freedom, has been developed. This theory is the CGC, discussed already in section (2.2).

During the first $\tau \approx \frac{1}{Q_s}$ the system can be described by solutions to the classical field equations. After this time, the gluon fields starts to become dilute and the classical field approximation begins to lose applicability. Thus, the higher the energy, the longer the classical field approximation will provide an adequate description of the system.

2.6.1 Geometric Scaling

For a system that is localized in rapidity, the only dimensionful quantity to determine the scale of the problem at a given rapidity is the saturation scale $Q_s^2(x)$. Then, since QCD is approximately scale invariant, the typical partonic transverse momentum will also be of the order of $Q_s^2(x)$. If, in addition, the inverse of the saturation scale squared is significantly larger than the area of the hadron, i.e., [12]

$$Q_S^2(x) \sim \frac{1}{\lambda_S^2} \gg \frac{1}{R^2} \tag{2.116}$$

where R is the radius, then the hadron area can be taken to be effectively infinite, since the parton wavelength is far smaller than the radius of the hadron. This means that for small enough x, all hadrons behave similarly, meaning that specific features of the hadron enter only in the saturation scale $Q_s^2(x, A)$. In fact, this idea is supported by the following empirical parametrization of the saturation scale,

$$Q_s^2(x, A) \sim \frac{A^{1/3}}{x^\lambda} \tag{2.117}$$

where $\lambda \sim 0.2 - 0.3$. This suggests that processes like deep inelastic scattering, which is central to the IP-Sat model, should be universal functions of the ratio of the transferred momentum to the saturation scale. This is known as "geometric scaling" and will be crucial in justifying the applicability of deep inelastic scattering physics to heavy ions. This notion is also critical to the MV model which assumes infinitely large 2-dimensional nuclei, the justification for which depends on the argument for geometric scaling given above.

2.7 IP-Glasma

IP-Glasma is a Monte-Carlo event generator that determines the color charge distribution within the IP-Sat framework. From there, it determines the gauge fields and evolves them in time via the classical Yang Mills equations. Finally, IP-Glasma computes the stress-energy tensor, and diagonalizes it to find the energy density and local velocity that are relevant to initializing hydrodynamical simulations. Having already discussed the CYM equations, and leaving the stress energy tensor for the next chapter, this section will address the details of the IP-Sat model, the sampling of nucleons, and the determination of the color charge density in the pre-collision nuclei.

2.7.1 IP-Sat Model

The Impact Parameter Dipole Saturation model [3], or IP-Sat, describes deep inelastic scattering in which a virtual photon(gluon) fluctuates into a quark-antiquark dipole, undergoes elastic scattering with a proton, and recombines into a photon (gluon). It improves upon the Golec-Biernat and Wusthoff (GBW) dipole saturation model by introducing a proton impact parameter dependence into the dipole dynamics and incorporating DGLAP into the dipole cross-section in order to extend the model to the high Q^2 regime.

The total cross section for the quark-antiquark dipole to interact with the gluon cloud in the proton is proportional to the area of the dipole πr^2, the strong coupling constant α_s, and the number of gluons per color charge in the cloud $\frac{xg(x,\mu^2)}{N_c}$,

$$\sigma_{q\bar{q}} = \frac{\pi^2}{N_c} r^2 \alpha_s(\mu^2) x g(x, \mu^2) \tag{2.118}$$

where $xg(x, \mu^2)$ is the gluon distribution function for momentum fraction x, at the scale μ^2. If we assume the dipole cloud in the proton to be extremely dense, as it would be in the CGC framework, and divide the proton into thin slices of thickness dz, then the probability that a dipole, at impact parameter b, does not undergo an inelastic interaction while traversing one slice of the proton is,

$$P(b) = 1 - \frac{\pi^2}{N_c} r^2 \alpha_s(\mu^2) x g(x, \mu^2) \rho(b, z) dz \tag{2.119}$$

where $\rho(b,z)$ is the gluon density inside of the proton and is normalized to unity, i.e., $\int d^2b dz \rho(b,z) = 1$. For the full proton, this probability becomes,

$$|S(b)|^2 = \exp\left\{-\frac{\pi^2}{N_c} r^2 \alpha_s(\mu^2) x g(x,\mu^2) T(b)\right\} \tag{2.120}$$

where $T(b) = \int dz \rho(b,z)$. Assuming the S-matrix element is mostly real, the differential cross section is given by,

$$\frac{d\sigma_{\bar{q}q}}{d^2b} = 2\left[1 - \exp\left(-\frac{\pi^2}{2N_c} r^2 \alpha_s(\mu^2) x g(x,\mu^2) T(b)\right)\right] \tag{2.121}$$

The impact parameter dependence is introduced through the proton thickness function $T(b)$, which is taken to be gaussian and normalized to unity,

$$T(b) = \frac{1}{2\pi B_G} \exp\left(-b^2/2B_G\right) \tag{2.122}$$

where $B_G = 4$ GeV^2 is fit to HERA diffractive data, and b is the proton impact parameter. Looking at the differential cross section as a function of impact parameter for different values of the the dipole size, we can see that the total cross section given above begins to plateau, i.e. saturate, and does so at larger values of b for larger dipole sizes.

Instead of thinking of saturation occurring below a certain energy level, one can alternatively think of saturation occurring at a given dipole size, meaning as the saturation scale increases, only smaller and smaller dipoles will "fit" inside the nucleus. This idea is illustrated schematically in figure (2.4) and a bit more quantitatively in figure (2.5).

The gluon distribution function, $xg(x,\mu^2)$, is initialized at the scale $\mu_0^2 = 1\,\text{GeV}^2$ via

$$x g(x,\mu_0^2) = A_g x^{-\lambda_g} (1-x)^{5.6} \tag{2.123}$$

where $A_g = 2.308$, and $\lambda_g = 0.058$ have been fitted to deep inelastic scattering (DIS) data [27]. The momentum fraction of individual partons, x, is taken to be $x = \frac{\langle p_T \rangle}{\sqrt{s}}$, where the average transverse momentum $\langle p_T \rangle$ is from a fit done by the

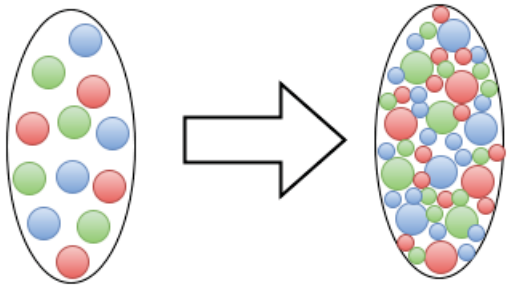

Figure 2.4: Schematic figure showing the increasing gluon density inside a nucleon as energy increases (lower energy on left, higher energy on right). The circles represent gluons of different colors and sizes within the nucleon.

CMS collaboration of charged hadrons as a function of the center of mass energy $\sqrt{s}$ [11],

$$\langle p_T \rangle = 0.413 - 0.0171 \ln s + 0.00143(\ln s)^2 \tag{2.124}$$

The scale can be related to the dipole radius via $\mu^2 = \frac{4}{r_\perp^2} + \mu_0^2$. Finally, the strong coupling at leading order is

$$\alpha_s(\mu^2) = \frac{12\pi}{(33 - 2N_f)\ln(\mu^2/\Lambda_{QCD}^2)} \tag{2.125}$$

where $N_f = 3$ and $\lambda_{QCD} = 0.2$GeV for the purposes of this thesis.

The gluon density, having been initialized in equation 2.123, is evolved from the initial scale μ_0^2 to μ^2 using leading order Dokshitzer-Gribov-Lipatov-Altarelli-Parisi (DGLAP) evolution equations [28, 29, 30] in the absence of quarks, [1]

$$\frac{\partial x g(x,\tilde{\mu}^2)}{\partial \log \tilde{\mu}^2} = \frac{\alpha_S(\tilde{\mu}^2)}{2\pi} \int_x^1 dz P_{gg}(z) \frac{x}{z} g(\frac{x}{z}, \tilde{\mu}^2) \tag{2.126}$$

where P_{gg} is the gluon splitting function with $N_f = 3$ flavors, $C_A = 3$, and $T_R = 1$,

$$P_{gg}(z) = 6\left[\frac{z}{(1-z)} + \frac{1-z}{z} + z(1-z)\right] + (\frac{11}{2} - \frac{N_f}{3})\delta(1-z) \tag{2.127}$$

For the purposes of this thesis, these equations are solved using a software written by Francois Gelis [31]. It solves the integro-differential DGLAP equations by expanding parton distributions and splitting functions in Laguerre polynomials, thereby reducing the problem to a set of ordinary differential equations defined by recurrence.

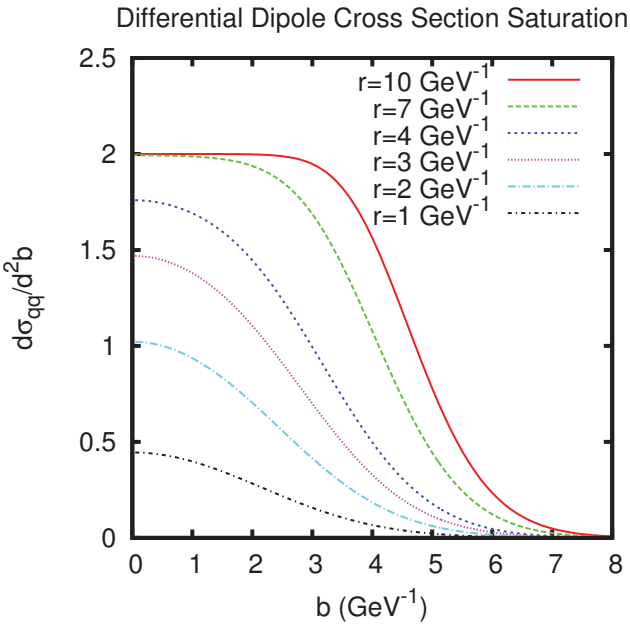

Figure 2.5: The differential dipole cross section as a function of impact parameter for different proton sizes saturating at 2.

In the CGC, there is a high gluon density, and the interaction probability for DIS approaches unity. In the IP-Glasma model, the saturation radius, r_s, is taken to be the dipole size for which the proton size becomes one interaction length. This corresponds to setting the exponent of equation (2.121) equal to 1/2. More specifically we mean,

$$\left(\frac{\pi^2}{2N_c} r^2 \alpha_s(\mu^2) x g(x,\mu^2) T(b)\right)\Bigg|_{r=r_s} = \frac{1}{2}. \tag{2.128}$$

This equation can be solved iteratively to find the value of r that meets this criterion. For this thesis, Brent's Method, a root finding algorithm that combines several less sophisticated methods for optimal efficiency and reliability, was used (see section (4.5) for details).

From there, the radius can be related to the saturation scale via

$$Q_{s,p}^2 = \frac{2}{r_s^2} \tag{2.129}$$

where the subscript p refers to the fact that is in the saturation scale for a single proton. To compare with the saturation scale condition given in equation (2.114),

plugging above into dipole saturation cross section, gives

$$\frac{\pi^2}{2N_c} r^2 \alpha_s(\mu^2) x g(x,\mu^2) T(b) = \frac{\pi^2}{N_c Q_{s,p}^2} \alpha(\mu^2) x g(x,\mu^2) T(b) = 1 \tag{2.130}$$

which, solving for Q_s,

$$Q_{s,p}^2 = \frac{\pi^2}{N_c} \alpha(\mu^2) x g(x,\mu^2) T(b) \sim \frac{\rho_g \alpha_s(\mu^2)}{A_{\text{dipole}}} \tag{2.131}$$

where the thickness function is a two dimensional Gaussian that acts as the inverse of the spatial area of the dipole, $1/A_{\text{dipole}}$.

From this, the saturation scale for each nucleus is computed by summing the contribution from each nucleon at a given point in the transverse plane. This depends on the spatial distribution of nucleons, which will be discussed in the next section. The saturation scale is directly related to the color charge squared per unit area, $g^2\mu_{(A)}^2(x, \boldsymbol{b}_\perp)$, via,

$$Q_{s(A)}^2(x, \boldsymbol{b}_\perp) = C g^2 \mu_{(A)}^2(x, \boldsymbol{b}_\perp) \tag{2.132}$$

where C is simply a constant of proportionality that is used to fit the overall energy density to give the proper multiplicity after hydrodynamics and UrQMD simulations. This has been fit to the $0-5\%$ centrality bin for a given center of mass energy in this thesis and has been determined to be $C = 0.49$ for 2.76 TeV and $C = 0.51$ for 5.02 TeV. The subscript (A) in equation (2.132) takes values 1 and 2, corresponding to the two incoming nuclei. It has been argued in [22] that this relationship between the saturation scale and color charge density should be $C \approx 0.6$ but, as discussed in this reference, there is a complicated numerical interplay between the longitudinal discretization, the infrared cutoff m used in the solution of the Poisson equation, and C. The initial implementation of IP-Glasma used this parameter to fix the multiplicity, as is done here, and obtained a value of $C = 0.75$ [1].

Having determined the saturation scale squared for both nuclei, plotted in fig. (2.6) for one nucleus, and thus the average squared color charge density, it is still not clear how the color charge is distributed within each nucleus. The IP-Glasma model samples the average color charge stochastically from a Gaussian distribution on an

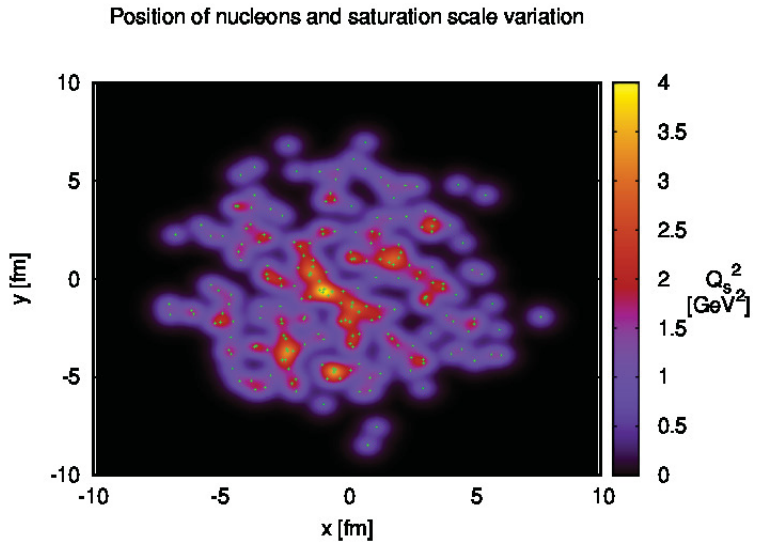

Figure 2.6: Position of nucleons and saturation scale variation in the IP-Glasma framework for an ultra-central 0-1% Pb-Pb collision at 2.76 TeV

event-by-event basis as will be seen in the next section. This is a key feature of the model that introduces sub-nucleonic color charge fluctuations.

2.7.2 *Alternative x Determination*

The above discussion presents the simplest method of determining x, but simply gives a constant value throughout the nuclei. In reality, x should depend on the transverse coordinate, $x(\boldsymbol{x}_\perp)$, since the value of x should vary from gluon to gluon. Thus there is also an implementation where $x(\boldsymbol{x}_\perp) = \frac{Q_s(\boldsymbol{x}_\perp)}{\sqrt{s}}$ is now a function of position in the transverse plane [32]. This is a far more realistic implementation and will introduce additional fluctuations. In this case, the thickness functions of individual nucleons is summed to give a total thickness function,

$$T_{total}(b) = \sum_{i=1}^{A} T_i(b) \tag{2.133}$$

where A is the number of nucleons in a given nucleus. This form for the thickness function makes the differential cross section, given in (2.121)

$$\frac{d\sigma_{\bar{q}q}}{d^2b} = 2\left[1 - \exp\left(-\frac{\pi^2}{2N_c}r^2\alpha_s(\mu^2)xg(x,\mu^2)\sum_{i=1}^{A}T(b)\right)\right] \tag{2.134}$$

Note that in the previous case, we determined the saturation scale for an individual nucleon and then summed the contributions to get the saturation scale for the entire nucleus. Now that x is dependent on Q_s, one must first solve for Q_s and x iteratively until the solutions converge. In order to do so, we take the initial value of x from the CMS parametrization given above.

2.7.3 Nucleon Position - Sampling and Impact Parameter

In addition to the sub-nucleonic color charge fluctuations that will be discussed shortly, IP-Glasma contains another crucial source of fluctuations that are geometric in nature. While this is by no means unique to the IP-Glasma model, the stochastic sampling of nucleon positions, and impact parameter b, introduce fluctuations that are crucial to determining the proper distribution of energy density as characterized by the ϵ_n's. These energy anisotropies are converted by hydrodynamic simulations into the flow harmonics, v_n's, crucial observables in the study of Heavy Ion Collisions. These quantities will be discussed more thoroughly in the results section of this thesis.

In IP-Glasma, the position of nucleons are sampled according to a Woods-Saxon distribution [1], [2] ,

$$\rho(r) = \rho_0\frac{1+\omega(r/R)^2}{1+\exp(\frac{r-R}{a})} \tag{2.135}$$

where ρ_0 is the nucleon density, ω represents deviations from the perfect Woods-Saxon shape, R is the radius of the nucleus, and a is the nuclear skin depth. In the simulations presented in this thesis, ω is taken to be zero, and ρ_0 is unity. For ^{208}Pb, the only nucleus relevant to this thesis, $R = 6.62$ fm and $a = 0.546$ fm.

Alternatively, one can use pre-determined nucleon configurations generated in [33] that include nucleon-nucleon correlations. This has been implemented numerically and is most important for ultra-central collisions where the geometry of the colliding nuclei is nearly circular and dominated by the distribution of nucleons within an

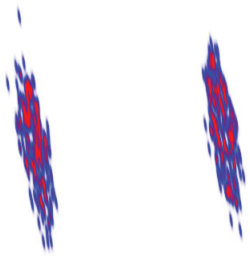

Figure 2.7: Two sheets of color glass prior to the collision. The color represents the strength of the saturation scale, and thus the color charge density, where red corresponds to a higher value, and blue a lower value.

individual nucleus.

Once the nucleons are sampled according to the 3-dimensional Woods-Saxon distribution described above, each nucleon is projected onto the transverse plane. At this point, there are two 2-dimensional nuclei, each with a distribution of nucleons. This is prior to the collision and thus these represent the two sheets of colored glass discussed previously and depicted in figure (2.7).

At this point, the impact parameter b, defined as the separation of the centers of the incoming nuclei in the direction perpendicular to the beam axis, is sampled from the distribution

$$P(b)db = \frac{bdb}{b_{\text{max}}^2/2} \tag{2.136}$$

for each event, where $b_{\text{max}} = 20$ fm for this thesis. The two nuclei are then each shifted by $b/2$ in opposite directions, giving a total separation of b.

2.7.4 Distribution of Color Charge

Once the positions of the nucleons are determined, the square of the saturation scale for each nucleus can be determined by summing the contribution from each nucleon at each point in the transverse plane,

$$Q^2_{s,nucleus}(\boldsymbol{x}_\perp) = \sum_{i=1} Q^2_{s,p,i}(\boldsymbol{x}_\perp) \tag{2.137}$$

Since $Q^2_{s,p} = \frac{2}{r_s^2}$, the total saturation scale is highly dependent on the distribution of nucleons in the transverse plane. From here, we can use (2.132) to determine the average squared surface color charge density for each nucleus.

The MV model considers colliding nuclei in the infinite momentum limit, where the nuclei are thin, infinitely large, two dimensional slabs of color charge. For the nucleus moving in the positive z direction the color charge is taken to have a statistical distribution of the form [15]

$$W[\rho] = \exp\left\{-\int d^2\boldsymbol{x}_\perp \frac{\rho_a(x^-, \boldsymbol{x}_\perp)\rho_a(x^-, \boldsymbol{x}_\perp)}{2\mu^2(x^-, \boldsymbol{x}_\perp)}\right\} \tag{2.138}$$

where $\mu^2(x^-, \boldsymbol{x}_\perp)$ characterizes the local color charge density in the transverse plane. Notice that, by neglecting correlations between partons with finite separation in the tranverse plane, the expression above models color confinement.

The color charge squared per unit area is sampled from the Gaussian weight function given in (2.138) via

$$\langle \rho^a(x^-, \boldsymbol{x}_\perp)\rho^b(x^+, \boldsymbol{y}_\perp)\rangle = g^2\delta^{ab}\delta(\boldsymbol{x}_\perp - \boldsymbol{y}_\perp)\mu^2 \tag{2.139}$$

Discretizing this expression for the lattice,

$$\langle \rho^a_k(x^-, \boldsymbol{x}_\perp)\rho^b_l(x^+, \boldsymbol{y}_\perp)\rangle = \delta^{ab}\delta^{kl}\delta(\boldsymbol{x}_\perp - \boldsymbol{y}_\perp)\frac{g^2\mu^2}{N_y} \tag{2.140}$$

where k and l are indices that label the discretized longitudinal coordinate that run from 1 to N_y. For the purposes of this thesis, $N_y = 10$ [22]. Of course, a and b are SU(N) color indices that run from 1 to $N_c^2 - 1$, and $x_\perp$ and $y_\perp$ are the positions of charges from the two nuclei in the transverse plane. Despite the fact that IP-Glasma is a boost invariant 2+1D model, a finite width in the longitudinal direction, one rapidity unit in this case, is necessary in order to avoid singularities arising from infinite spatial resolution. Taking N_y slices in the η direction corresponds to averaging over N_y color charge configurations. Numerically, the saturation scale is understood

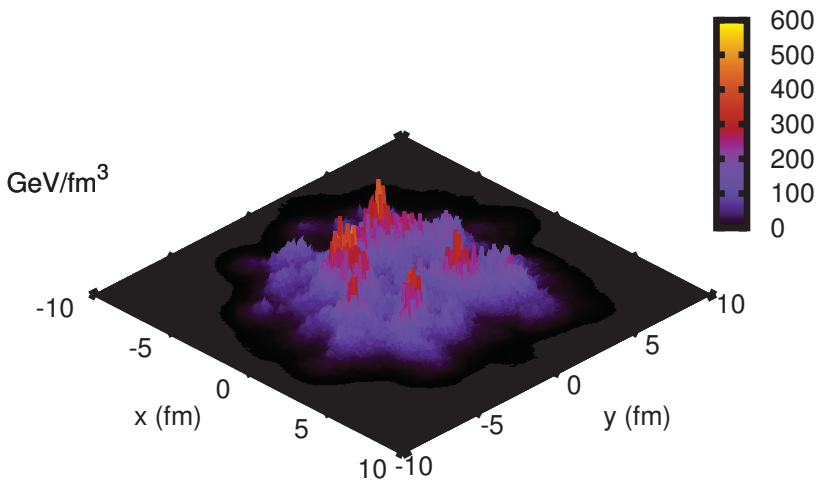

Figure 2.8: Contour plot of the energy density in the transverse plane for one event in the 0-5% centrality bin at 2.76 TeV and $\tau = 0.4$ fm/c. Quantum color charge fluctuations give the IP-Glasma model its "spikey" structure.

to depend on the value of N_y, but converges at some value of N_y, above which the dependence disappears [22]. This has been checked numerically and convergence occurs above $N_y = 50$.

Since the color charge squared is related to the saturation scale simply by a constant of proportionality, equation (2.140) can easily be cast in terms of the saturation scale as,

$$\langle \rho_k^a(x^-, \boldsymbol{x}_\perp)\rho_l^b(x^+, \boldsymbol{y}_\perp)\rangle = \delta^{ab}\delta^{kl}\delta(\boldsymbol{x}_\perp - \boldsymbol{y}_\perp)\frac{Q_s^2}{CN_y} \tag{2.141}$$

This is the variance of the color charge distribution. Of course, the expectation value of the color charge should vanish, $\langle \rho(\boldsymbol{x}_\perp)\rangle = 0$. However, there should be fluctuations on time scales much longer than the collision time, and given by equation (2.141). These fluctuations are sub-nucleonic quantum fluctuations on length scales on the order of the inverse saturation scale and lead to lumps of color charge on each incoming sheet of color glass [34]. In turn, these lumps lead to the "spikey" initial state, as opposed to smooth initial states generated in the Glauber model for example,

that has become the trademark of IP-Glasma and can be seen in figure (2.8).

Such quantum fluctuations lead to fluctuations in the event by event energy distribution per unit rapidity that follow a negative binomial distribution (NBD), as predicted by the glasma flux tube framework, and experimentally verified by fits to p+p multiplicity distributions at RHIC and LHC energies [2]. Such agreement with non-perturbative analytic results as well as experimental data lends credence to this model of sub-nucleonic quantum color fluctuations.

3

Energy-Momentum Tensor and Matching to Hydrodynamics

3.1 Introduction

After evolving the Yang-Mills equations to $\tau_{\rm switch}$, which is taken to be 0.4 fm/c for this thesis, the system should be close enough to thermal equilibrium for hydrodynamics to be applicable. In order to initialize hydrodynamics evolutions, one needs the stress energy tensor, $T^{\mu\nu}$. This section will deal with the calculation of this quantity from the fields that we have evolved via the YM equations and the procedure by which this is matched to hydrodynamics.

3.2 Energy-Momentum Tensor

First, we will derive the form of the energy-tensor for the CGC Lagrangian. From Noether's Theorem, the conserved current associated with translational invariance is the stress energy tensor given by,

$$T^{\mu\nu} = \frac{\delta L}{\delta(\partial_\mu A^a_\rho)}\partial^\nu A^a_\rho - L\delta^{\mu\nu} \tag{3.1}$$

Recalling that, in the absence of sources, $L_{CGC} = -\frac{1}{4}F^{a\mu\nu}F^a_{\mu\nu}$, it is easy to show,

$$\frac{\delta L}{\delta(\partial_\mu A^a_\rho)} = -F^{a\mu\rho} \tag{3.2}$$

and thus

$$T^{\mu\nu} = -F^{a\mu\rho}\partial^\nu A^a_\rho - \frac{1}{4}g^{\mu\nu}(-F^{a\alpha\beta}F^a_{\alpha\beta}) \tag{3.3}$$

$$T^{\mu\nu} = -F^{\mu\rho}\partial^{\nu}A_{\rho} + \frac{1}{4}g^{\mu\nu}F^{\alpha\beta}F_{\alpha\beta} \tag{3.4}$$

This energy momentum tensor is neither symmetric, nor gauge invariant, due to the first term. We can use an "improved" momentum tensor by adding a total derivative, $\partial_{\rho}K^{\rho\mu\nu}$ [35]. $K^{\rho\mu\nu}$ is anti-symmetric in its first two indices and takes the form $K^{\rho\mu\nu} = F^{a\mu\rho}A^{a\nu}$. This addition leaves the global energy-momentum 4-vector unchanged

$$p^{\nu} = \int d^3x\tilde{T}^{0\nu} = \int d^3xT^{0\nu} \tag{3.5}$$

since a total derivative will become a boundary term that vanishes at infinity.

$$\begin{aligned}
\tilde{T}^{\mu\nu} &= -F^{a\mu\rho}\partial^{\nu}A^{a}_{\rho} + \frac{1}{4}g^{\mu\nu}F^{a\alpha\beta}F^{a}_{\alpha\beta} + \partial_{\rho}(F^{a\mu\rho}A^{a\nu}) \\
\tilde{T}^{\mu\nu} &= -F^{a\mu\rho}\partial^{\nu}A^{a}_{\rho} + \frac{1}{4}g^{\mu\nu}F^{a\alpha\beta}F^{a}_{\alpha\beta} + (\partial_{\rho}F^{a\mu\rho})A^{a\nu} + F^{a\mu\rho}\partial_{\rho}A^{a\nu}
\end{aligned} \tag{3.6}$$

We can re-write the second to last term using the fact that the partial derivative can be written in terms of the covariant derivative as $\partial_{\rho} = D_{\rho} + igA^{b}_{\rho}$,

$$\begin{aligned}
\tilde{T}^{\mu\nu} &= -F^{a\mu\rho}\partial^{\nu}A^{a}_{\rho} + \frac{1}{4}g^{\mu\nu}F^{a\alpha\beta}F^{a}_{\alpha\beta} - ((D_{\rho} + igA^{b}_{\rho})F^{a\rho\mu})A^{a\nu} + F^{a\mu\rho}\partial_{\rho}A^{a\nu} \\
\tilde{T}^{\mu\nu} &= -F^{a\mu\rho}\partial^{\nu}A^{a}_{\rho} + \frac{1}{4}g^{\mu\nu}F^{a\alpha\beta}F^{a}_{\alpha\beta} - (D_{\rho}F^{a\rho\mu} + igF^{\rho\mu}A^{b}_{\rho} + ig[A^{b}_{\rho}, F^{a\rho\mu}])A^{a\nu} + F^{a\mu\rho}\partial_{\rho}A^{a\nu} \\
\tilde{T}^{\mu\nu} &= -F^{a\mu\rho}\partial^{\nu}A^{a}_{\rho} + \frac{1}{4}g^{\mu\nu}F^{a\alpha\beta}F^{a}_{\alpha\beta} - ([D_{\rho}, F^{a\rho\mu}] + ig[A^{b}_{\rho}, F^{a\rho\mu}])A^{a\nu} + F^{a\mu\rho}\partial_{\rho}A^{a\nu}
\end{aligned} \tag{3.7}$$

From the equations of motions in the absence of sources, the term $[D_{\rho}, F^{a\mu\rho}] = 0$, leaving

$$\tilde{T}^{\mu\nu} = -F^{a\mu\rho}\partial^{\nu}A^{a}_{\rho} + \frac{1}{4}g^{\mu\nu}F^{a\alpha\beta}F^{a}_{\alpha\beta} - ig[A^{b}_{\rho}, F^{a\rho\mu}]A^{a\nu} + F^{a\mu\rho}\partial_{\rho}A^{a\nu} \tag{3.8}$$

Finally, combining the first term with the last two terms by doing a little SU(3) group algebra gives

$$\tilde{T}^{\mu\nu} = -F^{a\mu\rho}F^{a\nu}_{\rho} + \frac{1}{4}g^{\mu\nu}F^{a\alpha\beta}F_{a\alpha\beta} \tag{3.9}$$

This expression is now symmetric and gauge invariant.

$$\tilde{T}^{\mu\nu} = -g^{\nu\delta}g^{\rho\epsilon}g^{\mu\theta}F_{\theta\epsilon}F_{\delta\rho} + \frac{1}{4}g^{\mu\nu}g^{\alpha\lambda}g^{\beta\omega}F_{\lambda\omega}F_{\alpha\beta} \tag{3.10}$$

3.2.1 Notation

Recalling that in the boost invariant case, we are treating the longitudinal component of the gauge fields as a scalar field, and the electric field as its conjugate momentum,

$$A_\eta = \phi$$

$$E^\eta = \pi = \frac{1}{\tau}\partial_\tau A_\eta \tag{3.11}$$

Choosing the gauge $A^\tau = 0$, and making the following definitions [24] ,

$$F^{i\eta} = D^i A^\eta = g^{ii}g^{\eta\eta}D_i A_\eta = \frac{1}{\tau^2}D_i\phi \quad (i = x, y)$$

$$E_i = -\tau\partial_\tau A_i \tag{3.12}$$

In this notation, the field strength tensor takes the form

$$F^{\mu\nu} = \begin{pmatrix} 0 & -\frac{E^x}{\tau} & -\frac{E^y}{\tau} & -\frac{\pi}{\tau} \\ \frac{E^x}{\tau} & 0 & F^{xy} & \frac{D_x\phi}{\tau^2} \\ \frac{E^y}{\tau} & F^{yx} & 0 & \frac{D_y\phi}{\tau^2} \\ \frac{\pi}{\tau} & -\frac{D_x\phi}{\tau^2} & -\frac{D_y\phi}{\tau^2} & 0 \end{pmatrix} \tag{3.13}$$

3.3 Diagonal Components of $T^{\mu\nu}$

In this section the diagonal components of the energy momentum tensor will be derived. Most importantly, $T^{\tau\tau}$, the energy density of the system will be shown to resemble very closely the energy density of Maxwell's electromagnetic fields. Using expression (3.10), and suppressing color indices throughout this calculation, the first

term, $T^{\tau\tau}$, becomes

$$T^{\tau\tau} = -F^{\tau\rho}F^{\tau}_{\rho} + \frac{1}{4}F^{\alpha\beta}F_{\alpha\beta} \tag{3.14}$$

Expanding the sum over indices and writing the field strength components out explicitly gives

$$\begin{aligned}
T^{\tau\tau} &= -[F^{\tau x}F^{\tau}_{x} + F^{\tau y}F^{\tau}_{y} + F^{\tau\eta}F^{\tau}_{\eta}] + \frac{1}{2}[F^{\tau x}F_{\tau x} + F^{\tau y}F_{\tau y} + F^{\tau\eta}F_{\tau\eta} + F^{xy}F_{xy} + F^{x\eta}F_{x\eta} + F^{y\eta}F_{y\eta}] \\
T^{\tau\tau} &= \left[\frac{E_x^2}{\tau^2} + \frac{E_y^2}{\tau^2} + E_\eta^2 - \frac{1}{2}\left(\frac{E_x^2}{\tau^2} + \frac{E_y^2}{\tau^2} + E_\eta^2 - (F^{xy})^2 - \frac{1}{\tau^2}(D_x\phi)^2 - \frac{1}{\tau^2}(D_y\phi)^2\right)\right] \\
T^{\tau\tau} &= \frac{1}{2}\left[\frac{E_x^2}{\tau^2} + \frac{E_y^2}{\tau^2} + \pi^2 + (F^{xy})^2 - \frac{1}{\tau^2}(D_x\phi)^2 - \frac{1}{\tau^2}(D_y\phi)^2\right]
\end{aligned} \tag{3.15}$$

In terms of a trace over color indices, where we use,

$$\mathrm{Tr}[t^a t^b] = \frac{1}{2}\delta^{ab} \tag{3.16}$$

our final result is

$$T^{\tau\tau} = \mathrm{Tr}[\frac{E_x^2}{\tau^2} + \frac{E_y^2}{\tau^2} + \pi^2 + (F^{xy})^2 - \frac{1}{\tau^2}(D_x\phi)^2 - \frac{1}{\tau^2}(D_y\phi)^2] \tag{3.17}$$

The first three terms give the energy density in the chromo-electric fields, and the last three in the chromo-magnetic fields. This expression is the analogue of the energy density of electromagnetic fields,

$$T^{\tau\tau}_{EM} = \frac{1}{2}[E^2 + B^2] \tag{3.18}$$

Equation (3.17) will be discretized in a later section and used to illustrate the behavior of the fields throughout the simulation.

Figure (3.1) gives an idea of the energy contribution of the different fields. It is clear that only the longitudinal fields are non-zero at initial time, and the other fields grow as the longitudinal fields decrease until the four components are equal by 0.2 fm/c. The maximum Q_s is about 2 GeV, so the time when the interactions become weak and the system moves towards free streaming is $\tau \sim \frac{1}{Q_s} \approx \frac{\hbar c}{2\mathrm{GeV}} \approx 0.1\mathrm{fm/c}$. It is also worth noting that the expansion of the system causes energy density plotted in figure (3.1) to decrease like $\frac{dE}{\tau dy} \sim \frac{1}{\tau}$ while $\frac{dE}{dy}$ becomes constant [1].

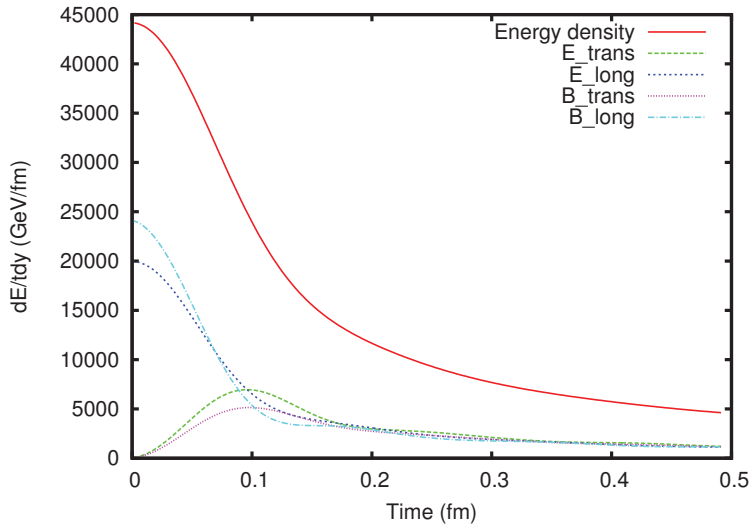

Figure 3.1: Energy Density in the Chromo-Electric and Chromo-Magnetic Fields

From eq. (3.10), one can derive the other diagonal components for the stress energy tensor. In doing so, one finds,

$$T^{xx} = tr[-\frac{E_x^2}{\tau^2} + \frac{E_y^2}{\tau^2} + \pi^2 + (F^{xy})^2 + \frac{1}{\tau^2}(D_x\phi)^2 - \frac{1}{\tau^2}(D_y\phi)^2] \tag{3.19}$$

$$T^{yy} = tr[\frac{E_x^2}{\tau^2} - \frac{E_y^2}{\tau^2} + \pi^2 + (F^{xy})^2 - \frac{1}{\tau^2}(D_x\phi)^2 + \frac{1}{\tau^2}(D_y\phi)^2] \tag{3.20}$$

$$T^{\eta\eta} = \frac{1}{\tau^2}tr[\frac{E_x^2}{\tau^2} + \frac{E_y^2}{\tau^2} - \pi^2 - (F^{xy})^2 + \frac{1}{\tau^2}(D_x\phi)^2 + \frac{1}{\tau^2}(D_y\phi)^2] \tag{3.21}$$

From these expressions it is clear that

$$T^{\mu}_{\mu} = 0 \tag{3.22}$$

as it should be. The remainder of the components of $T^{\mu\nu}$ are straightforward to derive from eq. (3.10). At this point, we will move on to discuss the procedure by which one matches the results of IP-Glasma to hydrodynamic simulations.

3.4 Eigenvalue Problem and Landau Matching

The stress energy tensor from the IP-Glasma framework can be used to initialize hydrodynamic simulations in a process known as Landau matching. It is believed that QGP is a strongly interacting medium that behaves as a nearly perfect fluid while the mean free path of the constituent particles is sufficiently small compared to the macroscopic scale, as characterized by the inverse of the expansion rate. Thus it is natural to describe the complicated dynamics involved in this portion of the evolution by hydrodynamics, a course grained theory that is based primarily on conservation of energy and momentum [36]

$$\partial_\mu T^{\mu\nu} = 0 \tag{3.23}$$

as well as various current conservation laws, such as baryon number, or electric charge,

$$\partial_\mu j^\mu = 0 \tag{3.24}$$

When supplemented by an equation of state, a function that relates the pressure to the energy density, the hydrodynamics equations are closed and one can evolve the system by solving these equations. In addition, one must initialize the stress energy tensor, which, given that hydrodynamics is an expansion of the stress energy tensor of an ideal fluid at rest, is traditionally required to be near local equilibrium. The stress energy tensor made up of the classical gluon fields in the IP-Glasma framework does not satisfy this criterion at common switching times, $\tau \approx 0.2 - 0.4$fm. In fact, if we look at the transverse and longitudinal pressures in ratio to the total energy of the system, defined as

$$P_T = -\frac{T^x_x + T^y_y}{2} = -\frac{g_{xx}T^{xx} + g_{yy}T^{yy}}{2} = \frac{T^{xx} + T^{yy}}{2} \tag{3.25}$$

and

$$P_L = -T^\eta_\eta = -g_{\eta\eta}T^{\eta\eta} = \tau^2 T^{\eta\eta} \tag{3.26}$$

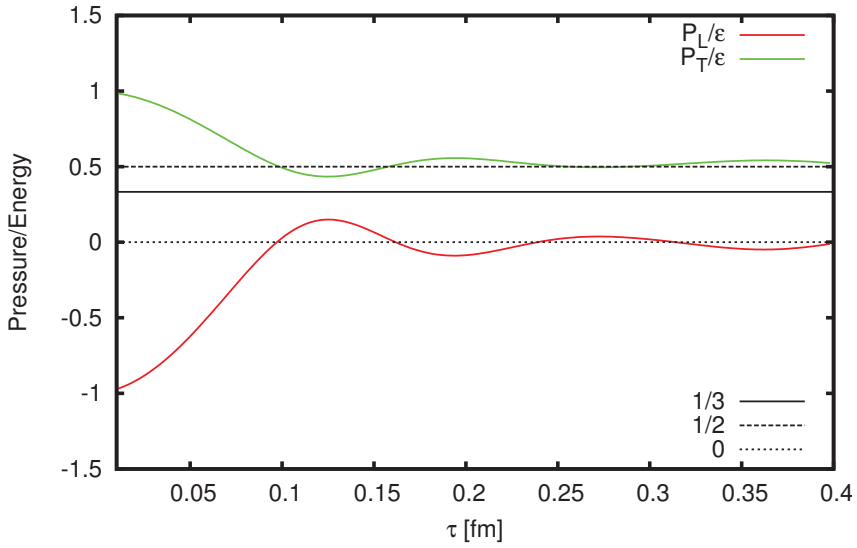

Figure 3.2: The ratio of the transverse pressure and longitudinal pressures to the energy density, given by the red and green curves respectively. It is clear that the system never isotropizes since these values do not approach 1/3.

we can see that, due to the fact that the transverse fields vanish at $\tau = 0^+$,

$$\lim_{\tau \to 0^+} P_T = -\lim_{\tau \to 0^+} P_L = \epsilon \tag{3.27}$$

Additionally, for the classical YM equations [37],

$$\lim_{\tau \to \infty} P_T = \frac{\epsilon}{2} \tag{3.28}$$

and

$$\lim_{\tau \to \infty} P_L = 0 \tag{3.29}$$

For an isotropic system $P_L = P_T = \frac{\epsilon}{3}$. Thus, for the Classical Yang Mills equations, the stress energy tensor never isotropizes. It has, however, been shown that quantum corrections can bring the system to a state in which hydrodynamics is applicable [37] [38].

In order to get an isotropic stress energy tensor in equilibrium for the leading order, i.e. classical, YM equations, one can simply neglect the non-equilibrium components

by solving the eigenvalue problem

$$T^{\mu}_{\nu} u^{\nu} = \epsilon u^{\nu} \tag{3.30}$$

using the IP-Glasma $T^{\mu\nu}$. The solution is taken to be the timelike eigenvector and its corresponding eigenvalue. The flow velocity's Minkowski norm is normalized to unity,

$$u^{\mu} u_{\mu} = g_{\mu\nu} u^{\mu} u^{\nu} = (u^{\tau})^2 - (u^{x})^2 - (u^{y})^2 - \tau^2 (u^{\eta})^2 = 1 \tag{3.31}$$

where the metric is $g_{\mu\nu} = diag(1, -1, -1 - \tau^2)$. Here, ϵ is taken to be the initial value of the local energy density in the hydrodynamic simulation, and u^{μ} is used to reconstruct the ideal hydrodynamics energy tensor [39]

For an ideal fluid at rest, the stress energy tensor decomposes as

$$T^{\mu\nu} = (\epsilon + P) u^{\mu} u^{\nu} - P g^{\mu\nu} = \mathrm{diag}(\epsilon, P, P, P) \tag{3.32}$$

Thus, one can reconstruct an ideal stress energy tensor from the initial flow u^{μ} and energy density ϵ taken from the eigenvalue problem. This process is known as Landau Matching.

In the absence of a process that equilibrates the system, Landau matching must be used to connect IP-Glasma and subsequent hydrodynamic simulations. It is clear that this process discards information from the IP-Glasma framework and more work needs to be done understand how the system reaches equilibrium. At the moment, however, when trying to match $T^{\mu\nu}_{IPG}$ directly to hydro, the inapplicability of hydrodynamics manifests itself numerically, as the non-ideal components can become order one, meaning they are no longer corrections to the equilibrium stress-energy tensor, and generate severe instabilities. The discarded components in Landau matching correspond to the shear stress tensor $\pi^{\mu\nu}$ and bulk viscous pressure Π. This is the case even in the viscous hydrodynamic simulations that will be presented in this thesis, meaning that $T^{\mu\nu}$ is initialized to the ideal case, and then evolved using the full equations that include shear and bulk viscoscities, namely,

$$T^{\mu\nu} = \epsilon u^{\mu} u^{\nu} - \Delta^{\mu\nu} (P + \Pi) + \pi^{\mu\nu} \tag{3.33}$$

with flow velocity u^μ, pressure P, energy density ϵ, shear stress tensor $\pi^{\mu\nu}$, and bulk viscous pressure Π. Here, $\Delta^{\mu\nu} = g^{\mu\nu} - u^\mu u^\nu$ is the local 3-metric that is orthogonal to the flow vector, and the shear stress tensor and bulk pressure satisfy

$$\tau_\Pi \dot{\Pi} + \Pi = -\zeta\theta - \delta_{\Pi\Pi}\Pi\theta + \lambda_{\Pi\pi}\pi^{\mu\nu}\sigma_{\mu\nu} \tag{3.34}$$

and

$$\tau_\pi \dot{\pi}^{\langle\mu\nu\rangle} + \pi^{\mu\nu} = 2\eta\sigma^{\mu\nu} - \delta_{\pi\pi}\pi^{\mu\nu}\theta + \phi_7\pi_\alpha^{\langle\mu}\pi^{\nu\rangle\alpha} - \tau_{\pi\pi}\pi_\alpha^{\langle\mu}\sigma^{\nu\rangle\alpha} + \lambda_{\pi\Pi}\Pi\sigma^{\mu\nu} \tag{3.35}$$

respectively. These relaxation type equation are derived from kinetic theory and solved numerically in MUSIC. The relaxation times for the bulk pressure and shear stress tensor are denoted τ_Π and τ_π, respectively. Also, $\theta = \partial_\mu u^\mu$ is the scalar expansion rate, $\sigma_{\mu\nu} = \frac{1}{2}\left(\nabla_\mu u_\nu + \nabla_\nu u_\mu - \frac{2}{3}\theta\Delta_{\mu\nu}\right)$, η is the shear viscosity and is assumed to be proportional to the entropy density $\eta \propto s$, while ζ is the bulk-viscosity whose temperature dependence is given in equation (3.40). For the second order transport coefficients listed in equation (3.34), the expressions are [40]

$$\begin{aligned} \frac{\delta_{\Pi\Pi}}{\tau_\Pi} &= \frac{2}{3} + O(z^2 \ln z), \\ \frac{\lambda_{\Pi\pi}}{\tau_\Pi} &= \frac{8}{5}\left(\frac{1}{3} - c_s^2\right) + O(z^4) \end{aligned} \tag{3.36}$$

and for (3.35), they are,

$$\begin{aligned} \frac{\lambda_{\pi\Pi}}{\tau_\pi} &= \frac{6}{5} + O(z^2), \\ \delta_{\pi\pi} &= \frac{4}{3}\tau_\pi, \\ \tau_{\pi\pi} &= \frac{10}{7}\tau_\pi, \\ \phi_7 &= \frac{9}{70P_0} \end{aligned} \tag{3.37}$$

where $z = m/T$ is the ratio of the mass of the particle to the temperature, c_s is the speed of sound, and P_0 is the thermodynamic pressure.

It is worth noting that it has recently been argued that the requirement that the system be near equilibrium may be an overly stringent demand since systems out of equilibrium have been shown to be adequately described by hydrodynamics

[36, 41, 42]. The mechanism by which this occurs is not fully understand and thus we will consider this notion to be an intriguing but unsettled question that faces the field in the years to come.

3.5 Initial Flow

A key feature of IP-Glasma is the non-zero flow that it provides as initial conditions for hydrodynamic evolutions, in contrast to many other initial conditions. This flow is necessary to get the correct values for observables such as the v_n flow harmonics and the mean transverse momentum $\langle p_T \rangle$.

Figure (3.3) shows the transverse flow field of a Pb-Pb collision at 2.76 TeV with $b = 0$ fm. The plots are intuitively pleasing, as the flow tends to point from high energy density to low energy density, as one would expect. The event in figure (3.4) with $b = 8$ fm has the characteristic almond shaped overlap region, and already has a non-zero v_2, even before hydrodynamic evolution. Note, that the impact parameter axis is the line $y = x$ in figure (3.4).

Due to the historical fact that boost invariant simulations have preceded full 3+1D simulations both in hydrodynamics and initial conditions, longitudinal flow has traditionally been initialized to zero. This is the case for the phenomenological study presented in this thesis. However, the component of the flow vector in the η-direction is not small. To illustrate this, we can compare the solution of the full 4×4 eigenvalue problem to the case where the η components are excluded and the eigenvalue problem effectively becomes 3 dimensional. In doing so for 100 Pb-Pb events at 2.76 TeV in the 0-5% centrality range, we find that the η component of the flow is nearly 50% of the transverse flow, where we use an RMS definition for the average of each flow component

$$\langle u^\mu \rangle = \langle \sqrt{\frac{\int \epsilon u^\mu u^\mu dx_\perp}{\int \epsilon dx_\perp}} \rangle \tag{3.38}$$

and

$$u^\perp = \sqrt{(u^x)^2 + (u^y)^2} \tag{3.39}$$

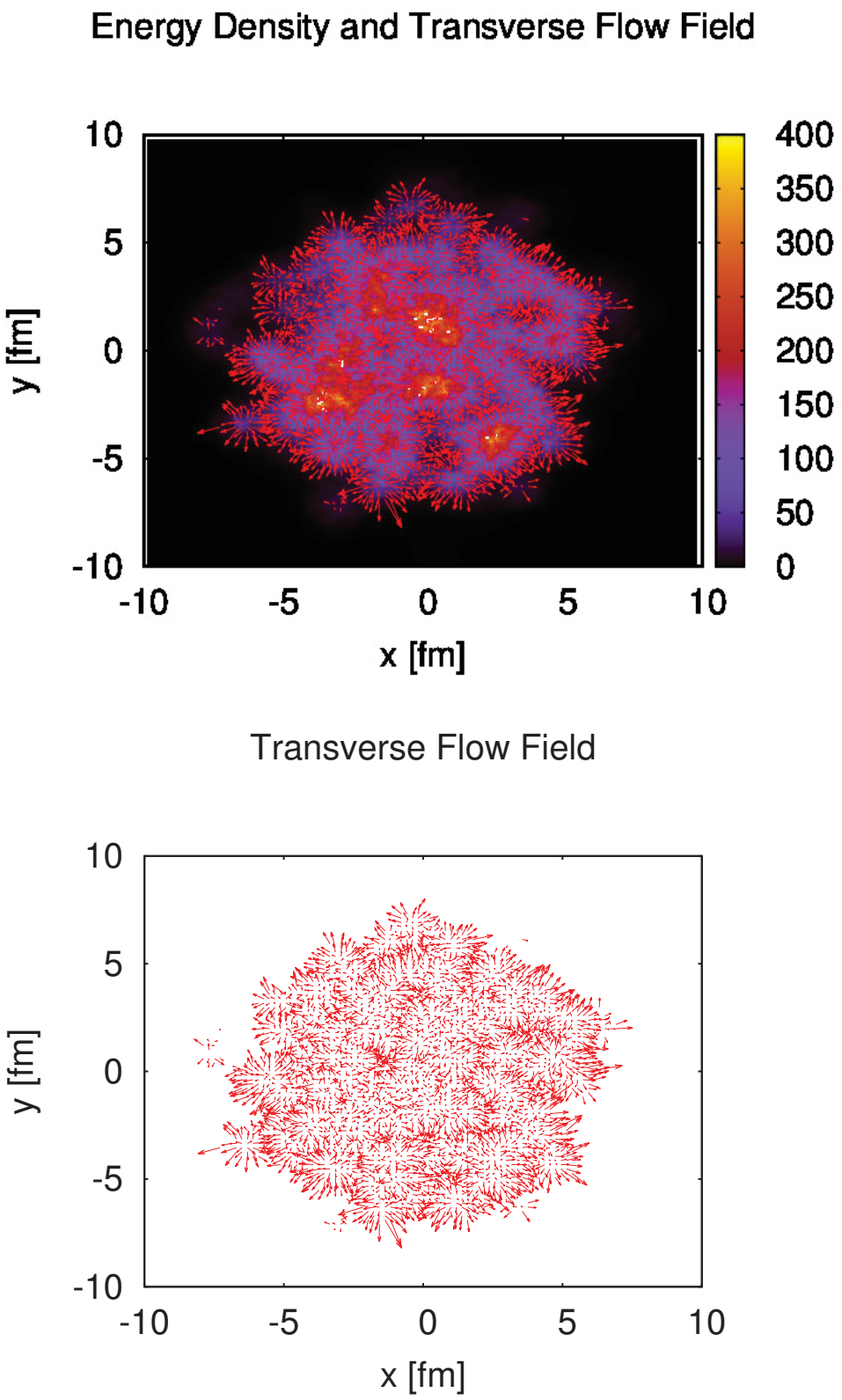

Figure 3.3: Above: Flow field u^μ superimposed on the local energy density ϵ, given in GeV/fm^3, for a Pb-Pb collision at $b = 0$ fm. Below: The same flow field u^μ as given above without the background energy density

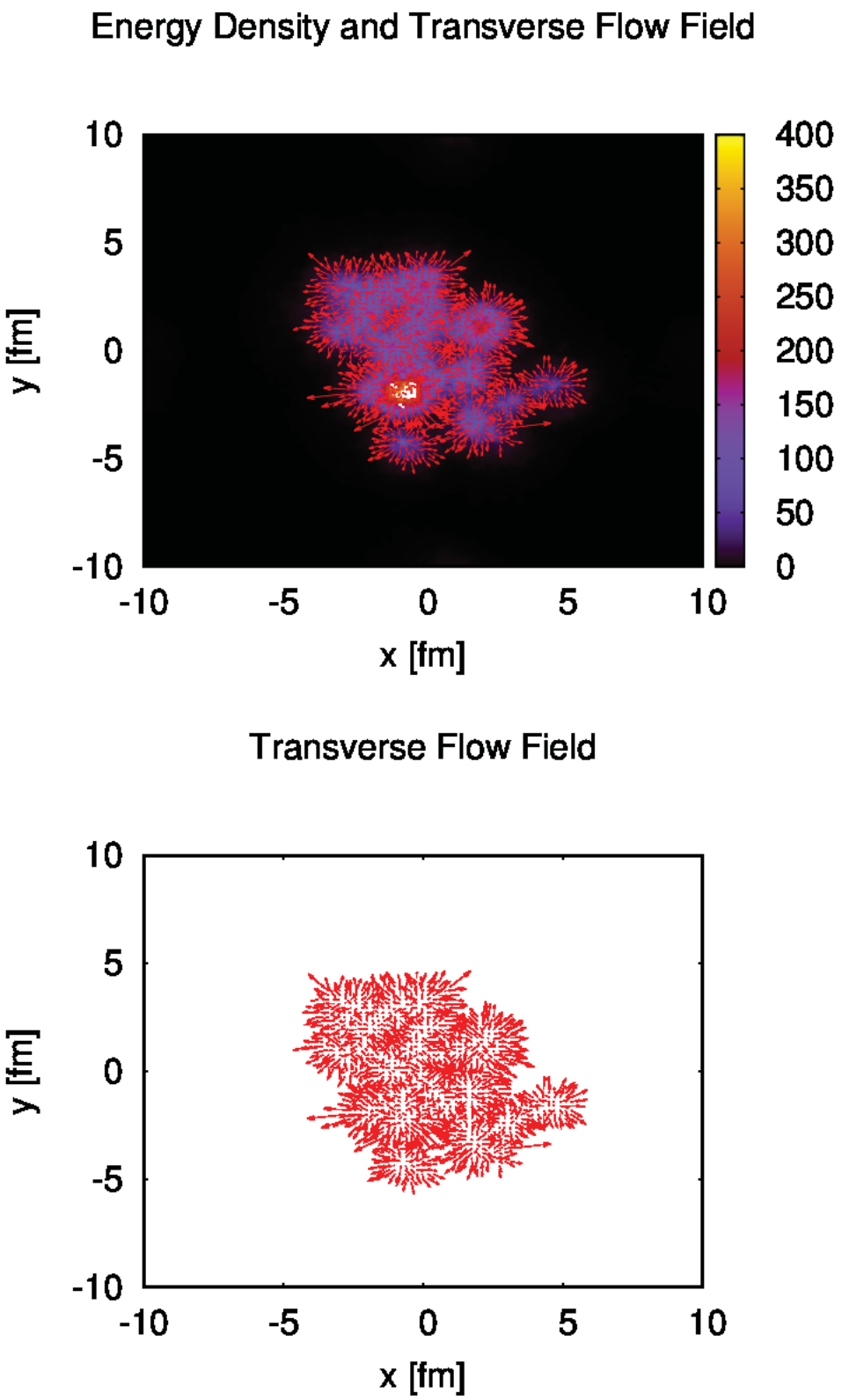

Figure 3.4: Top: Flow field u^μ superimposed on the local energy density ϵ, given in GeV/fm^3, for a Pb-Pb collision at $b = 8$ fm. Note that the impact parameter axis is taken to be the line $y = x$. One can see the famous almond shaped overlap region. Below: The same vector field without the background energy density

Table 3.1: Table of average flow $\langle u^\tau \rangle$, $\langle u^\perp \rangle$, and $\langle \tau u^\eta \rangle$

	Using 4x4 $T^{\mu\nu}$	Using 3x3 $T^{\mu\nu}$
$\langle u^\tau \rangle$	1.027776	1.023935
$\langle \tau u^\eta \rangle$	0.1005303	N/A
$\langle u^\perp \rangle$	0.2115732	0.2200597
$\frac{\langle \tau u^\eta \rangle}{\langle u^\perp \rangle}$	0.4751561	N/A

In order to compare quantities with the same units, we multiply u^η by τ, such that τu^η, $u^\perp$, and u^τ are all dimensionless in natural units. Note that the inclusion of the u^η component slightly decreases the transverse flow. The phenomenological effects of u^η, both on the transverse and longitudinal dynamics, should be studied to determine its importance. As the field moves towards full 3+1D simulations, the η component of the flow will almost certainly become a key new feature whose effects will need to be included.

3.6 Viscous Hydrodynamics Parametrization

As mentioned, equations (3.23) and (3.24) govern the hydrodynamical evolution and equation (3.33) gives the hydrodynamical stress energy tensor. The parameters that are used for the viscous hydrodynamic evolution will be outlined in this section.

One of the central goals of the HIC is to extract the transport coefficients of the QGP medium. Fortunately, the community has made significant progress in this direction, and the parameters used in this thesis derive heavily from the work of others and will be simply quoted here.

The shear viscosity used for the simulations in this thesis was taken to be $\eta/s = 0.095$ for both LHC energies. It has been postulated that a temperature dependent shear viscosity may be necessary to accurately describe physics at a wide range of collision energies. However, for the two energies studied here, which differ by less than a factor of two, no such parametrization was necessary to accurately describe the flow data, and thus the temperature dependence is either rather slight or the two

collision energies produce very similar temperatures.

The bulk viscosity on the other hand has been taken from [43] [44] to be temperature dependent and highly peaked around the QCD phase transition temperature. The same temperature dependence as given in [43] was used but the peak was reduced by 10%. The expression is given by,

$$\zeta/s(T) = 0.9\times\begin{cases} 0.9e^{\left(\frac{T}{T_\mathrm{p}}-1\right)/0.0025} + 0.22e^{\left(\frac{T}{T_\mathrm{p}}-1\right)/0.022} + 0.03 & \text{if} \quad T < 0.95T_\mathrm{p} \\ -13.77\left(\frac{T}{T_\mathrm{p}}\right)^2 + 27.55\left(\frac{T}{T_\mathrm{p}}\right) - 13.45 & \text{if} \quad 0.95T_\mathrm{p} < T < 1.05T_\mathrm{p} \\ 0.025e^{-\left(\frac{T}{T_\mathrm{p}}-1\right)/0.025} + 0.25e^{\left(\frac{T}{T_\mathrm{p}}-1\right)/0.13} + 0.001 & \text{if} \quad T > 1.05T_\mathrm{p} \end{cases}, \tag{3.40}$$

where $T_\mathrm{p} = 180$ MeV for the peak of ζ/s. The bulk viscosity above T_P in this parametrization is based on lattice calculations [45] and below T_P, it is based on calculations from a hadron resonance gas model [46].

3.7 Freezeout - Cooper-Frye Formalism

As the system expands hydrodynamically, it will cool and re-hadronize, i.e. turn back into hadrons. This occurs when hydrodynamics is no longer applicable, namely when the mean free path becomes on the order of the macroscopic length scale associated with the system. We consider this to happen at a given temperature and thus take an isothermal freezeout hypersurface, the exact temperature of which is often treated as a parameter in numerical simulations, as it is here, and is chosen to be $T_{freezeout} =$ 145MeV [43].

The Cooper-Frye formalism, first given in [47], provides a way of converting the hydrodynamic energy-momentum tensor into particles while conserving energy and momentum. It does so by integrating a statistical distribution function, derived through kinetic theory, to compute quantities of interest. The distribution function with shear and bulk viscosities is

$$f(x,\mathbf{p}) = f_0(x,\mathbf{p}) + \delta f_{shear}(x,\mathbf{p}) + \delta f_{bulk}(x,\mathbf{p}) \tag{3.41}$$

where the equilibrium term is

$$f_0(x,\mathbf{p}) = \frac{1}{\exp(\frac{p\cdot u}{T}) \mp 1} \tag{3.42}$$

depending on spin-statistics, and δf_{shear} and δf_{bulk} are viscous corrections to the distribution function given by [48],

$$f_{shear}(x,\mathbf{p}) = f_0(1+af_0)\frac{\pi_{\mu\nu}p^\mu p^\nu}{2(\epsilon_0+P_0)T^2} \tag{3.43}$$

and

$$f_{bulk}(x,\mathbf{p}) = -f_0(1+af_0)\frac{C_{bulk}}{T}\left[\frac{m^2}{3(p\cdot u)} - (\frac{1}{3}-c_s^2)(p\cdot u)\right]\Pi \tag{3.44}$$

Here $a = 0, 1, -1$ for Boltzmann, Bose-Einstein, and Fermi-Dirac statistics, respectively, c_s is the speed of sound, and C_{bulk} is defined through

$$\frac{T}{C_{bulk}} = \frac{1}{3}\sum_n d_n m_n^2 \int \frac{d^3\mathbf{k}}{(2\pi)^3 E_\mathbf{k}} f_{n,0}(1\pm f_{n,0})\left[\frac{m_n^2}{3E_\mathbf{k}} - (\frac{1}{3}-c_s^2)E_\mathbf{k}\right] \tag{3.45}$$

where the sum is over particle species and d_n are degeneracy factors. One can convert into particles via

$$\frac{dN}{d^3\mathbf{p}} = \frac{d}{(2\pi)^3}\int_\Sigma f(x,\mathbf{p})\frac{p^\mu d^3\Sigma_\mu}{E_\mathbf{p}} \tag{3.46}$$

where Σ_μ is the normal vector to the hypersurface of constant temperature. Assuming a single species of particle in the hadronic gas from here on out for simplicity, the number of particles is given by

$$N = \int \frac{dN}{d^3\mathbf{p}} d^3\mathbf{p} = \int_\Sigma n^\mu(x) d^3\Sigma_\mu \tag{3.47}$$

where n^μ is the number current given by

$$n^\mu(x) = \frac{d}{(2\pi)^3}\int \frac{p^\mu}{E_\mathbf{p}} f(x,\mathbf{p}) d^3\mathbf{p} \tag{3.48}$$

The number of particles from each individual cell is sampled from a Poisson distribution

$$P_{1-cell} = \frac{1}{N!}\langle N\rangle^N e^{-\langle N\rangle} \tag{3.49}$$

whose average is given by $\langle N\rangle_{1-cell}$ The total momentum can be determined as well

$$P^\mu = \int p^\mu \frac{dN}{d^3\mathbf{p}} = \int_\Sigma T^{\mu\nu}(x) d^3\Sigma_\nu \tag{3.50}$$

where the stress energy tensor for the hadron gas comes from kinetic theory,

$$T^{\mu\nu}(x) = \frac{d}{(2\pi)^3}\int \frac{p^\mu p^\nu}{E_\mathbf{p}} f(x,\mathbf{p}) d^3\mathbf{p} \tag{3.51}$$

Then momentum is also sampled via

$$\frac{dN}{d^3\mathbf{p}}|_{1-cell} = \frac{d}{(2\pi)^3}[f_0(x,\mathbf{p}) + \delta f_{shear}(x,\mathbf{p}) + \delta f_{bulk}(x,\mathbf{p})]\frac{p^\mu \Delta\Sigma_\mu}{E_\mathbf{p}} \tag{3.52}$$

if $f(x,\mathbf{p}) \geq 0$ and $p^\mu\Sigma_\mu > 0$ are satisfied. These criteria correspond to having a positive distribution function and a four-velocity u^μ pointing in the direction of decreasing temperature, respectively, at the cell in question. Otherwise the momentum is taken to be zero.

Once the system has fully hadronized, there are still re-scatterings and decays that can alter the state of the system, before the particles reach the detectors. This physics is taken care of in the Ultrarelativistic Quantum Molecular Dynamics (UrQMD) framework [6], the details of which can be found at https://urqmd.org/.

3.8 UrQMD

3.8.1 Hadronic Re-Scattering

The cross sections in UrQMD are functions of the particular species involved, the center of mass energy, and isospin, and are obtained from a variety of methods including experimental fits, algebraic parametrizations, the principle of detailed balance, and the additive quark model. These cross sections are interpreted as areas and the criterion for whether a nucleon-nucleon collision occurs is simply,

$$d_\perp < d_0 = \sqrt{\frac{\sigma_{tot}}{\pi}} \tag{3.53}$$

where $d_\perp$ is the separation of the particles and $\sigma_{tot} = \sigma(\sqrt{s}, \text{species})$ is simply a function of energy and the interacting species involved. This criterion is checked for each particle at every time step. For consistency, $d_\perp$ is taken to be the distance of closest approach in the local rest frame of the two potential collision partner particles,

$$d_\perp = \mathbf{d}^2 - \mathbf{d}_{||}{}^2 = (\mathbf{q_1} - \mathbf{q_2})^2 - \frac{((\mathbf{q_1} - \mathbf{q_2})(\mathbf{p_1'} - \mathbf{p_2'}))^2}{(\mathbf{p_1'} - \mathbf{p_2'})^2} \tag{3.54}$$

where $\mathbf{q_i}$ are the location of the particles and $\mathbf{p_i'}$ are the momenta of the particles in the local rest frame of the colliding particles. This avoids any ambiguity in the criterion for the nucleon-nucleon collisions arising from choice of reference frame.

The time of the collision is frame dependent and is defined in terms of the nucleus-nucleus reference frame to be,

$$\tau_{coll} = -\frac{(\mathbf{r_1} - \mathbf{r_2}) \cdot (\mathbf{p_1}/E_1 - \mathbf{p_2}/E_2)}{(\mathbf{p_1}/E_1 - \mathbf{p_2}/E_2)^2} \tag{3.55}$$

3.8.2 Resonance Decays

There is no reason to assume that all of the particles produced will be stable and thus it is important to allow for the particles to decay before reaching the detector. UrQMD includes resonance decays via a mass-dependent total width that is simply the sum of all partial decay widths,

$$\Gamma_{total}(M) = \sum_{br=i,j}^{N_{br}} \Gamma_{i,j}(M) \tag{3.56}$$

where the partial decay widths into the channel with final particles i and j is,

$$\Gamma_{total}(M) = \Gamma_R^{i,j} \frac{M_R}{M} \left(\frac{\langle p_{i,j}(M)\rangle}{\langle p_{i,j}(M_R)\rangle}\right)^{2l+1} \frac{1.2}{1 + 0.2\left(\frac{\langle p_{i,j}(M)\rangle}{\langle p_{i,j}(M_R)\rangle}\right)^{2l}} \tag{3.57}$$

Here M_R is the pole mass of the resonance, $\Gamma_R^{i,j}$ is the partial decay width into particles i and j at the pole as taken from the Particle Data Book, and l is the angular

momentum of the channel. The lifetime of each resonance is sampled via a Monte-Carlo procedure using the exponential decay law with decay constant $\tau_R = \frac{1}{\Gamma_R}$. Lastly, the final state is determined using the branching ratio.

Further details on cross sections, decay widths, particle species, as well as any other specifics related to the theory and implementation of UrQMD, can be found [6] [49]. The parameters used for this thesis correspond to the default parametrization of UrQMD. At this point, we move on to the numerical implementation of IP-Glasma.

4

Numerical Implementation

4.1 Introduction

4.2 Lattice Units and Spacing

4.2.1 Lattice Units

First, it is important to make note of the the units that will be used on the lattice. The reader may have noticed in the previous discussion that the lattice spacing, a, shows up in many expressions. In order to simplify equations and avoid confusion with units, we will work in "lattice units." This means that all quantities, after having been read into the simulation from the parameter file, are made unitless by the proper operations with the lattice spacing. The lattice spacing has units of length, and thus in natural units one can use the lattice spacing along with appropriate factors of $\hbar$ and c to convert quantities to lattice units, i.e. unitless. This will eliminate all factors of a in the calculation. After the simulation, all quantities are returned to physical units by the reverse procedure.

4.2.2 Lattice Spacing

The energy in the fields at $\tau = 0^+$ is understood to depend on the lattice spacing [50], but should converge towards a single value, regardless of lattice spacing at some later time. Figure (4.1) reassures us that our numerical implementation is sound and provides an indication of what lattice spacing and switching time are safe to use. It is worth noting, however, that the average initial flow is more sensitive to the

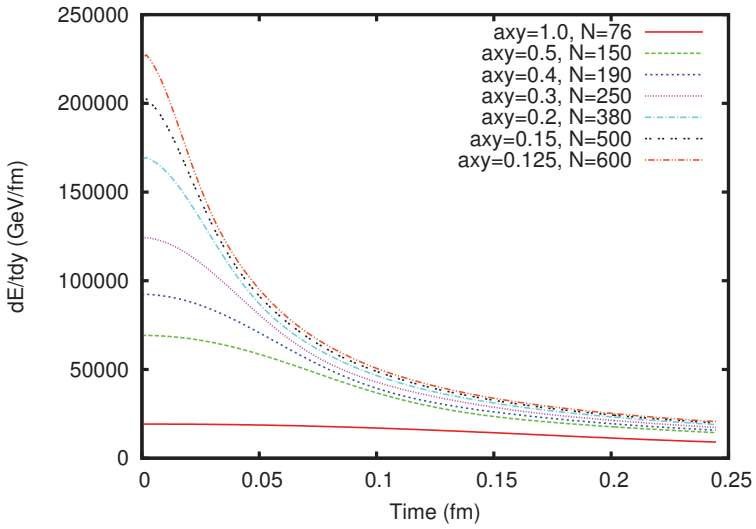

Figure 4.1: Total integrated energy density in the tranverse plane as a function of the lattice spacing, given in GeV^{-1}. For $\tau > 0.1$ we see convergence for $axy \geq 0.5\text{GeV}^{-1}$

lattice spacing than the integrated energy density, and thus requires a finer grid to find convergence. For the phenomenological results given in this thesis, $N = 1000$, $a_{xy} = 0.1$ GeV^{-1}, and the switching time is 0.4 fm/c. Here a_{xy} is the lattice spacing in the transverse plane, and is equivalent to what we have been referring to more generally as a.

As shown in figure (4.1), the energy density starts to converge at $\tau > 0.1$fm/c at relatively large values of $a_{xy} \sim 0.5\text{GeV}^{-1}$. The question, then, is for what value of the lattice spacing can we be confident that we are probing all of the relevant physics? What is the physical argument for using a given lattice spacing?

In order to resolve physics up to the saturation scale, the lattice spacing should be at least as small as the inverse saturation scale $1/Q_s$. Conservatively taking the maximum saturation scale at the LHC to be 4 GeV, the lattice spacing must be $a_{xy} \leq \frac{1}{Q_{s,max}} \approx 1/4$ GeV $= 0.25$ GeV^{-1}. By using a lattice spacing of $a_{xy} = 0.1\text{GeV}^{-1}$ for the results presented in this thesis, we ensure that we are able to safely resolve physics up to and including the saturation scale.

4.3 Numerical Procedure for Solving Initial Fields

The following numerical procedure for solving eq (2.104) was developed by Marius Cautun, Francois Fillion-Gourdeau, and Sangyong Jeon. The general procedure will be outlined here, but further details can be found [51].

First, it worth noting that equation (2.104) is actually $N_c^2 - 1$ equations, one for each SU(3) group generator. It has been solved analytically for the SU(2) case [24], but is a highly non-linear system that must be solved iteratively for the $N_c > 2$ case. One such solution will be presented in the following discussion.

The iterative procedure is initialized by taking the Abelian solution to equation (2.104) as a guess for the more general solution, namely,

$$U_i = U_i^{(A)} U_i^{(B)} \tag{4.1}$$

for a given lattice site (dropping lattice site index). Inserting this guess into eq. (2.104) gives,

$$\mathrm{ReTr}\left[t_a(U^{(1)} + U^{(2)})(1 + U^{(3)\dagger})\right] = f_a \tag{4.2}$$

Recalling that $U^{(3)}$ is an element of SU(3) we can relate the current iteration to the previous iteration via

$$U^{(3)}_{current} = e^{i\alpha x_a t_a} U^{(3)}_{previous} \tag{4.3}$$

in order to preserve unitarity. Here $U^{(3)}_{previous}$ is the previous guess obtained by solving (4.2), and α is a constant parameter of our choosing < 1.0 that helps with convergence by ensuring that f_a is small. If f_a is already small, α is taken to be unity. Expanding the exponential in (4.3) and keeping the first two terms gives

$$U^{(3)}_{current} \approx (1 + i\alpha x_a t_a) U^{(3)}_{previous} \tag{4.4}$$

and requiring that $U^{(3)}_{current}$ solves (2.104) yields

$$\alpha x_b \mathrm{Im\ Tr}\left[t_b t_a (U^{(1)} + U^{(2)}) U^{(3)\dagger}_{previous}\right] = -f_a \tag{4.5}$$

This set of equations can be solved for x_b, which in turns gives us $U^{(3)}_{current}$ via eq. (4.3) where we use the full expression, without approximating the exponential. Plugging $U^{(3)}_{current}$ back into (2.104) gives a new value of f_a which we will denote f^*_a. Using the Taylor expansion for the exponential in eq. (4.3), the first non-zero term gives

$$f^*_a = -\frac{\alpha^2}{2} x_b x_c \mathrm{ReTr}\left[t_b t_c t_a (U^{(1)} + U^{(2)}) U^{(3)\dagger}_{previous}\right] \tag{4.6}$$

Near the continuum limit, meaning $\lim_{N_y \to \infty}$, the Wilson lines become unit matrices. In this limit, eq. (4.5) becomes $x_a = -f_a$, and eq. (4.6) simplifies to

$$f^*_a = -\frac{\alpha^2}{4} f_b f_c d_{abc} \tag{4.7}$$

where d_{abc} are structure constants given by

$$d_{abc} = 2\mathrm{Tr}\left[\{t_a, t_b\} t_c\right] \tag{4.8}$$

in the fundamental representation of SU(3), and $\{t_a, t_b\}$ denotes the anti-commutator of t_a and t_b.

Despite the fact eq. (4.7) was derived in the continuum limit, we expect $f_a \propto f_b f_c$ in the general case, albeit with a more complicated relationship perhaps. Thus, for small initial guesses for f_a we expect $|f^*_a| < f_a$, and by iterating this process f_a should converge towards zero, yielding the solution to (2.104). The parameter α was introduced in equation (4.3) with the assumption that our solution to (4.6) gives us the correct direction to move for f^*_a from f_a but not necessarily the magnitude. Thus α helps this procedure converge faster.

If this procedure does not converge, although for most lattices spacings it does, we call a simulated annealing method (SAM) to improve the initial guess for $U^{(3)}$. This is done only if the process does not converge within a pre-determined number of iterations, taken to be on the order of 10-50. For details on the numerical performance of this method including data on iterations need for convergence, convergence speed, etc., see [51].

4.4 Leap Frog Algorithm

The leap frog algorithm is a symplectic integrator used to numerically integrate differential equations such as those in equations (2.99)-(2.103). It gets its name from the common children's game in which children successively hop over one another. The algorithm follows a similiar procedure by evolving derivatives at times halfway between the time steps of the quantities themselves, and thus the quantity and its derivative successively leap over one another, but are never at the same time. In general, for a quantity x, its first time derivative v, and second derivative a,

$$x(\tau + d\tau) = x(\tau) + v(\tau + d\tau/2)d\tau \tag{4.9}$$

$$v(\tau + d\tau/2) = v(\tau - d\tau/2) + a(\tau)d\tau \tag{4.10}$$

Applying this procedure, the discretized Hamiltonian equations of motion given in eq.'s (2.99)-(2.103), become,

$$\phi(x, \tau + d\tau) = \phi(x, \tau) + \frac{\tau + \frac{d\tau}{2}}{d\tau}\pi(x, \tau + \frac{d\tau}{2}) \tag{4.11}$$

$$U_i(x.\tau + d\tau) = \exp\left(i\frac{g^2 d\tau}{(\tau + \frac{d\tau}{2})}E^i(\tau + \frac{d\tau}{2})\right)U_i(\tau) \tag{4.12}$$

$$\begin{aligned} E^x(x, \tau + d\tau/2) = E^x(x, \tau - d\tau/2) &+ i\frac{(\tau + \frac{d\tau}{2})d\tau}{2g^2}\left(U_{xy} + U_{x-y} - \text{h.c.} - \text{trace}\right) \\ &+ i\frac{d\tau}{(\tau + \frac{d\tau}{2})}[\tilde{\phi}_x, \phi] \end{aligned} \tag{4.13}$$

$$\begin{aligned} E^y(x, \tau + d\tau/2) = E^y(x, \tau - d\tau/2) &+ i\frac{(\tau + \frac{d\tau}{2})d\tau}{2g^2}\left(U_{yx} + U_{y-x} - \text{h.c.} - \text{trace}\right) \\ &+ i\frac{d\tau}{(\tau + \frac{d\tau}{2})}[\tilde{\phi}_y, \phi] \end{aligned} \tag{4.14}$$

$$\pi(x, \tau + d\tau/2) = \pi(x, \tau - d\tau/2) + \frac{d\tau}{(\tau + \frac{d\tau}{2})}\sum_i(\tilde{\phi}_i + \tilde{\phi}_{-i} - 2\phi) \tag{4.15}$$

Note that the last three equations above would involve division by τ, which would cause clear issues for $\tau = 0$. For this reason $\frac{1}{\tau}$ is replaced by $\frac{d\tau}{(\tau+\frac{d\tau}{2})}$ which equals $1/2$ for $\tau = 0$. This introduces some error but prevents these terms from blowing up at initial time. For large τ this expression has the same behavior as $\frac{1}{\tau}$. Furthermore, because, as mentioned, the momenta (derivatives) E^i and π are stored at $\tau - \frac{d\tau}{2}$, while ϕ and U_i are stored at τ, the derivatives will always lag behind the fields by half of a time step. This is the so-called leap frog algorithm. At the end of the simulation, the derivatives are evolved by an additional half time step to bring all quantities to the same value of τ. The leap frog algorithm has error of order $d\tau^2$ at each step.

4.5 Solving for Q_s - Brent's Method

Brent's method [52] is a root finding algorithm that combines several simpler methods, namely the bisection method, the secant method, and inverse quadratic interpolation, for a quick yet reliable solution. As a reminder, the problem that we need to solve in order to determine the saturation scale is,

$$f(r) = \frac{\pi^2}{2N_c} r^2 \alpha_s(\mu^2) x g(x, \mu^2) T(b) - \frac{1}{2} = 0 \tag{4.16}$$

The value of r for which this condition is met gives the saturation scale as $Q_S^2 = \frac{2}{r^2}$. In order to solve this problem, Brent's method begins with the bisection method to isolate the root. Taking an initial guess for r, to be the average squared gluonic radius of the proton, $B_G = 4.0\text{GeV}^2$, and then searching for a place where the value of $f(r)$ changes sign, i.e. $f(a)f(b) < 0$ for two points a and b, will allow us to utilize the bisection method. For a continuous function, a change in sign guarantees a root between the two points with differing signs, *à la* the intermediate value theorem. We will call the current guess b and the guess for which the sign changes a such that $[a, b]$ contains the solution, and require that $|f(b)| \leq |f(a)|$, meaning if this condition is not met, we swap a and b. Thus b is regarded as the better approximation and a third point, c, is initialized by setting $c = a$. Now that the solution is bracketed, we check at each iteration whether $f(b) = 0$ or $|a - b| < \delta$, where δ is the tolerance that we set for the solution. If either condition is satisfied, b is the approximate solution

and the process is complete. Otherwise, the method determines a new trial point b' in the following way: If $f(a) \neq f(c)$ and $f(b) \neq f(c)$, b' is determined using inverse quadratic interpolation

$$b' = \frac{af(b)f(c)}{(f(a)-f(b))(f(a)-f(c))} + \frac{bf(a)f(c)}{(f(b)-f(a))(f(b)-f(c))} + \frac{cf(a)f(b)}{(f(c)-f(a))(f(c)-f(b))} \tag{4.17}$$

Otherwise, b' is determined by linear interpolation

$$b' = \frac{af(b) - bf(a)}{f(b) - f(a)} \tag{4.18}$$

The method maintains values of a,b, and c that satisfy the following conditions at each iteration:

(i) $b \neq c$

(ii) $f(b)f(c) < 0$ such that the solution lies in the interval (a, c) if f is continuous

(iii) $|f(b)| \leq f(c)$ such that b is a better approximate solution than c

(iv) either $a \neq b$ and $a \neq c$, or $a = c$ and a and is the previous value of b

At this point, a relatively complicated set of conditions determines whether to proceed by bisection or interpolation. The method iterates until a zero is found or the procedure converges. Brent's method is a fast, reliable root-finding algorithm that does not require derivatives of the function whose root is being sought. Further details of Brent's method and its numerical implementation can be found at [52, 53].

4.6 Gauge Invariance and Transformations

This section will serve as a review and/or primer on gauge invariance and gauge transformations to facilitate the discussion on lattice gauge theory in the section immediately following this one. It relies heavily on the section regarding gauge variance in Peskin and Schroeder [54] as well as [55] and [56].

As is familiar from classical electrodynamics, gauge fields are only determined up to a total derivative,

$$A_\mu \to A_\mu + \partial_\mu \theta \tag{4.19}$$

which allows the freedom to choose a gauge that will simplify calculations. In modern quantum field theory, however, gauge invariance is taken to be a fundamental symmetry and is used to constrain the types of terms that are allowed in the Lagrangians of gauge invariant theories.

An SU(N) gauge symmetry is a local symmetry of the the form,

$$\phi(x) \to V(x)\phi(x) = e^{i\theta_a(x)\tau_a}\phi(x) \tag{4.20}$$

where $\theta_a(x)$ is known as the gauge parameter and τ_a is an element of SU(N), known as a group generator. The kinetic term for the scalar field, $\partial_\mu\phi\partial^\mu\phi$, is no longer gauge invariant due to the fact that the local gauge invariance allows for independent rotations in SU(N) at different locations. Thus, derivatives, which involve the difference between the scalar field at two distinct points in space-time, are ill defined. To make sense of derivative terms such as

$$\epsilon^\mu\partial_\mu\phi = \lim_{\epsilon\to 0}\frac{1}{\epsilon}[\phi(x+\epsilon) - \phi(x)] \tag{4.21}$$

one can define what is called a "connection," "comparator", or as we will refer to it, a "link", $U(y,x)$, that transforms as

$$U(y,x) \to V(y)U(y,x)V^\dagger(x) \tag{4.22}$$

the idea being that it links two different points by making a quantity located at x, transform as if it is located at y. In this case, one can define the covariant derivative

$$\epsilon^\mu D_\mu\phi = \lim_{\epsilon\to 0}\frac{1}{\epsilon}\left[\phi(x+\epsilon) - U(x+\epsilon,x)\phi(x)\right] \tag{4.23}$$

where the link, as expressed as an expansion of the separation between the two points in the derivative, is

$$U(x+\epsilon,x) = 1 + ig\epsilon^\mu A_\mu(x) + O(\epsilon^2) \tag{4.24}$$

Plugging this form into (69), one gets the covariant derivative,

$$D_\mu = \partial_\mu - igA^a_\mu \tau^a \tag{4.25}$$

As its name would suggest the covariant dervivative transforms covariantly, i.e.,

$$D_\mu \phi(x) \to V(x) D_\mu \phi(x) \tag{4.26}$$

and therefore leaves the kinetic term, involving a product of the derivative and its conjugate, invariant under gauge transformations.

The link in equation (4.24) is essentially the exponent of the gauge field,

$$U(x+\epsilon, x) = \exp\left[ig\epsilon^\mu A_\mu(x)\right] \tag{4.27}$$

This will be important in calculating the field strength tensor, as we will see in the next section.

Alternatively, rather than thinking of the link as a way of preserving gauge invariance, one can think of a path of links that connect two points as the fundamental gauge invariant quantity associated with the gauge field, from which all other gauge invariant quantities can be constructed. This quantity is called the Wilson line and takes the form,

$$U_P(z,y) = P\left\{\exp\left[ig\int_0^1 ds \frac{dx^\mu}{ds} A^a_\mu(x(s))t^a\right]\right\} \tag{4.28}$$

where P denotes the path-ordered integral.

4.7 Lattice Gauge Theory

As in regular gauge theories, one needs to figure out a way to construct a gauge invariant action on the lattice. On the lattice, derivatives involve differences between neighboring lattice sites, connected by the smallest parallel transporter called the link. The link transports the gauge field in the positive direction, whereas its hermitian conjugate moves the field in the opposite direction. From the links, it is possible to

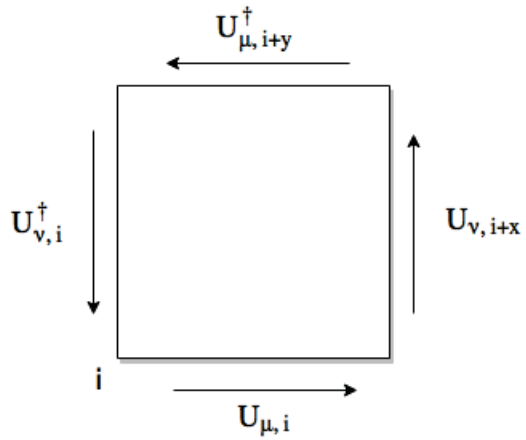

Figure 4.2: Plaquette in the $\mu - \nu$ plane beginning at lattice site i. In the boost invariant case, the lattice is 2-dimensional and we need only worry about the x and y directions. Notice how the hermitian conjugate of a link transports the field in the opposite direction.

construct the field strength by defining the plaquette. The plaquette is the trace of a product of links around a square on the lattice.

Let's see why the plaquette is important. Assuming a two-dimensional lattice with equal lattice spacing in the x and y directions such that $a_x = a_y = a$, and expanding the link

$$U_\mu(x) = \exp\{igaA^a_\mu(x)t^a\} \tag{4.29}$$

$$U_\mu = 1 + igaA^a_\mu t^a - \frac{1}{2}g^2a^2A^a_\mu A^b_\mu t^a t^b + O(a^3) \tag{4.30}$$

Making a loop around a single square in the positive μ and ν directions,

$$U_{\mu\nu} = U_\mu(x)U_\nu(x + a\hat{\mu})U^\dagger_\mu(x + a\hat{\nu})U^\dagger_\nu(x) \tag{4.31}$$

To linear order in the lattice spacing, a, we have

$$U^{(1)}_{\mu\nu} \approx 1 + iga\{A_\mu(x) + A_\nu(x + a\hat{\mu}) - A_\mu(x + a\hat{\nu}) - A_\nu(x)\} \tag{4.32}$$

$$U^{(1)}_{\mu\nu} \approx 1 + iga^2\{\partial_\mu A_\nu - \partial_\nu A_\mu\} \tag{4.33}$$

At second order in the lattice spacing, we pick up the non-abelian term of the field strength,

$$U^{(2)}_{\mu\nu} \approx U^{(1)}_{\mu\nu} - g^2a^2(A^2_\mu + A^2_\nu + A_\mu A_\nu - A_\mu A_\mu - A_\mu A_\nu - A_\nu A_\mu - A_\nu A_\nu + A_\mu A_\nu) \quad (4.34)$$

$$U^{(2)}_{\mu\nu} \approx 1 + iga^2(\partial_\mu A_\nu - \partial_\nu A_\mu) - g^2a^2[A_\mu, A_\nu] = 1 + iga^2F^a_{\mu\nu}t^a \approx \exp\{+iga^2F_{\mu\nu}\} \quad (4.35)$$

This is the plaquette. Its conjugate is found by traversing the square in the reverse direction,

$$U^\dagger_{\mu\nu} \approx 1 - iga^2F^a_{\mu\nu}t^a + \frac{g^2}{2}a^4F^a_{\mu\nu}F^b_{\mu\nu}t^at^b + ... \approx \exp\{-iga^2F_{\mu\nu}\} \quad (4.36)$$

Taking the trace gives us a plaquette and a gauge invariant way of computing the field strength on the lattice. We can take different combinations of plaquettes in order to compute quantities that are relevant for the action or stress-energy tensor, to varying orders of the lattice spacing. For example, to compute the field strength tensor squared, a quantity that will appear in the energy-momentum tensor, we can take

$$\mathrm{Tr}[4 - 2U_{\mu\nu} - 2U^\dagger_{\mu\nu}] = g^2a^4F^a_{\mu\nu}F^a_{\mu\nu} + O(a^6) \quad (4.37)$$

(we have used $\mathrm{Tr}[t^at^b] = \frac{1}{2}\delta^{ab}$)

Alternatively, we can compute the field strength by taking the difference of a plaquette and its hermitian conjugate, thus cancelling all even terms,

$$i\mathrm{Tr}[(U^\dagger_{\mu\nu} - U_{\mu\nu})t^a] = ga^2F^a_{\mu\nu} + O(a^6) \quad (4.38)$$

and then, by squaring it, we have $F^2_{\mu\nu}$ to order a^{12}.

Since we are dealing with an effectively 2-dimensional system, we need not worry about gauge links in the longitudinal direction. This concludes our brief discussion of lattice gauge theory, but this section will inform the lattice implementation of the theory including the equations of motion, and the calculations of the energy-momentum tensor.

4.8 Energy Momentum Tensor on the Lattice

In this section, we will express the stress energy tensor in its discretized form for the lattice calculation. We will define the transverse electric fields $E_{x,y}$ at the midpoint of the links, $i + \frac{e_{\hat{x},y}}{2}$ rather than at the vertices of the lattice. This choice means that the two neighboring lattice sites will each contribute equally to the value of the electric field in the middle of the link. In addition, we will define the stress energy tensor at the middle of the plaquette. Finally, if we absorb a factor of $1/g$ into the transverse electric field components as

$$E^i_{x(y)} \longrightarrow \frac{E^i_{x(y)}}{g} \tag{4.39}$$

and define the quantities for lattice site i,

$$E^2_{lattice,transverse}(i) = \frac{g^2}{2\tau^2}\mathrm{Tr}[E^{x2}_i + E^{x2}_{i+\hat{y}} + E^{y2}_i + E^{y2}_{i+\hat{x}}] \tag{4.40}$$

Note again that there are contributions to each component of the electric field from the two neighboring lattice sites. Further defining,

$$B^2_{lattice,y}(i) = \frac{1}{2\tau^2}\mathrm{Tr}\left[(\phi_i - U_{x,i}\phi_{i+\hat{x}}U^\dagger_{x,i})^2 + (\phi_{i+\hat{y}} - U_{x,i+\hat{y}}\phi_{i+\hat{x}+\hat{y}}U^\dagger_{x,i+\hat{y}})^2\right] \tag{4.41}$$

$$B^2_{lattice,x}(i) = \frac{1}{2\tau^2}\mathrm{Tr}\left[(\phi_i - U_{y,i}\phi_{i+\hat{y}}U^\dagger_{y,i})^2 + (\phi_{i+\hat{x}} - U_{y,i+\hat{x}}\phi_{i+\hat{x}+\hat{y}}U^\dagger_{y,i+\hat{x}})^2\right] \tag{4.42}$$

$$E^2_{lattice,long}(i) = \frac{1}{4}\mathrm{Tr}\left[\pi^2_i + \pi^2_{i+\hat{x}} + \pi^2_{i+\hat{y}} + \pi^2_{i+\hat{x}+\hat{y}}\right] \tag{4.43}$$

Here, because we have treated the longitudinal electric field as a scalar quantity, there are contributions from all four lattice sites comprising a square. Finally,

$$B^2_{lattice,long}(i) = \frac{2}{g^2}\left[N_c - \mathrm{ReTr}(U_{x,i}U_{y,i+\hat{x}}U^\dagger_{x,i+\hat{y}}U^\dagger_{y,i})\right] \tag{4.44}$$

where this is the longitudinal magnetic field squared from (4.37). Alternatively, one can increase the precision in the lattice spacing by taking the difference between the plaquette and its conjugate rather than adding, just as is done in (4.38),

$$B^2_{lattice,long}(i) = \left[-\frac{2}{g}\mathrm{Im}\left(\mathrm{Tr}(U_{x,i}U_{y,i+\hat{x}}U^\dagger_{x,i+\hat{y}}U^\dagger_{y,i})\right)\right]^2 \tag{4.45}$$

or

$$B^2_{lattice,long}(i) = \left[-\frac{i}{2g}(U_{x,i}U_{y,i+\hat{x}}U^\dagger_{x,i+\hat{y}}U^\dagger_{y,i} - U_{y,i}U_{x,i+\hat{y}}U^\dagger_{y,i+\hat{x}}U^\dagger_{x,i} - \mathrm{trace})\right]^2 \tag{4.46}$$

The latter expression is implemented in the code for the work presented here. Once again, "−trace" means subtract the diagonal elements of the matrix. From these four terms, we can construct the diagonal components of $T^{\mu\nu}$at lattice site i,

$$\begin{aligned}
T^{\tau\tau} &= E^2_{lattice,trans} + E^2_{lattice,long} + B^2_{lattice,x} + B^2_{lattice,y} + B^2_{lattice,long} \\
T^{xx} &= E^2_{lattice,trans} + E^2_{lattice,long} - B^2_{lattice,x} + B^2_{lattice,y} + B^2_{lattice,long} \\
T^{yy} &= E^2_{lattice,trans} + E^2_{lattice,long} + B^2_{lattice,x} - B^2_{lattice,y} + B^2_{lattice,long} \\
T^{\eta\eta} &= E^2_{lattice,trans} - E^2_{lattice,long} + B^2_{lattice,x} + B^2_{lattice,y} - B^2_{lattice,long}
\end{aligned} \tag{4.47}$$

Thus, $T^{\mu\nu}$ is manifestly traceless. Because $T^{\mu\nu}$ is symmetric, there are only six additional independent components, for a total of ten. The remaining components are

$$\begin{aligned}
T^{\tau x}_i = \frac{1}{4\tau}\mathrm{Tr}\Big[&- iE^y_i\Big(U_{y,i}U_{x,i+\hat{y}}U^\dagger_{y,i+\hat{x}}U^\dagger_{x,i} - U_{x,i}U_{y,i+\hat{x}}U^\dagger_{x,i+\hat{y}}U^\dagger_{y,i} - \frac{1}{N_c}\mathrm{trace} \\
&+ U^\dagger_{x,i-\hat{x}}U_{y,i-\hat{x}}U_{x,i-\hat{x}+\hat{y}}U^\dagger_{y,i} - U_{y,i}U^\dagger_{x,i-\hat{x}+\hat{y}}U^\dagger_{y,i-\hat{x}}U_{x,i-\hat{x}} - \frac{1}{N_c}\mathrm{trace}\Big) \\
&- iE^y_{i+\hat{x}}\Big(U_{y,i+\hat{x}}U_{x,i+\hat{x}+\hat{y}}U^\dagger_{y,i+2\hat{x}}U^\dagger_{x,i+\hat{x}} - U_{x,i+\hat{x}}U_{y,i+2\hat{x}}U^\dagger_{x,i+\hat{x}+\hat{y}}U^\dagger_{y,i+\hat{x}} - \frac{1}{N_c}\mathrm{trace} \\
&+ U^\dagger_{x,i}U_{y,i}U_{x,i+\hat{y}}U^\dagger_{y,i+\hat{x}} - U_{y,i+\hat{x}}U^\dagger_{x,i+\hat{y}}U^\dagger_{y,i}U_{x,i} - \frac{1}{N_c}\mathrm{trace}\Big) \\
&- \pi_i\Big(U_{x,i}\phi_{i+\hat{x}}U^\dagger_{x,i} - U^\dagger_{x,i-\hat{x}}\phi_{i-\hat{x}}U_{x,i-\hat{x}}\Big) - \pi_{i+\hat{y}}\Big(U_{x,i+\hat{y}}\phi_{i+\hat{x}+\hat{y}}U^\dagger_{x,i+\hat{y}} - U^\dagger_{x,i-\hat{x}+\hat{y}}\phi_{i-\hat{x}+\hat{y}}U_{x,i-\hat{x}+\hat{y}}\Big) \\
&- \pi_{i+\hat{x}}\Big(U_{x,i+\hat{x}}\phi_{i+2\hat{x}}U^\dagger_{x,i+\hat{x}} - U^\dagger_{x,i}\phi_iU_{x,i}\Big) - \pi_{i+\hat{x}+\hat{y}}\Big(U_{x,i+\hat{x}+\hat{y}}\phi_{i+2\hat{x}+\hat{y}}U^\dagger_{x,i+\hat{x}+\hat{y}} - U^\dagger_{x,i+\hat{y}}\phi_{i+\hat{y}}U_{x,i+\hat{y}}\Big)\Big]
\end{aligned} \tag{4.48}$$

Similarly,

$$
\begin{aligned}
T_i^{\tau y} = \frac{1}{4\tau}\mathrm{Tr}\Big[& - iE_i^x\Big(U_{x,i}U_{y,i+\hat{x}}U_{x,i+\hat{y}}^\dagger U_{y,i}^\dagger - U_{y,i}U_{x,i+\hat{y}}U_{y,i+\hat{x}}^\dagger U_{x,i}^\dagger - \frac{1}{N_c}\mathrm{trace} \\
& + U_{y,i-\hat{y}}^\dagger U_{x,i-\hat{y}}U_{y,i-\hat{y}+\hat{x}}U_{x,i}^\dagger - U_{x,i}U_{y,i-\hat{y}+\hat{x}}^\dagger U_{x,i-\hat{y}}^\dagger U_{y,i-\hat{y}} - \frac{1}{N_c}\mathrm{trace}\Big) \\
& - iE_{i+\hat{y}}^x\Big(U_{x,i+\hat{y}}U_{y,i+\hat{y}+\hat{x}}U_{x,i+2\hat{y}}^\dagger U_{y,i+\hat{y}}^\dagger - U_{y,i+\hat{y}}U_{x,i+2\hat{y}}U_{y,i+\hat{x}+\hat{y}}^\dagger U_{x,i+\hat{y}}^\dagger - \frac{1}{N_c}\mathrm{trace} \\
& + U_{y,i}^\dagger U_{x,i}U_{y,i+\hat{x}}U_{x,i+\hat{y}}^\dagger - U_{x,i+\hat{y}}U_{y,i+\hat{x}}^\dagger U_{x,i}^\dagger U_{y,i} - \frac{1}{N_c}\mathrm{trace}\Big) \\
& - \pi_i\Big(U_{y,i}\phi_{i+\hat{y}}U_{y,i}^\dagger - U_{y,i-\hat{y}}^\dagger\phi_{i-\hat{y}}U_{y,i-\hat{y}}\Big) - \pi_{i+\hat{x}}\Big(U_{y,i+\hat{x}}\phi_{i+\hat{x}+\hat{y}}U_{y,i+\hat{x}}^\dagger - U_{y,i-\hat{y}+\hat{x}}^\dagger\phi_{i-\hat{y}+\hat{x}}U_{y,i-\hat{y}+\hat{x}}\Big) \\
& - \pi_{i+\hat{y}}\Big(U_{y,i+\hat{y}}\phi_{i+2\hat{y}}U_{y,i+\hat{y}}^\dagger - U_{y,i}^\dagger\phi_i U_{y,i}\Big) - \pi_{i+\hat{x}+\hat{y}}\Big(U_{y,i+\hat{x}+\hat{y}}\phi_{i+2\hat{y}+\hat{x}}U_{y,i+\hat{x}+\hat{y}}^\dagger - U_{y,i+\hat{x}}^\dagger\phi_{i+\hat{x}}U_{y,i+\hat{x}}\Big)\Big]
\end{aligned}
\tag{4.49}
$$

Finally, for the last spatial-temporal component,

$$
\begin{aligned}
T^{\tau\eta} = \frac{g}{\tau^3}\mathrm{Tr}\Big[& E_i^x\Big(U_{x,i}\phi_{i+\hat{x}}U_{x,i}^\dagger - \phi_i\Big) + E_{i+\hat{y}}^x\Big(U_{x,i+\hat{y}}\phi_{i+\hat{x}+\hat{y}}U_{x,i+\hat{y}}^\dagger - \phi_{i+\hat{y}}\Big) \\
& + E_i^y\Big(U_{y,i}\phi_{i+\hat{y}}U_{y,i}^\dagger - \phi_i\Big) + E_{i+\hat{x}}^y\Big(U_{y,i+\hat{x}}\phi_{i+\hat{x}+\hat{y}}U_{y,i+\hat{x}}^\dagger - \phi_{i+\hat{x}}\Big)\Big]
\end{aligned}
\tag{4.50}
$$

For the purely spatial components,

$$
\begin{aligned}
T_i^{xy} = \frac{1}{2\tau^2}\mathrm{Tr}\Big[& - g^2\Big(E_i^x + U_{y,i}E_{i+\hat{y}}U_{y,i}^\dagger\Big)\Big(E_i^y + U_{x,i}E_{i+\hat{x}}U_{x,i}^\dagger\Big) \\
& + \Big(U_{x,i}\phi_{i+x}U_{x,i}^\dagger - \phi_i\Big)\Big(U_{y,i}\phi_{i+y}U_{y,i}^\dagger - \phi_i) + U_{y,i}\Big(U_{x,i+\hat{y}}\phi_{i+\hat{x}+\hat{y}}U_{x,i+\hat{y}}^\dagger - \phi_{i+\hat{y}}\Big)U_{y,i}^\dagger\Big(U_{y,i}\phi_{i+\hat{x}}U_{y,i}^\dagger - \phi_i\Big) \\
& + \Big(U_{x,i}\phi_{i+\hat{x}}U_{x,i}^\dagger - \phi_i\Big)U_{x,i}\Big(U_{y,i+\hat{x}}\phi_{i+\hat{x}+\hat{y}}U_{y,i+\hat{x}}^\dagger - \phi_{i+\hat{x}}\Big)U_{x,i}^\dagger \\
& + U_{y,i}\Big(U_{x,i+\hat{y}}\phi_{i+\hat{x}+\hat{y}}U_{x,i+\hat{y}}^\dagger - \phi_{i+\hat{y}}\Big)U_{y,i}^\dagger U_{x,i}\Big(U_{y,i+\hat{x}}\phi_{i+\hat{x}+\hat{y}}U_{y,i+\hat{x}}^\dagger - \phi_{i+\hat{x}}\Big)U_{x,i}^\dagger\Big]
\end{aligned}
\tag{4.51}
$$

For the spatial-η components,

$$
\begin{aligned}
T_i^{x\eta} = &-\frac{2}{\tau^2}\mathrm{Tr}\Bigg\{\frac{g}{4}\Big[E_i^x\Big(\pi_i + U_{x,i}\pi_{i+\hat{x}}U_{x,i}^\dagger\Big) + E_{i+\hat{y}}^x\Big(\pi_{i+\hat{y}} + U_{x,i+\hat{y}}\pi_{i+\hat{x}+\hat{y}}U_{x,i+\hat{y}}^\dagger\Big)\Big] \\
&+ \frac{1}{8ig}\Big[\Big(U_{x,i}U_{y,i+\hat{x}}U_{x,i+\hat{y}}^\dagger U_{y,i}^\dagger - U_{y,i}U_{x,i+\hat{y}}U_{y,i+\hat{x}}^\dagger U_{x,i}^\dagger - \frac{1}{N_c}\mathrm{trace} \\
&+ U_{y,i}U_{x,i-\hat{x}+\hat{y}}^\dagger U_{y,i-\hat{x}}^\dagger U_{x,i-\hat{x}} - U_{x,i-\hat{x}}^\dagger U_{y,i-\hat{x}}U_{x,i-\hat{x}+\hat{y}}U_{y,i}^\dagger - \frac{1}{N_c}\mathrm{trace}\Big)\Big(U_{y,i}\phi_{i+\hat{y}}U_{y,i}^\dagger - \phi_i\Big) \\
&+ \Big(U_{y,i+\hat{x}}U_{x,i+\hat{y}}^\dagger U_{y,i}^\dagger U_{x,i} - U_{x,i}^\dagger U_{y,i}U_{x,i+\hat{y}}U_{y,i+\hat{x}}^\dagger - \frac{1}{N_c}\mathrm{trace} \\
&+ U_{x,i+\hat{x}}U_{y,i+2\hat{x}}U_{y,i+\hat{x}+\hat{y}}^\dagger U_{x,i+\hat{x}}^\dagger - U_{y,i+\hat{x}}U_{y,i+\hat{x}+\hat{y}}U_{x,i+2\hat{x}}^\dagger U_{x,i+\hat{x}}^\dagger - \frac{1}{N_c}\mathrm{trace}\Big) \\
&\times \Big(U_{y,i+\hat{x}}\phi_{i+\hat{x}+\hat{y}}U_{y,i+\hat{x}}^\dagger - \phi_{i+\hat{x}}\Big)\Big]\Bigg\}
\end{aligned}
\tag{4.52}
$$

and finally,

$$
\begin{aligned}
T_i^{y\eta} = &-\frac{2}{\tau^2}\mathrm{Tr}\Bigg\{\frac{g}{4}\Big[E_i^y\Big(\pi_i + U_{y,i}\pi_{i+\hat{y}}U_{y,i}^\dagger\Big) + E_{i+\hat{x}}^y\Big(\pi_{i+\hat{x}} + U_{y,i+\hat{x}}\pi_{i+\hat{x}+\hat{y}}U_{y,i+\hat{x}}^\dagger\Big)\Big] \\
&+ \frac{1}{8ig}\Big[\Big(U_{y,i}U_{x,i+\hat{y}}U_{y,i+\hat{x}}^\dagger U_{x,i}^\dagger - U_{x,i}U_{y,i+\hat{x}}U_{x,i+\hat{y}}^\dagger U_{y,i}^\dagger - \frac{1}{N_c}\mathrm{trace} \\
&+ U_{x,i}U_{y,i+\hat{x}-\hat{y}}^\dagger U_{x,i-\hat{y}}^\dagger U_{y,i-\hat{y}} - U_{y,i-\hat{y}}^\dagger U_{x,i-\hat{y}}U_{y,i+\hat{x}-\hat{y}}U_{x,i}^\dagger - \frac{1}{N_c}\mathrm{trace}\Big)\Big(U_{x,i}\phi_{i+\hat{x}}U_{x,i}^\dagger - \phi_i\Big) \\
&+ \Big(U_{x,i+\hat{y}}U_{y,i+\hat{x}}^\dagger U_{x,i}^\dagger U_{y,i} - U_{y,i}^\dagger U_{x,i}U_{y,i+\hat{x}}U_{x,i+\hat{y}}^\dagger - \frac{1}{N_c}\mathrm{trace} \\
&+ U_{y,i+\hat{y}}U_{x,i+2\hat{y}}U_{y,i+\hat{x}+\hat{y}}^\dagger U_{x,i+\hat{y}}^\dagger - U_{x,i+\hat{y}}U_{y,i+\hat{x}+\hat{y}}U_{x,i+2\hat{y}}^\dagger U_{y,i+\hat{y}}^\dagger - \frac{1}{N_c}\mathrm{trace}\Big) \\
&\Big(U_{x,i+\hat{y}}\phi_{i+\hat{x}+\hat{y}}U_{x,i+\hat{y}}^\dagger - \phi_{i+\hat{y}}\Big)\Big]\Bigg\}
\end{aligned}
\tag{4.53}
$$

5

Description of Observables and Results

5.1 Spatial and Momentum Anisotropies: ϵ_n and v_n

As discussed in the introduction, one of the key signatures of QGP is the second Fourier coefficient of the expansion of the azimuthal distribution of particles,

$$\frac{dN}{p_T dp_T dy d\phi} = \frac{dN}{2\pi p_T dp_T dy}\left(1 + \sum_n 2v_n(y, p_T)\cos\left[n(\phi - \psi_n)\right]\right) \tag{5.1}$$

Each coefficient in this expansion, v_n, corresponds to a different shape of flow. The first coefficient, v_1, represents directed flow, whereas v_3 is a measure of triangular flow. The second harmonic, v_2, on the other hand, corresponds to the elliptic flow of the medium and is intimately linked to ϵ_2, which is a measure of the elliptic shape of the distribution of energy in the initial state that gets converted by hydrodynamic flow from a pressure anisotropy to a momentum anisotropy. In fact, this relation between ϵ_2 and v_2 is more generally true of the n-th harmonic. However, it is most clearly illustrated, and in fact most important, in the case of v_2, due to the initial geometry of colliding nuclei at finite impact parameter. The efficiency by which hydrodynamics converts the initial ϵ_n energy configuration from IP-Glasma, given in figure (5.1) , can be seen by the ratio of $\langle v_n \rangle / \langle \epsilon_n \rangle$ as given in plot (5.2). There are many definitions for computing v_n flow coefficients. In this work, we used the scalar product method, more details on which can be found in appendix (7.4).

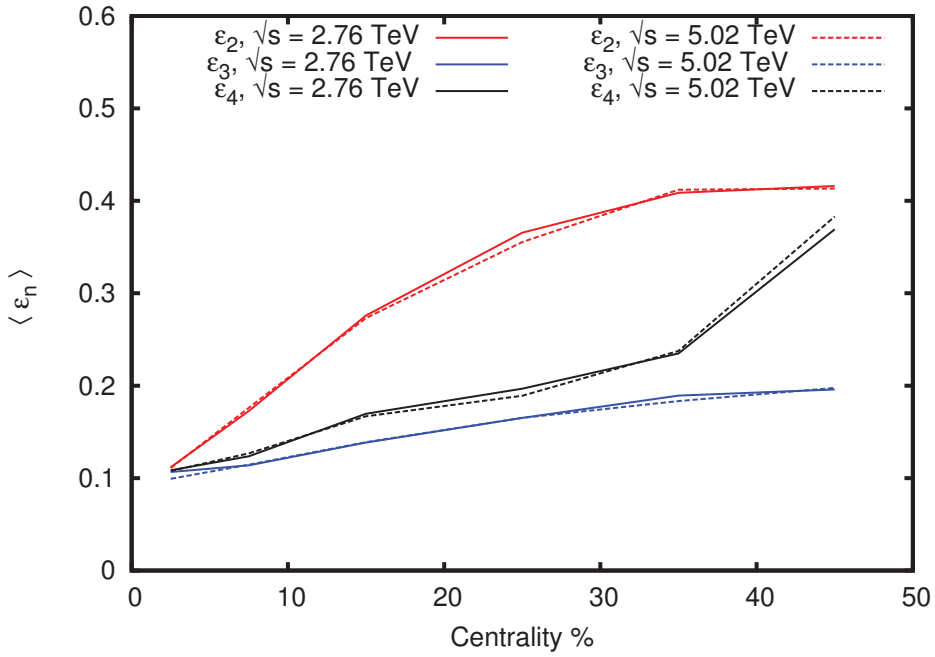

Figure 5.1: $\langle \epsilon_n \rangle$ at 5.02 TeV and 2.76 TeV for 1500 events per 10% centrality class. Note that the values of $\langle \epsilon_n \rangle$ are the same within statistical fluctuations for the two LHC collision energies.

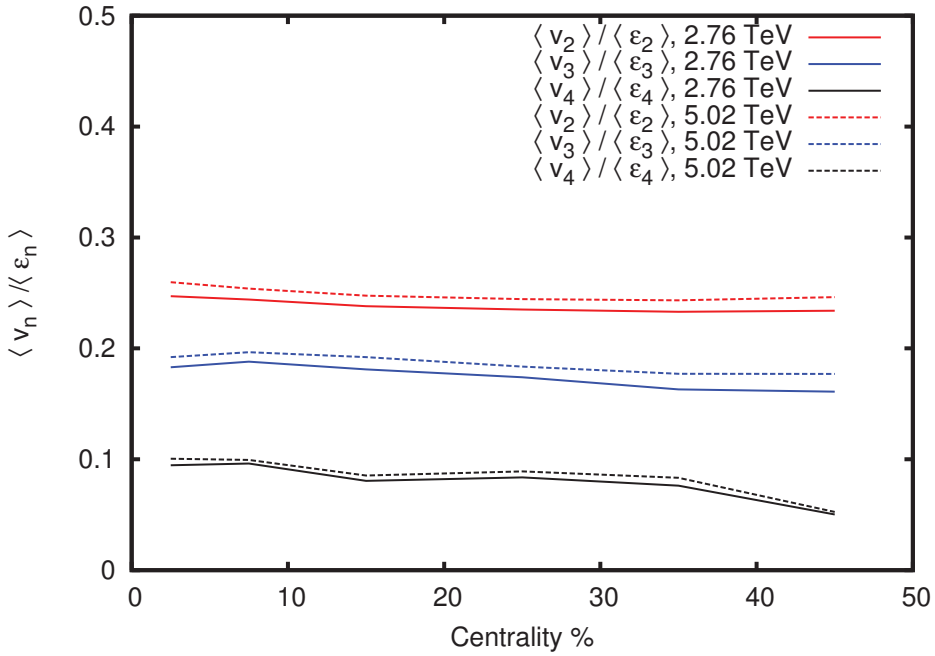

Figure 5.2: The event averaged integrated v_n in ratio to the event averaged ϵ_n $\langle v_n \rangle / \langle \epsilon_n \rangle$ at 5.02 TeV and 2.76 TeV. The longer lifetime of the fireball at the higher energy allows more time for the flow harmonics to develop.

5.1.1 Centrality Selection

Centrality has been determined by the minimum bias method. This entails randomly sampling the impact parameter, b, from 0-20 fm, according to $P(b)db = \frac{bdb}{b_{max}^2/2}$, and binning events according to their total energy in intervals, with 0-5% being the 5% of events with the highest total energy. This process is closest to what is done by experimentalists, who bin events on charged particle multiplicity. The criteria for determining the 100% centrality cutoff, or equivalently the threshold for whether an event occurred, is not as clear in the IP-Glasma framework as in, for example, the Glauber model. This is due to the fact that IP-Glasma is composed of gluon fields, and thus there can be gluon field interactions without what would be considered a binary, or nucleon-nucleon, collision in the Glauber model. For the purpose of this thesis, the boundary for the 100% centrality bin was taken such that the ratio of centrality bins fits the dN_{ch}/dy distribution from experimental data. Thus, we used this cutoff as a parameter that we fit to data, and once this 100% centrality determination was made, all other centralities became fixed.

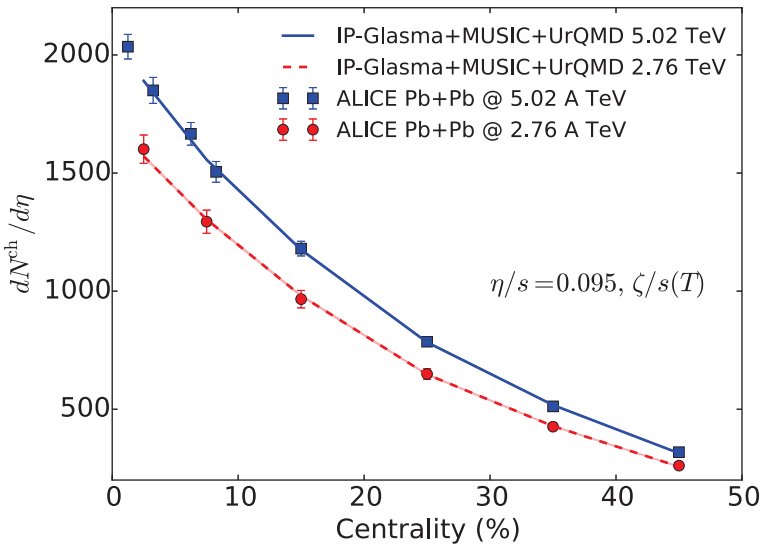

Figure 5.3: Charged particle multiplicity $\frac{dN_{ch}}{dy}$ as a function of centrality for 2.76 TeV[57] and 5.02 TeV [58].

At 2.76 TeV, the boundary that we determined for 100% centrality corresponded

to an energy of ≈ 0.4 GeV per unit rapidity, which for a plateau region of 10 rapidity units, gives a total energy of 4 GeV. The maximum saturation scale at this energy is 2 GeV, meaning that the effective criterion set for whether a collision occurred was the creation of two gluons at the saturation scale. We varied the boundary by a factor of two and the results were insensitive to the exact choice of cutoff. For 5.02 TeV, the maximum value of the saturation scale increases to about 2.25 GeV, and thus the 100% centrality threshold is slightly higher.

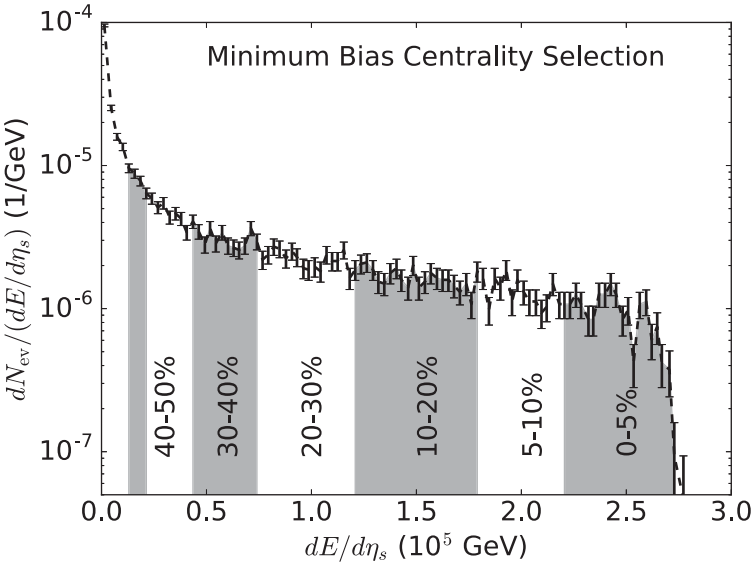

Figure 5.4: Minimum bias centrality selection histogram for 12,000 events at 2.76 TeV.

5.2 Results - Pb-Pb at 2.76 TeV vs. 5.02 TeV

5.2.1 Overview of Results

The results presented here consist of 1500 events per 10% centrality class for a total of 7500 events from 0-50%. IP-Glasma is run on a 1000×1000 grid with a lattice spacing $a = 0.1$ GeV^{-1}, which is then course grained for a lattice spacing of 0.5 GeV^{-1} for the hydrodynamic simulation, MUSIC. Time steps are taken to be $d\tau = 0.01$ GeV$^{-1} \approx 0.002$ fm for IP-Glasma and the system is evolved to a hydro switching time of 0.4 fm.

Qualitatively, the results at the two LHC energies are very similar. The quantitative differences are generally on the single percentage level. The charged hadron v_2

for example only increases by a few percentage points at the higher energy, as shown in figure (5.5) with good agreement with data. Measurements of many other observ-

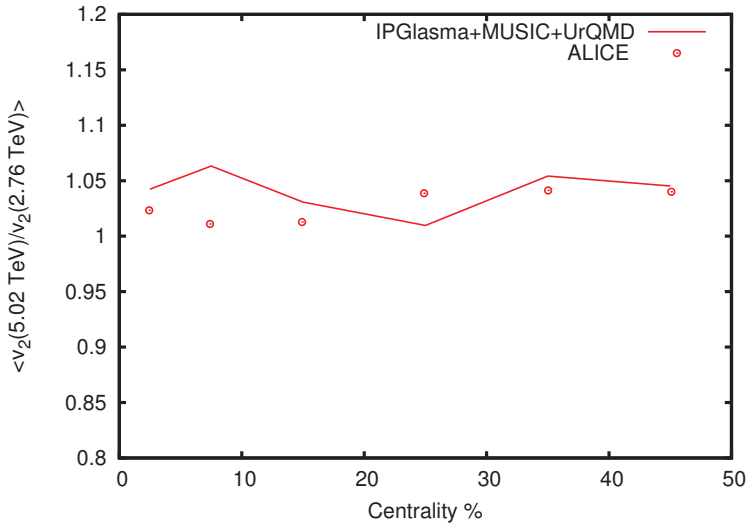

Figure 5.5: The ratio of v_2 for the two LHC energies as a function of centrality. Data taken from the ALICE Collaboration [59].

ables, at the time of this writing have yet to be published at 5.02 TeV, and thus the results presented serve as predictions from the IP-Glasma+MUSIC+UrQMD framework. These predictions follow a similar trend of qualitative agreement with slight quantitative increases, as compared to 2.76 TeV. Quantities for which data has yet to be published at 5.02 TeV include the particle spectra (fig. (5.9)), v_n distributions (fig. (5.9)), identified particle differential v_n's (figs. (5.7)), v_n correlations (figs. (5.13), (5.14)), and mean p_T (fig. (5.10)).

In terms of IP-Glasma, the initial state eccentricities are the same within statistical fluctuations for the two energies and the average initial flow, as characterized by $\langle u^{\perp} \rangle$, is 2-3% larger, on average, at 5.02 TeV compared to 2.76 TeV.

5.2.2 *Differential v_n's*

We can also look at v_n flow harmonics as a function of p_T. From figure (5.7), one can see that our results match the data far better at 0-5% centrality in the 1-2 GeV p_T range compared to more peripheral events. This is because high p_T physics such as jets and mini-jets, plays a much larger role in peripheral collisions. Such high p_T

components are not part of the collective behavior of the QGP medium and thus do not develop the same anisotropies as low p_T partons. Our calculation, which does not include jets, lacks these lower v_n high p_T contributions that would bring the curves down in the $p_T > 1.0$ GeV region. This is a clear sign that high p_T physics is needed to complete the picture.

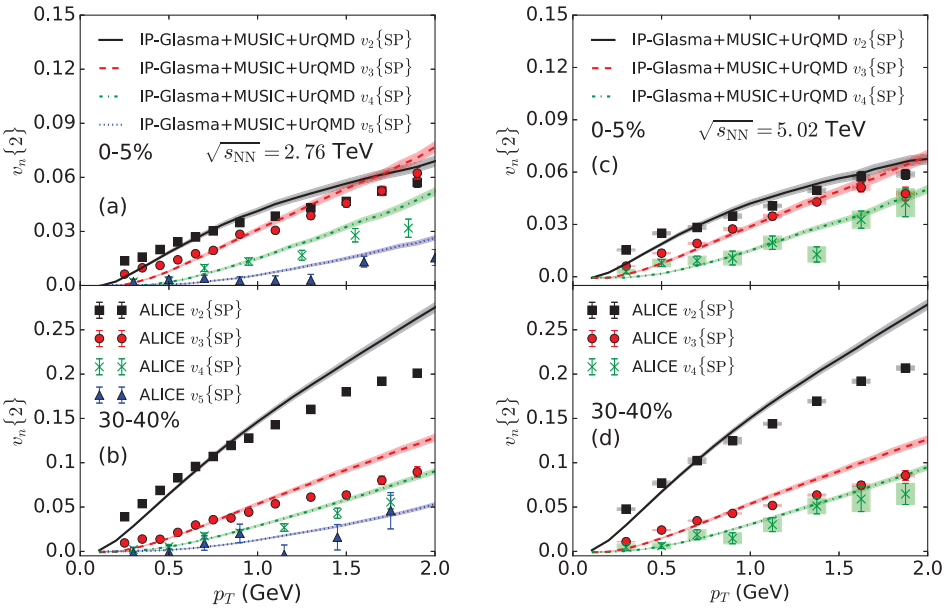

Figure 5.6: Differential v_n for charged hadrons in 0-5% (a, c) and 30-40% (b, d) centrality bins in Pb+Pb collisions at 2.76 (a, b) and 5.02 (c, d) A TeV. Experimental data taken from [60, 61].

It should also be noted that far better agreement has been achieved for differential v_n's using only shear viscosity in other studies. Bulk viscosity, which is necessary for other observables such as $\langle p_T \rangle$, acts isotropically and does not develop flow anisotropies. Its inclusion requires a decreased shear, however, since some of the viscous effects will be taken care of by bulk in this case. Thus, with a lower shear viscosity, the slope of the differential v_n's changes and tends to miss the higher p_T region of hydrodynamic applicability.

In the identified particle differential v_n in figure (5.7) there is a clear mass ordering between the protons, kaons, and pions. This is due to the fact that as the fluid hadronizes, the particles are boosted from the local rest frame of the fluid cell to the lab frame. Given the same velocity, the heavier particles have a greater momentum

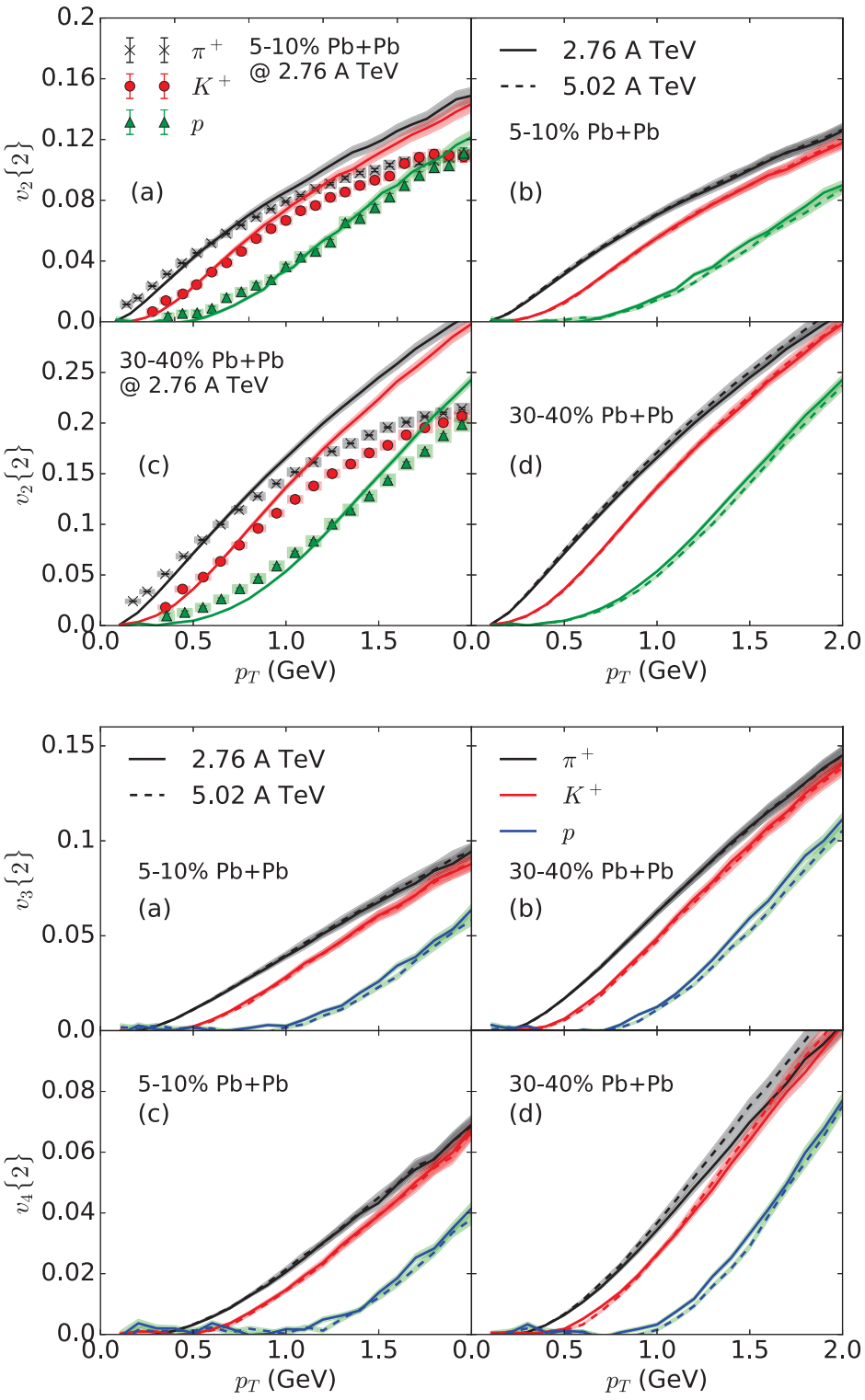

Figure 5.7: Top: Identified particle differential v_2 for (a) 5-10% at 2.76 TeV vs ALICE data [62] (b) 5-10% comparison between LHC energies (c) 30-40% at 2.76 vs ALICE data (d) 30-40% comparison between LHC energies. Bottom: Differential v_3 for (a) charged hadrdons 5-10% at 2.76 TeV and 5.02 TeV (b) identified particles 5-10% at 2.76 TeV and 5.02 TeV and differential v_4 for (c) charged hadrons 30-40% at 2.76 TeV and 5.02 TeV (d) identified particles 30-40% at 2.76 TeV and 5.02 TeV

which blue shifts their differential v_n to higher p_T.

5.2.3 Integrated v_n

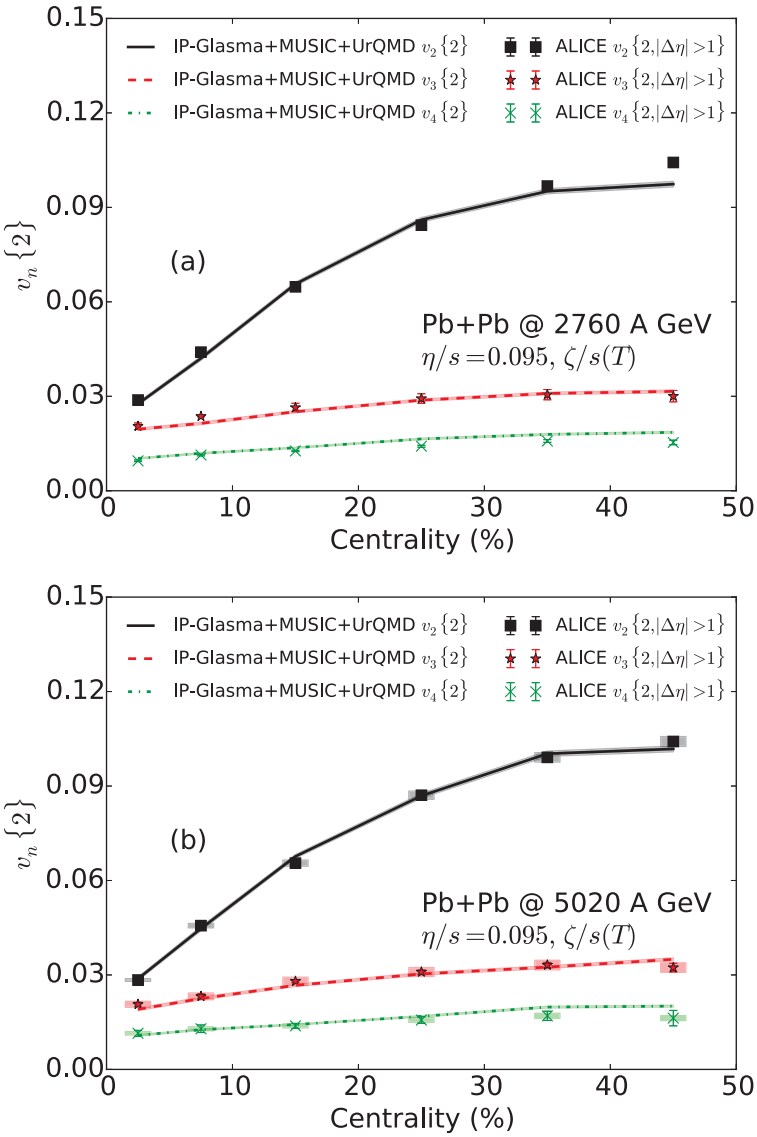

Figure 5.8: Integrated v_n as a function of centrality at 2.76 TeV and 5.02 TeV, as compared to ALICE data [59]

As can be seen, despite nearly identical ϵ_n values for the two LHC collision energies in figure (5.1), the higher energy has consistently larger v_n. Higher temperature results in a longer lifetime of the fireball since it will take longer for the system to cool to the freezeout temperature, where the QGP hadronizes back into particles and the

collective behavior ceases. A longer lifetime thus allows more time for the collective behavior, as governed by hydrodynamics, to convert the initial energy anisotropies into momentum anisotropies. Hence we see larger v_n values at the higher energy.

5.2.4 v_n distributions

While v_2 is driven primarily by the initial geometry of the system, higher harmonics such as v_3 are fluctuation driven and are described well by the IP-Glasma model, a feat that is rare among initial state models. In addition, as was shown in [63] the IP-Glasma framework is not only able to reproduce event-averaged flow data but, indeed, is able to reproduce the event-by-event v_n distributions amazingly well, as in fig. (5.9). Further note how closely the v_n distributions track the corresponding ϵ_n distributions, an indication that the initial state is behind the successful reproduction of the v_n distributions. This result suggests that the initial state fluctuations in the IP-Glasma model accurately capture the physical fluctuations in the initial state of HIC's.

5.2.5 Mean Transverse Momentum: $\langle p_T \rangle$

IP-Glasma initial conditions generate large pressure gradients that lead to high mean p_T. It was shown in [43] that bulk viscosity can remedy this situation by slowing the radial expansion of the fluid. Using the bulk parametrization given in this thesis, we accurately describe the pion $\langle p_T \rangle$ but underestimate the heavier kaon and proton data. The inclusion of re-scatterings in UrQMD generates increased mean p_T for these heavier hadrons and we end up within 10% of the data at all centralities. The effect UrQMD on the $\langle p_T \rangle$ can be seen by comparing the dashed line, without UrQMD, with the solid line, with UrQMD, in figure (5.10)

It is worth noting that one could also increase the mean p_T by allowing hydrodynamics to evolve to a lower temperature, since hydrodynamics will generate transverse momentum. Doing so, however, would compromise the charged hadron multiplicities of the heavier hadrons since the energy density at freeze out would be too low to produce many of these heavy particles. The amazing thing about the results shown

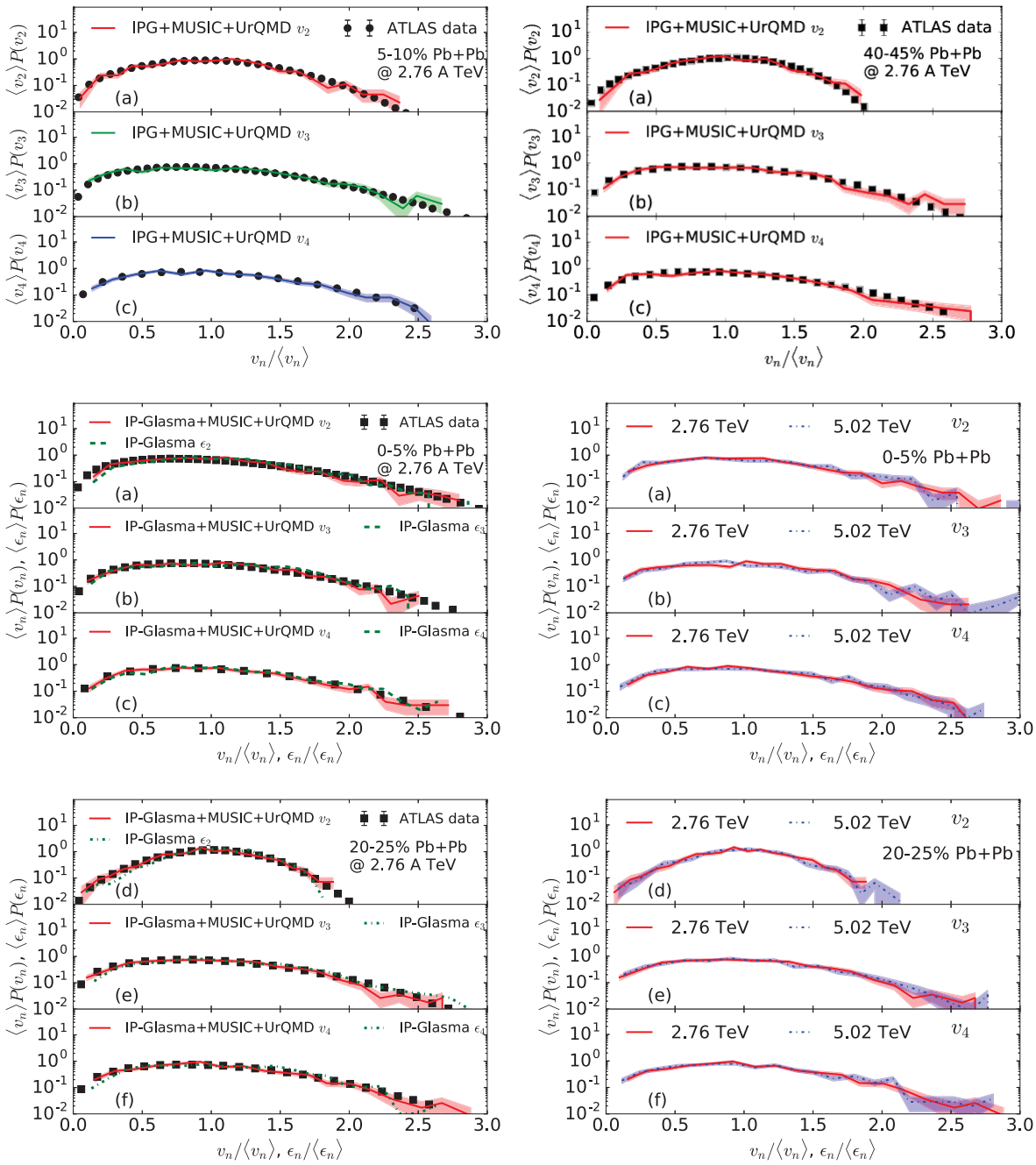

Figure 5.9: Event-by-event $\frac{v_n}{\langle v_n\rangle}$ and $\frac{\epsilon_n}{\langle\epsilon_n\rangle}$ distributions for Pb-Pb at 2.76 TeV in the 5-10% (top left) and 40-45% (top right) centrality bin, for 2.76 TeV in the 0-5% centrality bin compared to ATLAS data (middle left), between collision energies in 0-5% centrality bin (middle right), 2.76 TeV in the 20-25% centrality bin compared to ATLAS data (bottom left), and a comparison between collision energies in the 20-25% centralily bin (bottom right) Data from the ATLAS collaboration [64].

here is that we are able to simultaneously describe charged hadron multiplicities, v_n's, spectra, and mean p_T.

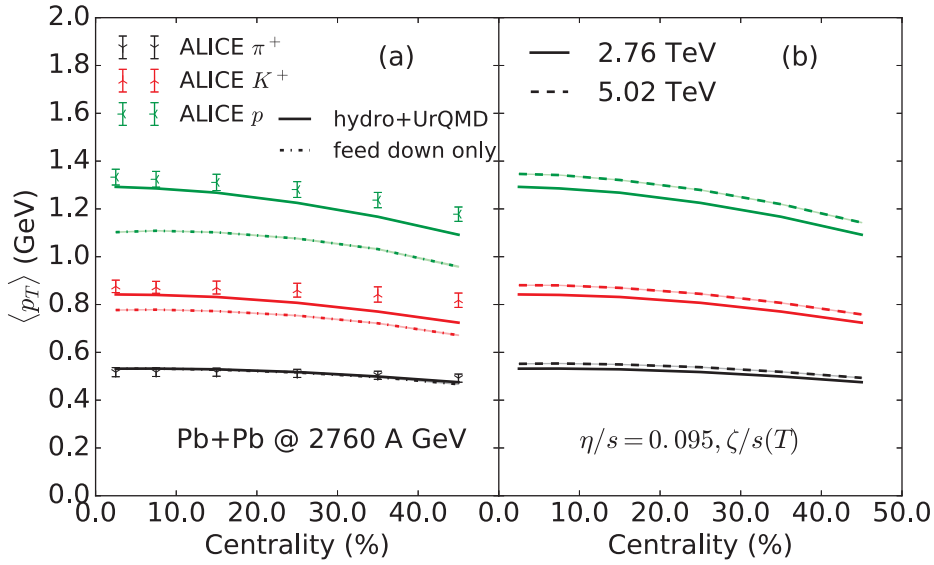

Figure 5.10: Identified particle $\langle p_T \rangle$ as a function of centrality (a) vs ALICE data [65] and (b) a comparison between LHC energies.

5.2.6 Particle Spectra and Identified Particle Multiplicity

The identified particle spectra quantify the transverse momentum distributions of individual particle species and are shown for pions, kaons, protons and multi-strange particles in figure (5.12). It is important to note that hadronic re-scatterings from UrQMD are necessary to adequately describe data for the heavier particles, such as kaons, and especially protons. The identified particle multiplicity in figure (5.11) shows that we are not only able to reproduce the centrality dependence of the charged particle multiplicity, but that our thermal sampling in the Cooper-Frye particlization procedure, along with the UrQMD dynamics are able to accurately produce the correct identified particle multiplicities as well.

5.2.7 v_n Correlations

This is the first time v_n correlations have been calculated for IP-Glasma initial conditions. Non-trivial v_n correlations in good agreement with data provide a strong indication that the initial state energy distributions of IP-Glasma are physical. Smooth initial conditions, which are sometimes used to initialize hydrodynamics in HIC simulations, cannot possibly reproduce the rich structure of these fascinating observables.

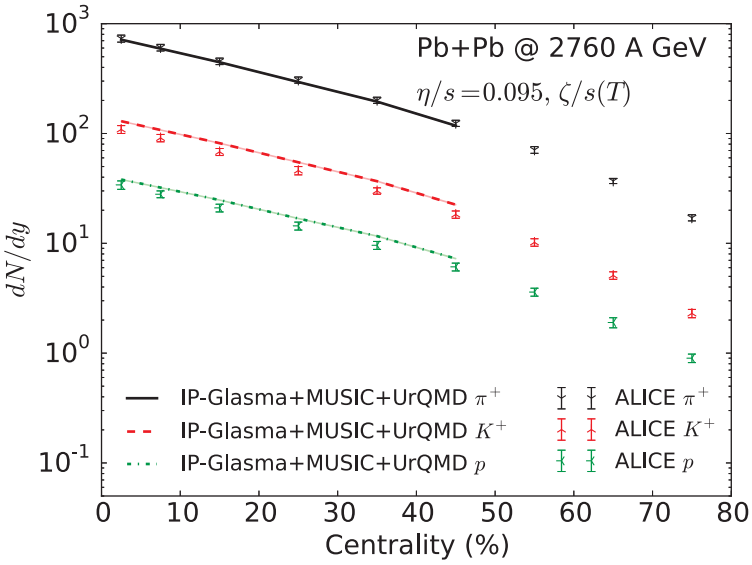

Figure 5.11: Identified particle multiplicities $\frac{dN}{dy}$ as a function of centrality

Take a smooth initial condition that is a perfect ellipse, for example. It will have vanishing odd flow coefficients and v_2-v_4 correlations, due to symmetry. The same smooth initial condition may be able to adequately reproduce v_2, however. Thus, v_n correlations give us a deeper insight into the initial state, that goes beyond the flow coefficients themselves. For details on how v_n correlations were computed in this work see appendix (7.5).

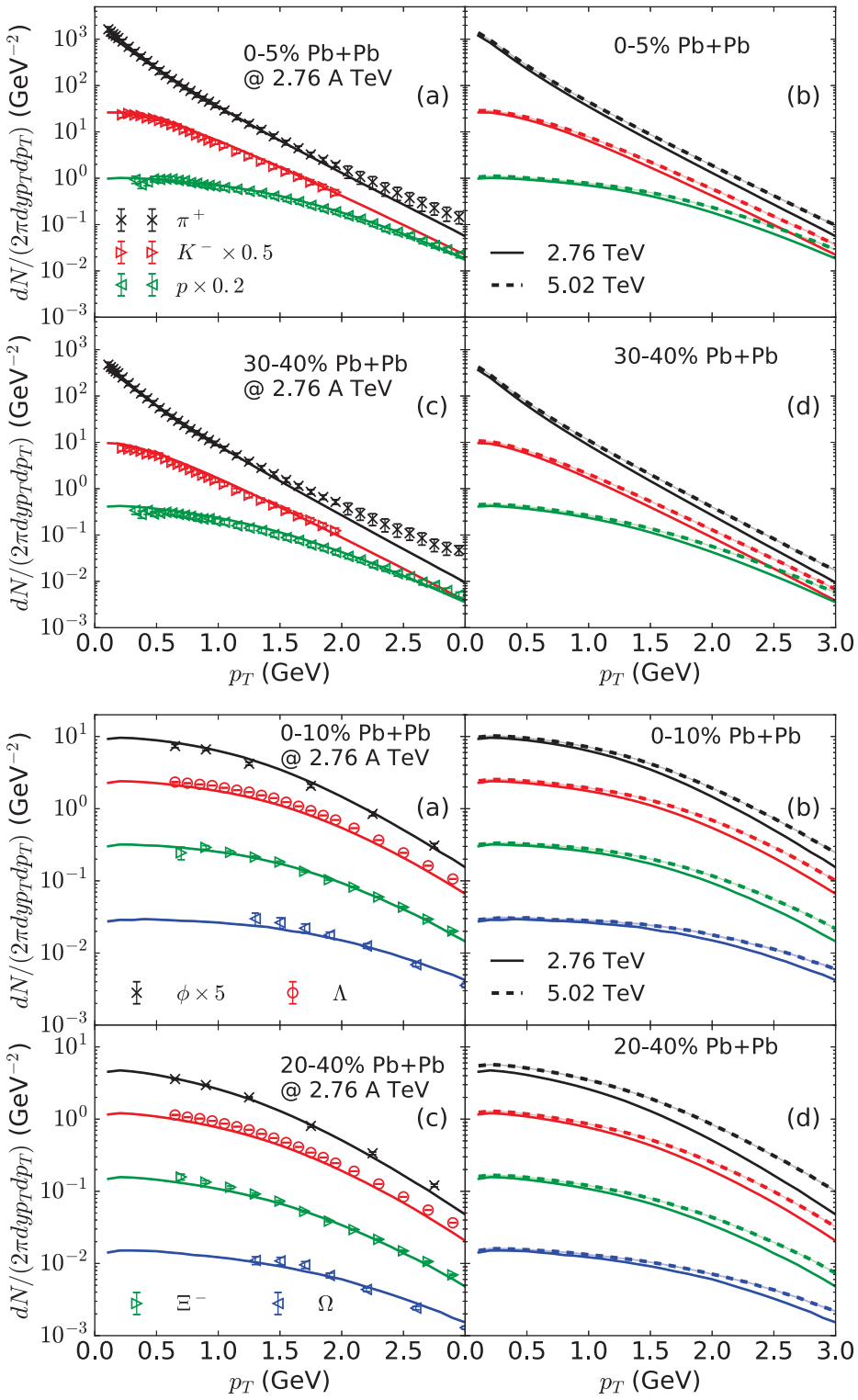

Figure 5.12: Top: Identified particle spectra at two centralities (a),(c) comparison with ALICE data [65] at 2.76 TeV and (b),(d) prediction and comparison between the two LHC energies. Bottom: Strange particle spectra at two centralities (a),(c) comparison with data at 2.76 TeV, and (b),(d) prediction and comparison between the two LHC energies

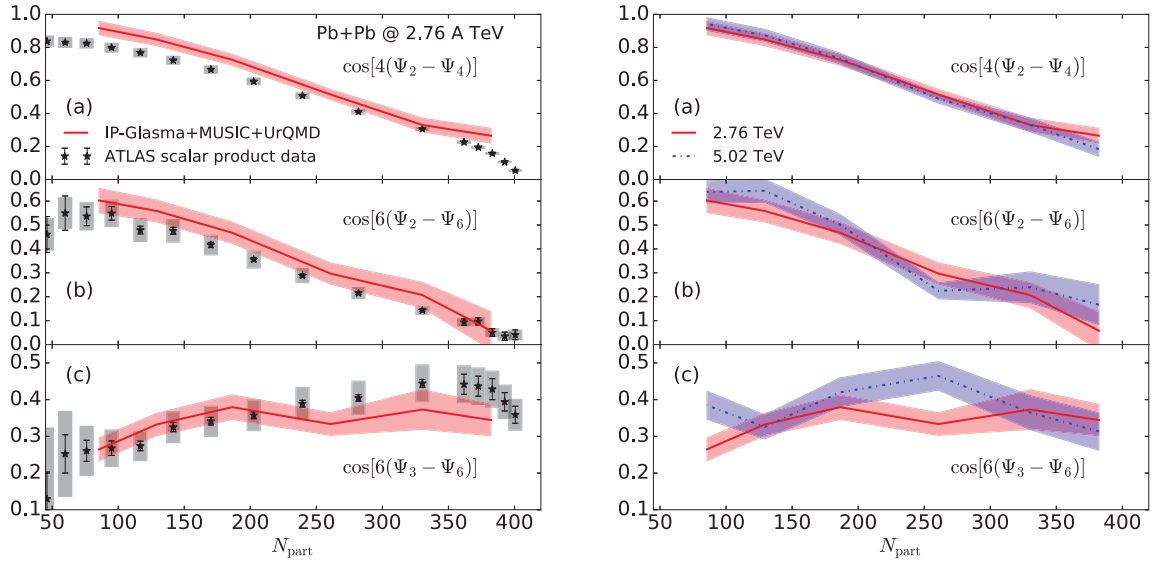

Figure 5.13: Top: Two-plane v_n correlations as a function of centrality for Pb-Pb at 2.76 TeV compared to ATLAS data [66]. Bottom: Two-plane v_n correlations as a function of centrality for Pb-Pb at both LHC energies.

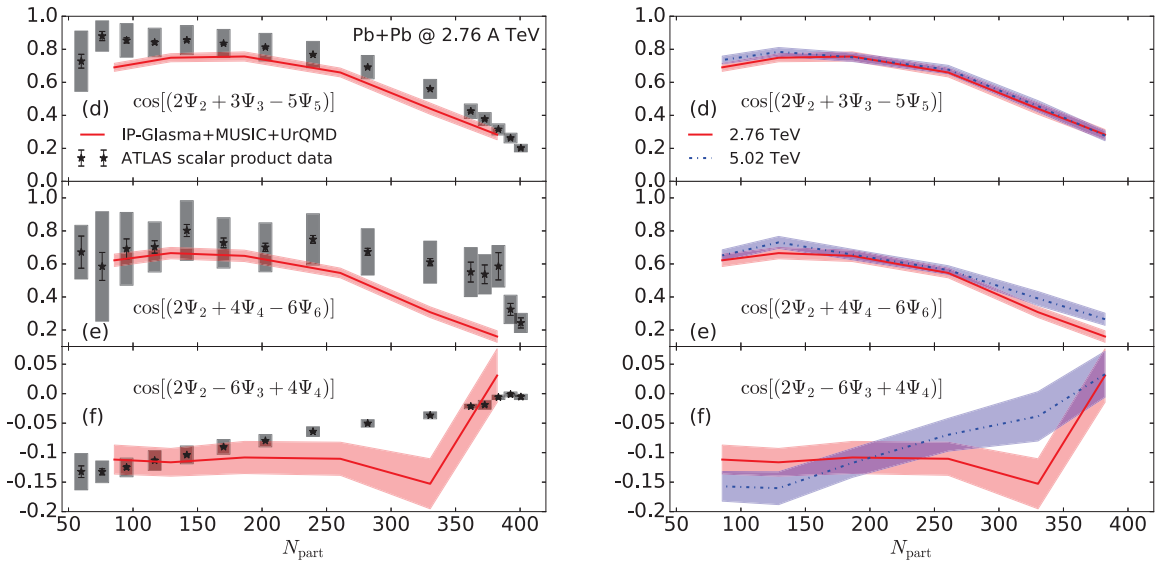

Figure 5.14: Top: Three-plane v_n correlations as a function of centrality for Pb-Pb at 2.76 TeV compared to ATLAS data [66].Bottom: Three-plane v_n correlations as a function of centrality for Pb-Pb at both LHC energies

6

Conclusion

In this thesis, we have discussed the motivation for Heavy Ion Collisions as well as the basic theoretical framework in which we study them, with a strong emphasis on the initial state. In particular, we have provided an in-depth description of the IP-Glasma model and highlighted its distinguishing features. The procedures used to implement IP-Glasma as a numerical simulation have been outlined. Finally, we have presented and analyzed phenomenological results produced in the IP-Glasma+MUSIC+UrQMD framework and shown the incredible success of this model by reproducing a wide range of observables.

Our ability to describe the data at both 2.76 TeV and 5.02 TeV with the same parametrization is a strong indication that the temperatures are similar at the two collision energies. The higher energy provides for a slightly longer lifetime of the QGP fireball and thus allows hydrodynamics to develop more anisotropic flow. Overall, we see only a slight difference on the percent level between the two energies for most observables considered and conclude that there is no fundamentally different physics at the two energies.

While intuitive, these results lend further support for the robust IP-Glasma +MUSIC+UrQMD hybrid model that has been developed at McGill University. Finally, while the results presented are able to reproduce a broad range of observables, they seem to leave a clear signal showing the necessity of high p_T physics, such as jets, for a complete picture of heavy ion physics. Such a signal appears in the differential and integrated v_n observables.

7

Appendices

7.1 Light Cone Coordinates, Rapidity, and Proper Time

.

Light cone coordinates are extremely useful in the context of heavy ion collisions and will be outlined here. This system mixes the temporal coordinate with the beam coordinate to form

$$x^{\pm} = \frac{1}{\sqrt{2}}(x^0 \pm x^3) \tag{7.1}$$

if the direction of the beam is taken to be the third spatial coordinate. Momentum in this system, for example, can be written

$$p^{\pm} = \frac{1}{\sqrt{2}}(p^0 \pm p^3) = \frac{1}{\sqrt{2}}(E \pm p^z) \tag{7.2}$$

Another important feature of light cone coordinates to note is the dot product,

$$x \cdot y = x^+ y^- + x^- y^+ - x_\perp y_\perp \tag{7.3}$$

Other useful definitions that are used throughout this thesis as well as the study of HIC's generally are proper time,

$$\tau = \sqrt{t^2 - z^2} = \sqrt{x^+ x^-} \tag{7.4}$$

and space-time rapidity,

$$\eta = \frac{1}{2}\ln\left(\frac{t+z}{t-z}\right) = \frac{1}{2}\ln\left(\frac{x^+}{x^-}\right) \tag{7.5}$$

Solving these expressions in terms of the Cartesian coordinates t and z,

$$t = \tau \cosh \eta = \frac{1}{2}(x^+ + x^-)$$

$$z = \tau \sinh \eta = \frac{1}{2}(x^+ - x^-)$$

Proper time is the parameter that we use to evolve the system, since it corresponds to the local time of a particle moving in the z-direction,

$$\tau = \sqrt{t^2 - z^2} = t\sqrt{1 - (\frac{z}{t})^2} = t\sqrt{1 - v_z^2} = \frac{t}{\gamma} \tag{7.6}$$

In addition to these coordinates, it is important to make note of the various metrics in the different coordinate systems. Throughout this thesis, we utilize three different coordinate systems: Minkowski (t, x, y, z), Milne (τ, x, y, η), and light cone (x^+, x^-, x, y). One can transform metric tensors between coordinates via,

$$g'_{\alpha\beta} = \frac{\partial x^\mu}{\partial x^\alpha}\frac{\partial x^\nu}{\partial x^\beta} g_{\mu\nu}$$

For the three coordinate systems mentioned we have

$$g_{\mu\nu}(t, x, y, z) = \begin{pmatrix} 1 & 0 & 0 & 0 \\ 0 & -1 & 0 & 0 \\ 0 & 0 & -1 & 0 \\ 0 & 0 & 0 & -1 \end{pmatrix}$$

$$g_{\mu\nu}(\tau, x, y, \eta) = \begin{pmatrix} 1 & 0 & 0 & 0 \\ 0 & -1 & 0 & 0 \\ 0 & 0 & -1 & 0 \\ 0 & 0 & 0 & -\tau^2 \end{pmatrix}$$

$$g_{\mu\nu}(x^+, x^-, x, y) = \begin{pmatrix} 0 & 1 & 0 & 0 \\ 1 & 0 & 0 & 0 \\ 0 & 0 & -1 & 0 \\ 0 & 0 & 0 & -1 \end{pmatrix}$$

7.2 Lie Algebra - SU(3) Algebra

The SU(3) matrices are 3×3 special unitary matrices that obey the following lie algebra,

$$[T^a, T^b] = if^{abc}T^c \tag{7.7}$$

where T^a are group elements of SU(3) and f^{abc} are SU(3) structure constants. In addition, the generators are normalized to obey,

$$\mathrm{Tr}[T^aT^b] = \frac{1}{2}\delta_{ab} \tag{7.8}$$

There are $N_c^2 - 1$ such generators T^a for SU(N), giving 8 in the case of SU(3).

7.3 Dirac Matrices

The gamma matrices γ^μ act on spinors and come in a variety of representations. Their defining feature is the Clifford algebra that they obey, namely the anti-commutation relation,

$$\{\gamma^\mu, \gamma^\nu\} = 2\eta^{\mu\nu} \tag{7.9}$$

where $\mu, \nu = 0, 1, 2, 3$. The simplest representation of the Dirac matrices are 4×4 matrices, meaning there is no such representation in 3×3 or smaller matrices. One prevalently used representation is

$$\gamma^0 = \begin{pmatrix} 0 & 1 \\ 1 & 0 \end{pmatrix} \tag{7.10}$$

$$\gamma^0 = \begin{pmatrix} 0 & \sigma^i \\ -\sigma^i & 0 \end{pmatrix} \tag{7.11}$$

where σ^i are the familiar Pauli matrices.

7.4 Calculating Flow Harmonics - Scalar Product Method

There are various methods and definitions for calculating flow harmonics. The method employed for the plots shown in this thesis is known as the scalar product method and is outlined briefly here. For a more in depth discussion see [67, 68]. First defining the event flow as

$$Q_n = |Q_n| e^{in\psi_n} = \frac{1}{N} \sum_j e^{in\phi_j} \tag{7.12}$$

Then, as is done in the event plane method, one can define particles of interest as, for example, identified particles in a small p_T range and their corresponding flow vector as Q_n. Then v_n is determined by correlating the particles of interest to two different groups of particles, known as sub-events and denoted by A and B, in a wide p_T range with flow vectors Q_{nA}, and Q_{nB}, respectively. The expression is

$$v_n\{SP\} = \frac{\langle Q_n Q_{nA}^* \rangle}{\sqrt{\langle Q_{nA} Q_{nB}^* \rangle}} \tag{7.13}$$

where the name scalar product comes from this definition. This expression assumes that v_n does not fluctuate event to event, an assumption we know not to be true. In the case of of event-by-event fluctuations in v_n, event averages are taken in two steps: first averaging over events with the same v_n and then averaging over v_n bins. Doing so for equation (7.13) and using the following two definitions

$$\langle Q_n Q_{nA}^* \rangle_{|v_n} = \langle Q_n e^{-in\phi_n} \rangle_{|v_n} \langle Q_{nA} e^{-in\phi_n} \rangle_{|v_n}^* = v_n v_{nA} \tag{7.14}$$

$$\langle Q_{nA} Q_{nB}^* \rangle_{|v_n} = v_{nA}^2 \tag{7.15}$$

we can calculate the scalar product result for the fluctuating case,

$$v_n\{SP\} = \frac{\langle v_n v_{nA} \rangle_{v_n}}{\sqrt{\langle v_{nA}^2 \rangle_{v_n}}} = \sqrt{v_n^2} \tag{7.16}$$

The scalar product method does not include any experimental detector specific properties and thus allows for an easy comparison between theory and experiment.

7.5 Flow-Plane Correlations

It is also informative to look at how different v_n coefficients correlate to one another. Such correlations can be defined as [69]

$$C\{c_1 n_1, ..., c_k n_k\}\{SP\} = \frac{\langle Q_{n_1}^{c_1} ... Q_{n_k}^{c_k} \rangle}{\sqrt{\langle Q_{n_1}^{c_1} (Q_{n_1}^{c_1})^* \rangle ... \langle Q_{n_k}^{c_k} (Q_{n_k}^{c_k})^* \rangle}} \tag{7.17}$$

where

$$\sum_{i=1}^{k} c_i n_i = 0 \tag{7.18}$$

In this thesis, we only consider two- and three-plane v_n correlations defined, respectively, as

$$C\{c_1 n_1, c_2 n_2\}\{SP\} = \frac{\langle Q_{n_1}^{c_1} Q_{n_2}^{c_2} \rangle}{\sqrt{\langle Q_{n_1}^{c_1} (Q_{n_1}^{c_1})^* \rangle \langle Q_{n_2}^{c_2} (Q_{n_2}^{c_2})^* \rangle}} \tag{7.19}$$

and

$$C\{c_1 n_1, c_2 n_2, c_3 n_3\}\{SP\} = \frac{\langle Q_{n_1}^{c_1} Q_{n_2}^{c_2} Q_{n_3}^{c_3} \rangle}{\sqrt{\langle Q_{n_1}^{c_1} (Q_{n_1}^{c_1})^* \rangle \langle Q_{n_2}^{c_2} (Q_{n_2}^{c_2})^* \langle Q_{n_3}^{c_3} (Q_{n_3}^{c_3})^* \rangle}} \tag{7.20}$$

So to compute a two-plane angle for v_2 and v_4, for example, a combination that satisfies (7.18) is $n_1 = c_2 = 2$, and $n_2 = c_1 = 4$.

Bibliography

[1] Bjoern Schenke, Prithwish Tribedy and Raju Venugopalan. Event-by-event gluon multiplicity, energy density and eccentricities at RHIC and LHC, 2012; arXiv:1206.6805. DOI: 10.1103/PhysRevC.86.034908.

[2] Bjoern Schenke, Prithwish Tribedy and Raju Venugopalan. Fluctuating Glasma initial conditions and flow in heavy ion collisions, 2012; arXiv:1202.6646. DOI: 10.1103/PhysRevLett.108.252301.

[3] Henri Kowalski and Derek Teaney. An Impact Parameter Dipole Saturation Model, 2003, Phys.Rev. D68 (2003) 114005; arXiv:hep-ph/0304189. DOI: 10.1103/PhysRevD.68.114005.

[4] "Collective Hydrodynamic Flow in the QGP." `http://puma.uio.no/trine/ALICE-Oslo/flow_pattern.html`, June 2015 (accessed August, 2016).

[5] Bjoern Schenke, Sangyong Jeon and Charles Gale. 3+1D hydrodynamic simulation of relativistic heavy-ion collisions, 2010, Phys.Rev.C82:014903,2010; arXiv:1004.1408. DOI: 10.1103/PhysRevC.82.014903.

[6] S. A. Bass, M. Belkacem, M. Bleicher, M. Brandstetter, L. Bravina, C. Ernst, L. Gerland, M. Hofmann, S. Hofmann, J. Konopka, G. Mao, L. Neise, S. Soff, C. Spieles, H. Weber, L. A. Winckelmann, H. Stcker, W. Greiner, Ch. Hartnack, J. Aichelin and N. Amelin. Microscopic Models for Ultrarelativistic Heavy Ion Collisions, 1998, Prog.Part.Nucl.Phys.41:255-369,1998; Prog.Part.Nucl.Phys.41:225-370,1998; arXiv:nucl-th/9803035. DOI: 10.1016/S0146-6410(98)00058-1.

[7] F. Gelis. Color Glass Condensate and Glasma, 2012; arXiv:1211.3327. DOI: 10.1142/S0217751X13300019.

[8] Edmond Iancu, Andrei Leonidov and Larry McLerran. Nonlinear Gluon Evolution in the Color Glass Condensate: I, 2000, Nucl.Phys. A692 (2001) 583-645; arXiv:hep-ph/0011241. DOI: 10.1016/S0375-9474(01)00642-X.

[9] Larry McLerran and Raju Venugopalan. Computing Quark and Gluon Distribution Functions for Very Large Nuclei, 1993, Phys.Rev.D49:2233-2241,1994; arXiv:hep-ph/9309289. DOI: 10.1103/PhysRevD.49.2233.

[10] Ringaile Placakyte, for the H1 Collaboration and for the ZEUS Collaboration. Parton Distribution Functions, 2011; arXiv:1111.5452.

[11] The CMS Collaboration. Transverse-momentum and pseudorapidity distributions of charged hadrons in pp collisions at $s = 7$TeV, 2010, Phys.Rev.Lett.105:022002,2010; arXiv:1005.3299. DOI: 10.1103/PhysRevLett.105.022002.

[12] Edmond Iancu and Raju Venugopalan. The Color Glass Condensate and High Energy Scattering in QCD, 2003; arXiv:hep-ph/0303204.

[13] F. Gelis. Initial state and thermalization in the Color Glass Condensate framework, 2015; arXiv:1508.07974. DOI: 10.1142/S0218301315300088.

[14] Edmond Iancu, Andrei Leonidov and Larry McLerran. The Colour Glass Condensate: An Introduction, 2002; arXiv:hep-ph/0202270.

[15] Larry McLerran and Raju Venugopalan. Computing Quark and Gluon Distribution Functions for Very Large Nuclei, 1993, Phys.Rev.D49:2233-2241,1994; arXiv:hep-ph/9309289. DOI: 10.1103/PhysRevD.49.2233.

[16] Alex Krasnitz, Yasushi Nara and Raju Venugopalan. Gluon production in the Color Glass Condensate model of collisions of ultrarelativistic finite nuclei, 2002, Nucl.Phys.A717:268-290,2003; arXiv:hep-ph/0209269. DOI: 10.1016/S0375-9474(03)00636-5.

[17] Jamal Jalilian-Marian, Alex Kovner, Larry McLerran and Heribert Weigert. The Intrinsic Glue Distribution at Very Small x, 1996, Phys.Rev. D55 (1997) 5414-5428; arXiv:hep-ph/9606337. DOI: 10.1103/PhysRevD.55.5414.

[18] Alex Kovner, Larry McLerran and Heribert Weigert. Gluon Production at High Transverse Momentum in the McLerran-Venugopalan Model of Nuclear Structure Functions, 1995, Phys.Rev. D52 (1995) 3809-3814; arXiv:hep-ph/9505320. DOI: 10.1103/PhysRevD.52.3809.

[19] Alex Kovner, Larry McLerran and Heribert Weigert. Gluon Production from Non-Abelian Weizscker-Williams Fields in Nucleus-Nucleus Collisions, 1995, Phys.Rev. D52 (1995) 6231-6237; arXiv:hep-ph/9502289. DOI: 10.1103/PhysRevD.52.6231.

[20] Larry McLerran. The CGC and the Glasma: Two Lectures at the Yukawa Insitute, 2010, Prog.Theor.Phys.Suppl.187:17-30,2011; arXiv:1011.3204. DOI: 10.1143/PTPS.187.17.

[21] Bjoern Schenke and Soeren Schlichting. 3-D Glasma Initial State for Relativistic Heavy Ion Collisions, 2016; arXiv:1605.07158.

[22] T. Lappi. Wilson Line Correlator in the MV Model: Relating the Glasma to Deep Inelastic Scattering, 2007, Eur.Phys.J.C55:285-292,2008; arXiv:0711.3039. DOI: 10.1140/epjc/s10052-008-0588-4.

[23] T. Lappi. Production of Gluons in the Classical Field mMdel for Heavy Ion Collisions, 2003, Phys.Rev. C67 (2003) 054903; arXiv:hep-ph/0303076. DOI: 10.1103/PhysRevC.67.054903.

[24] Alex Krasnitz and Raju Venugopalan. Non-Perturbative Computation of Gluon Mini-Jet Production in Nuclear Collisions at Very High Energies, 1998, Nucl.Phys. B557 (1999) 237; arXiv:hep-ph/9809433. DOI: 10.1016/S0550-3213(99)00366-1.

[25] T. Lappi. Energy Density of the Glasma, 2006, Phys.Lett.B643:11-16,2006; arXiv:hep-ph/0606207. DOI: 10.1016/j.physletb.2006.10.017.

[26] Edmond Iancu. The Colour Glass Condensate, 2002, Nucl.Phys.A715:219-232,2003; arXiv:hep-ph/0210236. DOI: 10.1016/S0375-9474(02)01430-6.

[27] Amir H. Rezaeian, Marat Siddikov, Merijn Van de Klundert and Raju Venugopalan. Analysis of Combined HERA Data in the Impact-Parameter Dependent Saturation model, 2012, Phys.Rev.D87:034002,2013; arXiv:1212.2974. DOI: 10.1103/PhysRevD.87.034002.

[28] G. Altarelli and G. Parisi, "Asymptotic Freedom in Parton Language," *Nucl. Phys.*, vol. B126, pp. 298–318, 1977.

[29] Y. L. Dokshitzer, "Calculation of the Structure Functions for Deep Inelastic Scattering and e+ e- Annihilation by Perturbation Theory in Quantum Chromodynamics.," *Sov. Phys. JETP*, vol. 46, pp. 641–653, 1977. [Zh. Eksp. Teor. Fiz.73,1216(1977)].

[30] V. N. Gribov and L. N. Lipatov, "Deep inelastic e p Scattering in Perturbation Theory," *Sov. J. Nucl. Phys.*, vol. 15, pp. 438–450, 1972. [Yad. Fiz.15,781(1972)].

[31] F. Gelis, "Software (DGLAP Equation)." `http://ipht.cea.fr/Pisp/francois.gelis/Soft/DGLAP/index.php`. Accessed July 5, 2016.

[32] Bjoern Schenke, Prithwish Tribedy and Raju Venugopalan. Multiplicity Distributions in p+p, p+A and A+A Collisions from Yang-Mills Dynamics, 2013, Phys. Rev. C 89, 024901 (2014); arXiv:1311.3636. DOI: 10.1103/PhysRevC.89.024901.

[33] M. Alvioli, H. -J. Drescher and M. Strikman. A Monte Carlo Generator of Nucleon Configurations in Complex Nuclei Including Nucleon-Nucleon Correlations, 2009, Phys. Lett. B 680 (2009) 225-230; arXiv:0905.2670. DOI: 10.1016/j.physletb.2009.08.067.

[34] G. Chen, R. J. Fries, J. I. Kapusta and Y. Li. Early Time Dynamics of Gluon Fields in High Energy Nuclear Collisions, 2015, Phys. Rev. C 92, 064912 (2015); arXiv:1507.03524. DOI: 10.1103/PhysRevC.92.064912.

[35] Daniel N. Blaschke, Francois Gieres, Meril Reboud and Manfred Schweda. The Energy-Momentum Tensor(s) in Classical Gauge Theories, 2016; arXiv:1605.01121.

[36] Francois Gelis and Bjoern Schenke. Initial State Quantum Fluctuations in the Little Bang, 2016; arXiv:1604.00335.

[37] Thomas Epelbaum and Franois Gelis. Isotropization of the Quark Gluon Plasma, 2014; arXiv:1401.1666. DOI: 10.1016/j.nuclphysa.2014.02.014.

[38] T. Epelbaum, *Approach to Equilibrium in High Energy Heavy Ion Collisions*. PhD thesis, 2014.

[39] Sangyong Jeon and Ulrich Heinz. Introduction to Hydrodynamics, 2015; arXiv:1503.03931.

[40] G. S. Denicol, S. Jeon and C. Gale. Transport Coefficients of Bulk Viscous Pressure in the 14-moment Approximation, 2014; arXiv:1403.0962. DOI: 10.1103/PhysRevC.90.024912.

[41] Aleksi Kurkela and Yan Zhu. Isotropization and Hydrodynamization in Weakly Coupled Heavy-Ion Collisions, 2015, Phys. Rev. Lett. 115, 182301 (2015); arXiv:1506.06647. DOI: 10.1103/PhysRevLett.115.182301.

[42] Michal P. Heller, Romuald A. Janik and Przemyslaw Witaszczyk. The Characteristics of Thermalization of Boost-Invariant Plasma from Holography, 2011, Phys. Rev. Lett. 108, 201602 (2012); arXiv:1103.3452. DOI: 10.1103/PhysRevLett.108.201602.

[43] S. Ryu, J. -F. Paquet, C. Shen, G. S. Denicol, B. Schenke, S. Jeon and C. Gale. The Importance of the Bulk Viscosity of QCD in Ultrarelativistic Heavy-Ion

Collisions, 2015, Phys. Rev. Lett. 115, 132301 (2015); arXiv:1502.01675. DOI: 10.1103/PhysRevLett.115.132301.

[44] G. S. Denicol, T. Kodama, T. Koide and Ph. Mota. Effect of Bulk Viscosity on Elliptic Flow Near QCD Phase Transition, 2009, Phys.Rev.C80:064901,2009; arXiv:0903.3595. DOI: 10.1103/PhysRevC.80.064901.

[45] F. Karsch, D. Kharzeev and K. Tuchin. Universal Properties of Bulk Viscosity Near the QCD Phase Transition, 2007, Phys.Lett.B663:217-221,2008; arXiv:0711.0914. DOI: 10.1016/j.physletb.2008.01.080.

[46] Jacquelyn Noronha-Hostler, Jorge Noronha and Carsten Greiner. Transport Coefficients of Hadronic Matter Near T_c, 2008, Phys.Rev.Lett.103:172302,2009; arXiv:0811.1571. DOI: 10.1103/PhysRevLett.103.172302.

[47] F. Cooper and G. Frye, "Comment on the Single Particle Distribution in the Hydrodynamic and Statistical Thermodynamic Models of Multiparticle Production," *Phys. Rev.*, vol. D10, p. 186, 1974.

[48] S. Ryu, *Integrated Description of Heavy Ion Collisions at RHIC and the LHC*. PhD thesis, McGill University, 2016.

[49] Hannah Petersen, Jan Steinheimer, Gerhard Burau, Marcus Bleicher and Horst Stcker. Fully Integrated Transport Approach to Heavy Ion Reactions with an Intermediate Hydrodynamic Stage, 2008, Phys.Rev.C78:044901,2008; arXiv:0806.1695. DOI: 10.1103/PhysRevC.78.044901.

[50] Kenji Fukushima and Francois Gelis. The Evolving Glasma, 2011; arXiv:1106.1396. DOI: 10.1016/j.nuclphysa.2011.11.003.

[51] M. Cautun, "Photon Production in the Color Glass Condensate Formalism," Master's thesis, McGill University, Montreal, QC Canada, 2009.

[52] R. P. Brent, *Algorithms for Minimization Without Derivatives*. Dover Publications, 2013. [ISBN:9781306352611]

[53] H. Walker, "Brent's Method." http://users.wpi.edu/~walker/MA3257/HANDOUTS/brents_algm.pdf, 2006 (accessed August, 2016).

[54] M. E. Peskin and D. V. Schroeder, *An Introduction To Quantum Field Theory (Frontiers in Physics)*. Westview Press, 1995. [ISBN:9780201503975]

[55] G. Münster and M. Walzl. Lattice Gauge Theory - A Short Primer, 2000; arXiv:hep-lat/0012005.

[56] G. Moore, "Informal Lectures on Lattice Gauge Theory."http://theorie.ikp.physik.tu-darmstadt.de/qcd/latt_lectures.pdf 2003 (accessed August, 2016).

[57] ALICE Collaboration (K. Aamodt *et al.*) Centrality Dependence of the Charged-Particle Multiplicity Density at Mid-Rapidity in Pb-Pb Collisions at $\sqrt{s_{NN}}$ = 2.76 TeV, 2010, Phys.Rev.Lett.106:032301,2011; arXiv:1012.1657. DOI: 10.1103/PhysRevLett.106.032301.

[58] ALICE Collaboration. Centrality Dependence of the Charged-Particle Multiplicity Density at Mid-Rapidity in Pb-Pb collisions at $\sqrt{s_{\rm NN}}$ = 5.02 TeV, 2015, Phys. Rev. Lett. 116, 222302 (2016); arXiv:1512.06104. DOI: 10.1103/PhysRevLett.116.222302.

[59] ALICE Collaboration. Anisotropic Flow of Charged Particles in Pb-Pb Collisions at $\sqrt{s_{\rm NN}}$ = 5.02 TeV, 2016, Phys. Rev. Lett. 116, 132302 (2016); arXiv:1602.01119. DOI: 10.1103/PhysRevLett.116.132302.

[60] ALICE Collaboration. Higher Harmonic Anisotropic Flow Measurements of Charged Particles in Pb-Pb collisions at 2.76 TeV, 2011, Phys.Rev.Lett. 107:032301,2011; arXiv:1105.3865. DOI: 10.1103/PhysRevLett.107.032301.

[61] ALICE Collaboration. Anisotropic Flow of Charged Particles in Pb-Pb Collisions at $\sqrt{s_{\rm NN}}$ = 5.02 TeV, 2016, Phys. Rev. Lett. 116, 132302 (2016); arXiv:1602.01119. DOI: 10.1103/PhysRevLett.116.132302.

[62] ALICE Collaboration. Elliptic Flow of Identified Hadrons in Pb-Pb Collisions at $\sqrt{s_{\rm NN}}$ = 2.76 TeV, 2014, JHEP 06 (2015) 190; arXiv:1405.4632. DOI: 10.1007/JHEP06(2015)190.

[63] Charles Gale, Sangyong Jeon, Bjoern Schenke, Prithwish Tribedy and Raju Venugopalan. Initial State Fluctuations and Higher Harmonic Flow in Heavy-Ion Collisions, 2012; arXiv:1210.5144. DOI: 10.1016/j.nuclphysa.2013.02.037.

[64] Jiangyong Jia and for the ATLAS Collaboration. Measurement of the Distributions of Event-by-Event Flow Harmonics in Pb-Pb Collisions at $\sqrt{s_{NN}}$=2.76 TeV with the ATLAS detector, 2012, Nucl.Phys.A904-905,421 (2013); arXiv:1209.4232. DOI: 10.1016/j.nuclphysa.2013.02.039.

[65] ALICE Collaboration. Centrality Dependence of π, k, p Production in Pb-Pb Collisions at $\sqrt{s_{\rm NN}}$ = 2.76 TeV, 2013, Phys. Rev. C 88, 044910 (2013); arXiv:1303.0737. DOI: 10.1103/PhysRevC.88.044910.

[66] ATLAS Collaboration. Measurement of Event-Plane Correlations in $\sqrt{s_{NN}}$=2.76 TeV Lead-Lead Collisions with the ATLAS Detector, 2014, Phys. Rev. C 90, 024905 (2014); arXiv:1403.0489. DOI: 10.1103/PhysRevC.90.024905.

[67] Matthew Luzum and Jean-Yves Ollitrault. Eliminating Experimental Bias in Anisotropic-Flow Measurements of High-Energy Nuclear Collisions, 2012, Phys.Rev. C87 (2013) 044907; arXiv:1209.2323. DOI: 10.1103/PhysRevC.87.044907.

[68] STAR collaboration. Elliptic Flow from Two- and Four-Particle Correlations in Au + Au Collisions at $\sqrt{s_{NN}}$ = 130 GeV, 2002, Phys.Rev.C66:034904,2002; arXiv:nucl-ex/0206001. DOI: 10.1103/PhysRevC.66.034904.

[69] C. Shen, *The Standard Model for Relativistic Heavy-Ion Collisions and Electromagnetic Tomography*. PhD thesis, Ohio State University, 2014.